Physical Mechanisms of DNA repair:
A single molecule perspective

Andrea Candelli
Physics of Living Systems
Department of Physics and Astronomy
Faculty of Exact Sciences
VU University Amsterdam

This thesis was reviewed by the following committee:

Prof. dr. Gijs J.L. Wuite
VU University Amsterdam, The Netherlands

Prof. dr. Erwin J.G. Peterman
VU University Amsterdam, The Netherlands

Prof. dr. Taekjip Ha
University of Illinois, Urbana Champaign, USA

Prof. dr. Antoine M. van Oijen
Rijksuniversiteit Groningen, The Netherlands

Dr. Luca Pellegrini
Cambridge University, United Kingdom

Dr. Greg J. Stephens
VU University Amsterdam, The Netherlands

Prof. dr. Claire Wyman
Erasmus University Medical Center, Rotterdam, The Netherlands

Cover designed by Rodolfo Riccomboni

A digital version is available at: www.ubvu.vu.nl/dissertations

This work is funded by NWO (Nederlandse Organisatie voor WetenSchappelijk Onderzoek) via the TopTalent programme.

The reaserch was performed in the Department of Physics and Astronomy at the VU University Amsterdam, Amsterdam, The Netherlands

VRIJE UNIVERSITEIT

Physical Mechanisms of DNA repair:
A single molecule perspective

ACADEMISCH PROEFSCHRIFT

ter verkrijging van de graad Doctor aan
de Vrije Universiteit Amsterdam,
op gezag van de rector magnificus
prof.dr. F.A. van der Duyn Schouten,
in het openbaar te verdedigen
ten overstaan van de promotiecommissie
van de Faculteit der Exacte Wetenschappen
op donderdag 30 mei 2013 om 11.45 uur
in de aula van de universiteit,
De Boelelaan 1105

door

Andrea Candelli

geboren te Trieste, Italië

promotoren:

prof.dr.ir. G.J.L. Wuite
prof.dr.ir. E.J.G. Peterman

Keep Ithaca always in your mind.
Arriving there is what you're destined for.
But don't hurry the journey at all.
Better for it to last many years,
and to anchor at the island when you are old,
rich with all you have gained on the way,
don't expect Ithaca to offer you wealth.
Ithaca gave you the journey.
Without her, you wouldn't ever have left.

Tienila sempre in mente, Itaca.
La tua meta, approdarvi.
Ma non far fretta al tuo viaggio.
Meglio che duri molti anni,
e che ormai vecchio alla tua isola attracchi,
ricco di quel che guadagnasti per via,
senza aspettarti da Itaca ricchezze.
Itaca ti ha donato il bel viaggio
Non saresti partito senza di lei.

Konstantinos Kavafis, *Ithaca* (1911)

CONTENTS

LIST OF FIGURES

1 DNA DAMAGE AND REPAIR

DNA DAMAGE AND REPAIR

The scope of this introductory chapter is to provide the reader a brief introduction on the topics discussed in this thesis: the molecular mechanisms of DNA damage and repair. First I will discuss the physical structure and the biological role of DNA. Next, I will present an overview of the cellular strategies to repair the various types of DNA lesions and the medical relevance of these reparatory pathways. Finally, I will explain how single-molecule technologies can contribute to the understanding of these important biological processes. A brief overview of the content of this thesis is also presented.

1.1 SINGLE MOLECULES AND DNA

The information essential for life is stored and encoded in long polymers called deoxyribose nucleic acids, or DNA. The chemical structure of its monomers, nucleotides, are composed of three important components: i) a purine (Adenine – A or Guanine – G) or pyrimidine base (Cytosine – C or Thymine – T), ii) a sugar deoxyribose group and iii) a phosphate group. Nucleotides are connected in long chains with a backbone consisting of alternating phosphates and deoxyriboses. The bases are linked covalently to the sugar groups. In the cell, two DNA polymers chains are connected, forming a right-handed double helix. In this double helix, the bases point inwards, forming specific hydrogen-bonded pairs: C pairs to G forming 3 hydrogen-bonds, while the A:T pair forms 2 hydrogen bonds (see Figure 1).

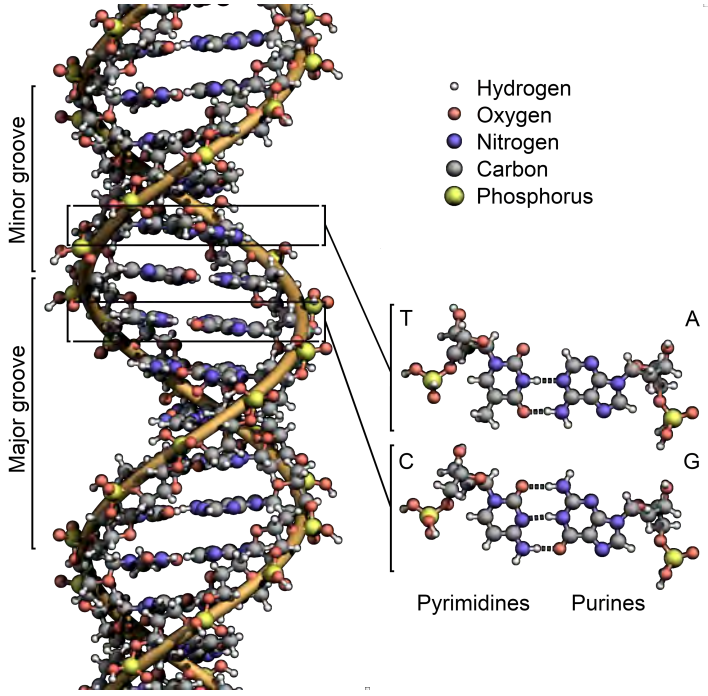

Figure 1.: Structure of the DNA double helix The atoms composing the deoxyribonucleic acid are color-coded and the double-helical arrangement of the two strands is visible (orange strand). The bases point inwards and are paired between opposite strands with specific hydrogen bonds between A and T and C and G (see inset). Image credit: Wikipedia.

In the cell, DNA is covered with proteins, forming structures called chromosomes. Human cells contain 23 pairs of chromosomes, containing in total approximately 3 billions of nucleotides. The total length of DNA in in a cell is several meters (0.34 nm per base pair). To fit in the cell's nucleus with a size of several micrometers, DNA has to be compacted. The cell accomplishes this function using specialized proteins that are able to wrap the DNA around them. Compaction and genome organization highlight key questions concerning DNA mechanics that are essential for cellular life. The advent of single-molecule technologies has made it possible to address such questions with a quantitative and physical point of view.

1.2 DNA BREAKS AND REPAIR MECHANISMS

Two important aspects of the DNA metabolism in cellular life should be noted. First of all, during cell proliferation, the genetic information should be passed to the daughter cells rapidly and accurately, with little or no errors. In the long term, genetic modifications are essential, since they drive the evolution of organisms by impacting their chances of survival. On the other hand, within the lifetime of an individual organism, genetic stability is required. While most cellular components are continuously being created and degraded, the cell's genetic information must be preserved intact. Two requirements, therefore, must be met: (i) an accurate DNA replication mechanism must be in place, and (ii) efficient strategies for the repair of DNA lesions have to be in place. DNA molecules are physically and chemically unstable and many different types of damage can occur, due to the endogenous and exogenous factors. Undesired DNA modifications can occur as casual errors during normal DNA metabolic process such as replication, recombination and repair. In addition, numerous chemicals and environmental agents (exogenous mutagens and endogenously produced reactive oxygen species) can create dangerous genomic modifications. Understanding the mechanisms of DNA damage and repair, together with the consequences of these genetic damages is crucial. In fact, DNA damages can be deleterious for living organisms, with consequences including cell death, inheritable mutations and, in certain circumstances, life-threating diseases such as cancer [73]. To highlight this fact, many of the genes that participate in the DNA repair mechanisms are now included in the class of

tumor suppressing genes. There are several repair mechanisms available for the cell to react to the different types of DNA damages. In the following sections we will review their fundamental function and determining steps (see Figure 2).

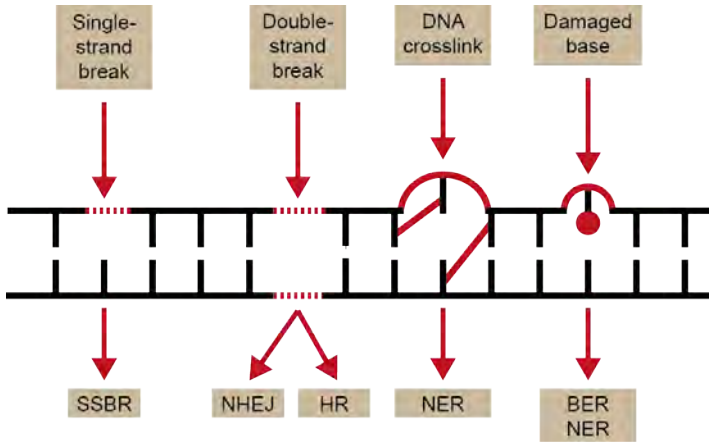

Figure 2.: DNA damage and repair mechanisms. DNA chemical and structural integrity is continuously threatened by exogenous and endogenous agents. Specialized DNA repair mechanisms respond to different types of lesions. SSBR, single-strand break repair. NHEJ, non-homologous end joining. HR, homologous recombination. NER, nucleotide excision repair. BER, base excision repair.

1.2.1 Nucleotide excision repair

Nucleotide excision repair (NER) responds to specific chemical modifications of DNA bases [86]. Modifications in the DNA base chemistry such as cyclobutane pyrimidine dimers (CPD) and [6-4] photoproducts alter the regular base pairing, creating modified DNA structures, commonly referred to as "DNA adducts". These mutations originate from exogenous agents such as sunlight (UV DNA damage) or chemical carcinogens (the fungal toxin aflatoxin B1 for example) and involve the covalent cross -links between adjacent pyrimidine bases (CC, TT or CT) or the covalent attachment of chemical groups to the DNA bases. NER can follow two different pathway, depending on whether the DNA damage has occurred on a transcribed region (Transcription coupled repair – TCR) or not (Global genomic repair – GCR). The main catalytic steps in NER are recognition

of the DNA damage, removal of a short single-stranded DNA (ssDNA) gap around the damaged sequence, DNA synthesis using the undamaged ssDNA as a template, and a final ligation step. The importance of NER is evidenced by the fact that specific mutations in NER-related genes result in severe syndromes such Xeroderma pigmentosum (XP) and Cockayne's syndrome, characterized by increased photosensitivity and high probability of developing skin cancer.

1.2.2 Base excision repair

Similarly to NER, the base-excision repair (BER) pathway is composed of a set of enzymes that recognize and modify chemically altered bases in the genome. BER, however, specifically repairs another class of DNA lesions, depurination, depyrimidation, base deamination or base alkylation [43]. These modifications, in contrast to the ones repaired by the NER pathway, do not affect the physical structure of the DNA double helix. BER is initiated by specific DNA glycosylases that recognize the chemically abnormal base and cleave the covalent bond to the deoxyribose, leaving behind a abasic site. After removal of the altered base, the exposed sugar is recognized and excised by specific endonucleases (APE – apurinic/apyrimidine endonucleases). A single-strand gap of 1 or 2 bases is therefore created and is filled in by a DNA polymerase β. The final step of this repair process consists in a ligation step and is accomplished either by a XRCC1-Ligase 3α complex or by the DNA Ligase 1.

1.2.3 Single-stranded break repair

Single-stranded breaks (SSBs) consist of a physical interruption of one of the strand of the DNA double helix. The predominant cause of SSBs is oxidative attack by endogenously generated reactive oxygen species (ROS). SSBs are one of the most predominant DNA lesions in the cell (SSBs occurs up to three orders of magnitude more frequently than DSBs) and therefore need to be repaired quickly and efficiently. Unrepaired SSBs can cause stalled DNA replication forks, eventually leading to the generation of double-stranded breaks, a very harmful form of DNA lesion. A crucial component of the SSB repair pathway [24] is the SSB sensor, the poly-(ADP-ribose) polymerase 1 (PARP1) which are directly involved in the detection

of the SSB and in the early stage of the SSB repair pathway. To restore the sequence integrity, the DNA ends must first be processed to obtain the canonical hydroxyl group at the 3' end (3'-OH) and phosphate group at the 5'-end. This is a pre-requisite to complete the later step of the repair: gap filling and the DNA ligations step. A number of hereditary genetic diseases is linked to malfunctions in SSB repair, such as Ataxia-oculomotor Apraxia 1 and Spinocerebellar ataxia with axonal neuropathy.

1.2.4 Double-streanded break repair mechanisms

Double-stranded DNA breaks (DSBs) represent one of the most harmful genomic lesions and can cause genome rearrangements and cell death, if left unrepaired. DSBs can arise either due to exogenous sources, such as ionizing radiation (IR) or due to endogenous events, such as meiosis and replication forks encountering SSBs. Upon occurrence of DSBs, both eukaryotic and prokaryotic organisms have two main strategies to repair the DNA and re-establish the genome integrity, homologous recombination (HR) and non-homologous end joining (NHEJ). The choice between the two pathways depends various factors [79, 31], including the availability of a second copy of the genetic information, the type of lesion suffered by the DNA and the cell type. During late S and G2 cell phases, for example, a homologous sequence donor is present and HR is the predominant mechanism of repair. During the other cell phases, DSBs (non-replication associated breaks) are mostly repaired by the NHEJ pathway.

Homologous recombination

HR is a complex, accurate, multi-step process that repairs double-stranded DNA breaks [71, 142] (see Figure 3). To restore genetic integrity, HR makes use of the sister chromosome as a template to prevent loss of precious genetic information. The fundamental role of HR in genome maintenance is highlighted by the fact that a variety of hereditary cancer syndromes, including breast and ovarian cancer, are attributable to malfunctions in HR-related genes [73].

The current model of HR comprises three major phases [71, 142]: presynapsis (the formation of the recombinase-DNA filament), synapsis (the formation of a strand exchange complex) and post-synapsis (the restoration of the genome integrity). HR is initiated after the occurrence of a

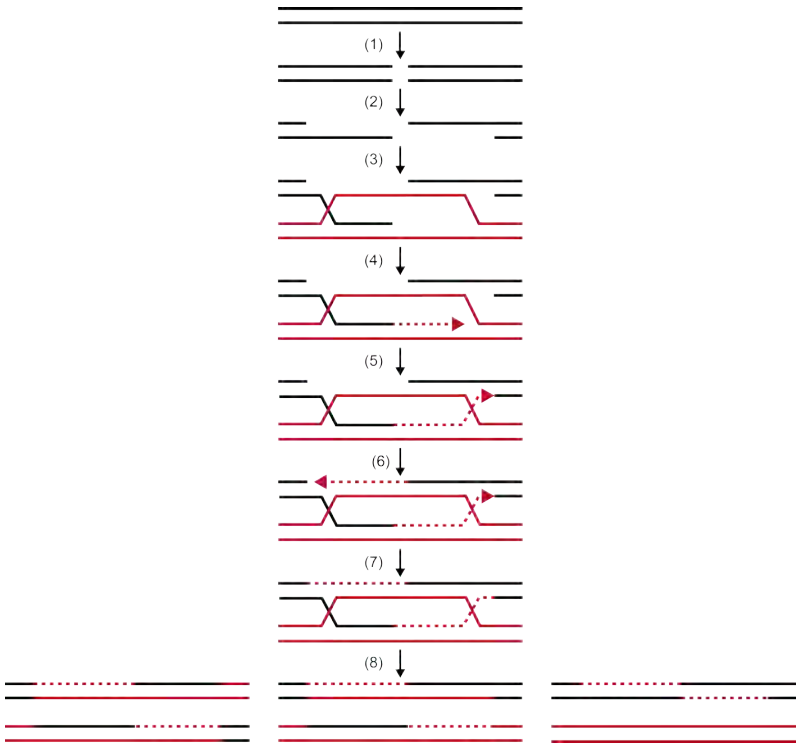

Figure 3.: Mechanisms of double-stranded break repair by homologous recombination. The integrity of the genome can be affected by exogenous and endogenous factors. After the occurrence of a DSB (1), the DNA-ends are resected and a ssDNA overhang is created (2). The RAD51 nucleoprotein filament binds to the ssDNA and search and pair with the homologous sequence, displacing one of the strand and creating a D-loop (3). A DNA polymerase uses the invaded template strand and recovers the lost genetic information (4). The second end of the broken chromosome is captured by specialized enzymes (RAD52) (5) and a second DNA synthesis step takes place (6). A double Holliday junction structure is than formed (7). The final structure can be resolved in multiple alternative ways, resulting in crossover or non-crossover products (8).

double-stranded DNA break and the subsequent detection by the MRN complex (MRE11, RAD50 and NSB1 protein). The MRN complex is also involved in physically tethering the two broken DNA ends together, preventing the drifting away of the broken chromosomes fragments. The following step consists in the end-resection and the creation of a long single-stranded DNA (ssDNA) overhang (approximately 1000 nucleotides). The resection-step is initiated by a specialized enzyme (CtIP), activated by the

cyclin-dependent kinase (CDK) and finalized by a nuclease-helicase helicase complex (BLM-DNA2 for example), which is able to accomplish directional, processive DNA end-resection. Replication protein A (RPA) binds to the newly formed single-stranded DNA, protecting it from degradation. The central component of HR, RAD51 forms a helical nucleoprotein filament around the ssDNA assisted by one or more recombinase mediators. RAD51 performs the important task of pairing with the homologous DNA sequence of the sister chromosome and mediate the strand-exchange reaction. Upon completion of the strand-exchange reaction and the successful creation of a joint molecule, RAD51 disassembles in order to allow the DNA polymerase to access the site of damage and use the sister chromosome as a template to recover the genetic information. In the final phase of HR, a double Holliday junction structure is created which is resolved by different specialized pathways.

There is a considerable interest in the understanding of HR pathway, since a number of hereditary cancer syndromes display defects in genes involved in the HR pathway. In particular, the assembly of the RAD51 recombinase filament on ssDNA is of particular interest, since it is at a center of a complex regulatory network. Among the proteins involved in the regulation of the assembly of RAD51 filament the protein BRCA2 is especially important, since possesses several distinct RAD51-binding subunits that physically interact with RAD51 which are involved in facilitating the formation of the RAD51 nucleoprotein filament. Mutations in BRCA2 lead to chromosomal rearrangements, hypersensitivity to DSBs and predispose individuals to high risks of breast and ovarian cancer.

Non-homologous end joining

Most of the double-stranded DNA breaks occurring in the cell are repaired by NHEJ [95]. NHEJ operates very differently from compared to HR. In NHEJ, DNA-end resection is blocked and the presence of the second chromosome copy is not required to perform the repair process. NHEJ operates by direct ligation of the DSB, which makes it an error-prone repair mechanism. Although our understanding of NHEJ is not yet complete, it is considered to consist of three major steps. First, a complex of Ku70/80 and DNA-PKcs is involved in the detection of the DSB and in tethering the two broken DNA ends together. After this step, specialized enzymes

process the DNA-ends and a complex of XRCC4 and Ligase IV mediate the ligation of the broken ends stimulated by the protein XLF.

1.3 DNA REPAIR AND CANCER

Understanding the different causes of DNA damages and the various repair mechanisms is not only important for from a biological point of view but it has important medical implications. It is well known that carcinogenic agents are very potent mutagens, indicating that modifications in the genetic code are involved in the proliferation of cancer cells. Specifically, modifications or inactivation of genes involved in genome maintenance can drastically increase the mutation rate, eventually making the cell acquire the typical traits of cancer [73, 65]. Genome instability has been detected in virtually all forms of cancer and constitutes one of the hallmarks of cancers[65]. At the same time, understanding the mechanisms of DNA repair not only contribute to the causes of cancer formation but can furnish insights in how to medically treat it.

The basic idea behind modern cancer therapy is to expose the patient's body to agents (such as chemicals and high energy radiation) that kill cancer cells more efficiently than healthy tissues. In order to specifically target cancer cells, these external agents exploit specific cellular features of cancer. In some cases, cancer therapies target the cell cycle (cell division and growth), since many cancer cells show an enhanced proliferation rate compared to their healthy counterparts. In order to induce cell's death, the fundamental therapeutic approach consists in inducing DNA damages. If left unrepaired, lesions to DNA causes cell-cycle arrest and subsequently cell death. Cells death can occur either directly or following DNA replication across a damaged section of the genome. Because cancer tissues are composed of fast replicating cells, DNA-damaging agents are therefore selective for cancer-replicating cells. The side effect of the potent mutagenicity of anti-cancer chemotherapeutics is the possibility of the appearance of a second therapy-induced tumor.

In the human body, as previously explained, a several DNA damage response systems are in place that can react to these DNA damaging agents and repair the damages before it provokes the cell's death. DNA repair, therefore, greatly reduces the effect of DNA-damaging drugs. The efficacy

of DNA damage therapeutics and the DNA repair pathways are therefore strongly intertwined [143, 181]. Interestingly, in many cancers the DNA damage response system is strongly altered, some pathways are inactivated while others may be upregulated. Targeting specific defects in the DNA repair mechanisms of cancer cells represent a potential novel route for treating cancer more efficiently [131, 41, 34].

1.4 SINGLE MOLECULE BIOPHYSICS

The development of single-molecule technologies allowed the interrogation of individual biological systems and found widespread application in the context of DNA-proteins interactions. Optical tweezers enable researchers to manipulate single DNA molecules and measure their mechanical properties with exquisite sensitivity. Single-fluorescence microscopy is a complementary technique, capable of following individual proteins translocating on nucleic acids and their conformational changes. An important development in the field of single-molecule biophysics consists in correlating mechanical with fluorescence information. This allows studying biological processes at the single molecule level from multiple points of view, providing the opportunity to look at molecular interactions from a more complete perspective.

The primary goal of my thesis is to study repair mechanisms using these single molecule tools because they provide essential mechanistic information about these processes which is currently still lacking. In particular, I use throughout my research instrumentation that combines single-molecule DNA manipulation and single-protein visualization. The instrument I designed and constructed integrates optical tweezers, single-molecule fluorescence microscopy and microfluidics into a unique platform. By using this instrument, I was able, at the same time to manipulate and measure mechanical and structural properties of DNA-protein complexes, localize individual proteins on DNA with nanometer accuracy and trigger the biochemical reaction in a controllable way. This methodology allowed to isolate and study with molecular resolution DNA repair processes in real-time, providing the opportunity to look at its physical mechanisms from a quantitative point of view.

1.5 OUTLINE OF THE THESIS

In this thesis, optical tweezers, single-molecule fluorescence microscopy and microfluidics are combined to obtain new insights in the physical mechanisms of DNA repair.

Chapter 2 provides an extensive review of the existing literature on single-molecule experiments addressing RecA and RAD51, the core component of HR in prokaryotic and eukaryotic organisms. In HR, RecA and RAD51 assembles on single stranded DNA, pair with the homologous sequence on the sister chromosome, perform the strand exchange reaction and finally disassemble from the heteroduplex DNA. All these biochemical reactions are coordinated by ATP-binding, conformational transformations of the protein and ATP hydrolysis. Single-molecule approaches, such as optical and magnetic tweezers, FRET spectroscopy and fluorescence microscopy have isolated and studied these molecular mechanisms. Despite years of intense research on these topics many inconsistencies and open questions, discussed in the chapter, still remain.

Chapter 3 describes the technology used in this thesis: a combination of DNA-manipulation (optical tweezers), direct protein-visualization (single-molecule fluorescence microscopy) and microfluidics technologies. First I describe the benefits and the field of application of this technical approach for the study of DNA-protein interaction. Also I describe some experiments where I studied the limit of protein localization on a single DNA molecule as a function of the applied tension

Chapter 4 describes the biochemical methods and procedures to generate single-stranded DNA molecules for single-molecule experiments using optical tweezers. Many biochemical methods are available to modify ds-DNA molecules, but protocols for the generation of ssDNA are much more limited. I also discuss some of the practical difficulties in handling ssDNA molecules using optical tweezers and methods to preserve their integrity during the single-molecule experiment.

Chapter 5 is an in-depth single-molecule study of the mechanism of RAD51-nucleoprotein filament assembly on both ssDNA and dsDNA. Filament assembly is shown to be highly selective, with a marked preference for ssDNA over dsDNA. Using the capability of counting individual RAD51 proteins we visualized and quantified the nucleation and growth of RAD51 filaments. I revealed that RAD51 nuclei are heterogeneous in

size, depending on their aggregation state in solution. A physical model has been developed that quantitatively described our experimental observations. Moreover, the effect of BRC4, one the RAD51-binding subunit of the breast cancer tumor suppressor BRCA2 on RAD51 filament assembly has been studied.

Chapter 6 discusses several dynamic aspects of the RAD51 nucleoprotein filament. First I describe a striking difference in the behavior of RAD51 filament when comparing two naturally occurring variants of RAD51 (K313 and Q313). I observe that this biochemical modification triggers RAD51 to slide on the ssDNA via a mixed diffusion-hopping mechanism. Using dynamic force-spectroscopy we also investigated how tension affects the structure of the RAD51 nucleoprotein filament. By performing out of equilibrium measurements we were able to measure the free energy difference between the conformations of RAD51.

Chapter 7 presents the DNA-binding and bridging mechanism of XRCC4 and XLF, two crucial component of the non-homologous end joining pathway (NHEJ). I observed that the formation of XRCC4-XLF filaments does not alter the mechanical properties of DNA, giving us hints on the strategy that XRCC4 and XLF employs to engage DNA. The DNA-binding mode of the XRCC4-XLF filament is highly complex and is characterized by sliding, pausing and filament rearrangements. Finally, we developed an innovative assay to study the DNA end-bridging activity of XRCC4-XLF.

2 HOMOLOGOUS RECOMBINATION

SINGLE-MOLECULE VIEWS ON HOMOLOGOUS RECOMBINATION

All organisms need homologous recombination to repair DNA double-strand breaks. Defects in recombination are linked to genetic instability and to elevated risks in developing cancers. The central catalyst of homologous recombination is a nucleoprotein filament, consisting of recombinase proteins (human RAD51 or bacterial RecA) bound around single-stranded DNA.

The biological role of the nucleoprotein filament consists in finding the homologous DNA sequence in the sister chromosome and exchange the genetic information in order to re-estabilish the genetic integrity. Over the last two decades, single-molecule techniques have provided substantial new insights into the dynamics of homologous recombination. Here we survey important recent developments in this field of research, we highlights the contradictions of the current experimental evidence and provide an outlook on future developments and open questions.

2.1 INTRODUCTION

2.1.1 Double-stranded DNA breaks and Homologous Recombination

Ultimately, the biological essence of life consists in the accurate transmission of genetic information from one generation to the next. Preserving genome integrity against DNA damages is therefore crucial for living organisms.

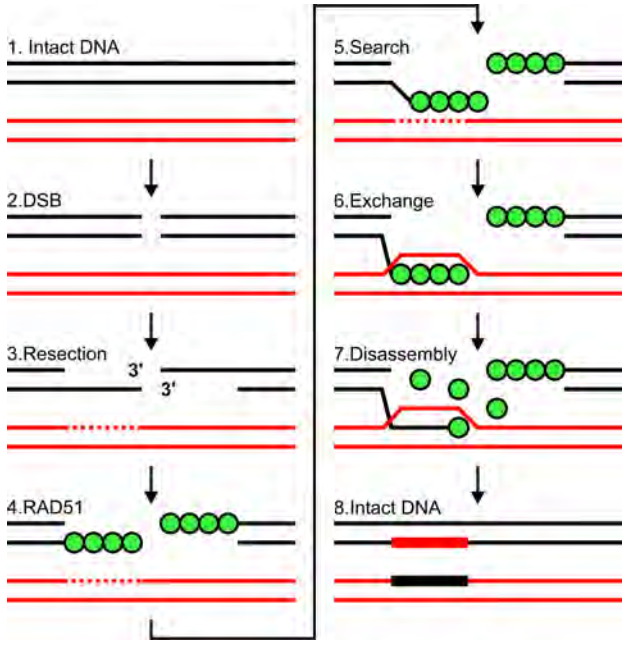

Figure 4.: **Homologous recombination pathway.** [1] Two intact identical copies of the genome in somatic cells in S and G2 phases. [2] Occurrence of a DNA double-stranded break (DSB). [3] End-resection creates a 3' single-stranded DNA tail. [4] RAD51, assisted by recombinase mediators assembles in form of filaments on ssDNA. [5] Homology search: the nucleoprotein filament finds the homologous DNA sequence. End of the pre-synaptic phase. [6] Sequence homology is found and a stable complex is formed. One of the strands of the target DNA (red) is displaced and interacts with the secondary-binding site of the recombinase filament. End of synaptic phase. [7] RAD51 unbind from the DNA duplex, triggered by ATP hydrolysis (Start of post-synaptic phase). [8] Cross-over structure is resolved and genomic integrity is re-established.

Among the different types of DNA damage encountered, DNA double-strand breaks (DSB) pose a serious threat to cell survival. If left unrepaired they can lead to chromosomal fragmentation and genomic rearrangements, a hallmark of many cancers [73, 80]. DSBs are predominantly caused by chemical and environmental agents such as reactive oxygen species and ionizing radiations. In addition, DSBs can be induced endogenously to generate genetic diversity during meiotic recombination. One of the fundamental cellular strategies to repair DSBs is homologous recombination (HR). In somatic cells, HR is active during the S and G2 phase of the cell cycle [71], when sister chromatids are available to serve as a template for the recovery of the genetic information. HR is a highly regulated and accurate process, which is able restore chromosome integrity without losing genetic information [142, 184]. The basic scheme of HR is similar across all kingdoms of life and can be divided in three stages [71, 142]: pre-synapsis, synapsis and post-synapsis (see Figure 4).

Double-stranded breaks (DSB) and Homologous Recombination

Steps in HR pathway

In pre-synapsis, the broken DNA ends are processed by a specialized set of proteins (end-resection machinery) that create long 3'-tailed single-stranded DNA (ssDNA) overhangs. Single-stranded DNA binding proteins, such as Replication Protein A (RPA) in humans, immediately cover the exposed ssDNA to protect it from degradation [180]. Next, recombinase proteins (RAD51 in eukaryotes, RecA in E. coli), assisted by recombinase mediators (in human: tumour repressor proteins BRCA2 and RAD51 paralogues such as RAD51B, RAD51C, RAD51D, XRCC2, and XRCC3), displace RPA and form nucleoprotein filaments (NPF) on the ssDNA overhangs [83, 98, 75]. The NPF, in turn, is able to find (homology search) and pair (strand exchange) with the homologous section on the sister chromosome. ATP-hydrolysis triggers RAD51 disassembly, creating a joint-structure that serves as priming site for DNA synthesis and recovery of the genetic information. Finally, the joint intermediates are resolved and ligated, restoring two intact chromosomes.

Medical relevance of DNA repair recombination

Malfunctions in DNA repair processes can cause chromosome instability [73], one of the causes of cancer formation [119]. In addition, mutations in HR genes have been linked to various forms of hereditary diseases [73]. For example, biochemical and genetic studies pose the process of nucleoprotein-filament formation at the centre of a complex network of mediators that include important tumour-suppressor proteins such as BRCA2 and various helicases (BLM, FANCJ, RecQ5), which are implicated

in different forms of tumours [108, 29, 73]. Understanding the dynamics and the regulation of the RAD51 nucleoprotein filament is therefore not only important for understanding homologous recombination but can also provide insights in the molecular causes underlying carcinogenesis.

2.1.2 Structure and conformations of human RAD51

RecA and RAD51: at the core of homologous recombination

Recombinase proteins RAD51 (human) and RecA (E. coli) are considered to be the central HR catalysts, since they are involved in the core step of the recombination process, the exchange of DNA strands between homologous sections of the chromosomes [14]. RecA and RAD51 share structural and functional similarities but also some remarkable differences. Both RAD51 and RecA are globular proteins with a molecular weight of 38 kDa and DNA-stimulated ATPase activity [10, 166].

The RAD51 nucleoprotein filament

These recombinase proteins form regular, right-handed, helical filaments around ssDNA and dsDNA [190]. Human RAD51 and E. coli RecA bind to both ssDNA and dsDNA in the presence of ATP with a stoichiometry of one monomer per 3 nucleotides [14, 166, 128], resulting in a helical structure with approximately 6 proteins per helical turn [190]. X-ray crystallography and electron microscopy studies have provided snapshots of the dynamic rearrangements of nucleoprotein filament, demonstrating the existence of distinct conformations depending on nucleotide bound to the ATPase active site, that is located at the monomer-monomer interface within the recombinase filament [33, 38, 134]. In the case of human RAD51, nucleoprotein filaments formed in the presence of ssDNA and ATP, exhibit an extended conformation, characterized by a pitch of 9.9 nm [190], which results in an average axial rise per base of 0.51 nm, approximately 50% longer than B-form dsDNA (0.34 nm). RAD51-ssDNA filaments assembled in the presence of ADP or ATP-γ-S, are significantly shorter, with a helical pitch of only 7.6 nm [190] (average axial rise per base is 0.39 nm). The structural difference between these two conformations consists in the position of the N-terminal domain, which undergoes a rotation from the extended ATP-bound state to the compressed ADP-bound form [190].

RecA, the bacterial homolog of RAD51, displays similar structural properties, also showing two different conformations with and elongated and compressed pitch (10 vs 8 nm) according to the nucleotide bound (ATP vs ADP) [128]. One of the striking biochemical differences between RAD51

and RecA consists in the interplay between their structural and functional features and the nucleotide cofactor bound at the monomer-monomer interface. ATP-γ-S, for example, activates the RecA recombinase filament for strand exchange by keeping it in the extended conformation. On the contrary, the RAD51 filaments on DNA bound in the presence of ATP-γ-S display a compressed structure, likely resembling and intermediate state before disassembly. In the case of RecA the two conformations clearly display very different biochemical functions: ATP-bound-extended filaments are able to perform strand exchange with high efficiency, while the ADP-bound-compressed form is less active, and might represent an intermediate state before disassembly [128].

The RecA nucleoprotein filament

A recent X-ray crystallography study on RecA [33] has revealed important insights on how ssDNA and dsDNA are engaged by the recombinase filament. In the RecA-ssDNA complex the average base-to-base distance is 0.51 nm, exactly 50% longer than in the B-DNA form (0.34 nm). The inter-base distance, however, is not uniform throughout the filament. Every RecA monomers binds three bases. Within the triplet, base stacking is observed between two bases, resulting in a B-DNA-like conformation, with a slightly elongated axial rise of 0.42 nm. The last base of one triplet and the first one of the next shows a significant local stretching (0.78 nm) and no base stacking interactions. In addition, RecA has a secondary binding site (SBS), whose role in strand exchange is still unclear. This secondary binding site binds ssDNA with higher affinity than dsDNA. A possible role for the SBS is therefore to interact with the ssDNA strand that is displaced during strand exchange [104, 103, 77] and stabilize the nascent strand exchange complex.

Molecular insights in strand exchange reaction catalyzed by RecA

Although these structural studies provide insights in HR with atomic resolution, only static snapshots of some of the reaction intermediates are available. Isolating, addressing and quantifying the dynamic features of this complex biophysical process is fundamental to obtain a detailed knowledge of the HR repair process. Over the past two decades, DNA-protein interaction studies have been revolutionized by the development and application of single-molecule techniques [25]. These approaches are very well suited for resolving the dynamics of complex and heterogeneous biological transitions [25]. The HR process and in particular recombinase proteins (RecA and RAD51) have been under intense study using these novel methods. In this review we will provide an overview of the methods

Single-molecule approaches and the study of HR

used, experiments done and an outlook of what can be expected in the years to come.

2.1.3 Single-Molecule Techniques for studying DNA-protein interactions

In the last two decades a substantial advancement has been made to develop and apply novel technologies for providing a quantitative description of DNA-protein interactions. The field of single-molecule technologies, in particular, experienced a tremendous increase in its importance. Here we will briefly discuss the three classes of single-molecule techniques that have been most successfully applied to HR.

Single-molecule DNA manipulation

The first class is based on the mechanical manipulation of individual DNA molecules using optical [117] or magnetic tweezers [45]. Using these approaches, the interaction between proteins and DNA is followed by monitoring the changes in the mechanical properties of the DNA substrate, such as the contour or the persistence length (see Figure 5). In both methods, ssDNA or dsDNA needs to be attached to force transducers. In all these experiments, an individual single-stranded (ssDNA) or double-stranded DNA (dsDNA) molecule is attached from its extremities between two surfaces, one of them acting as force transducer. In magnetic and single-optical tweezers the two surfaces consist of a micron-sized bead and a glass slide or a micropipette. For dual-optical tweezers the DNA molecule is directly attached to two micro-spheres. The extension of the DNA and the tension applied to it can be measured and controlled with high precision (on the nanometer scale and sub-piconewton resolution). The key difference between the two techniques is the physical nature of the bead manipulation mechanism.

Optical Tweezers

In an optical tweezers instrument, the tight focus of a near-infrared laser beam generates a three-dimensional trap due to the momentum transfer from the laser light to the microsphere [7]. In this way, transparent, μm-sized spheres can be stably held. Optical tweezers are currently capable of distinguishing mechanical changes in length of the DNA molecule with Ångstrom precision [148, 1] and apply forces as high as high as hundreds of piconewtons [120].

In a magnetic tweezers instrument an electromagnet or permanent magnet is mounted on a motorized stage in close proximity to the sample. The

DNA is attached with one end to the surface of the microscope slide and with the other end to a paramagnetic microsphere.

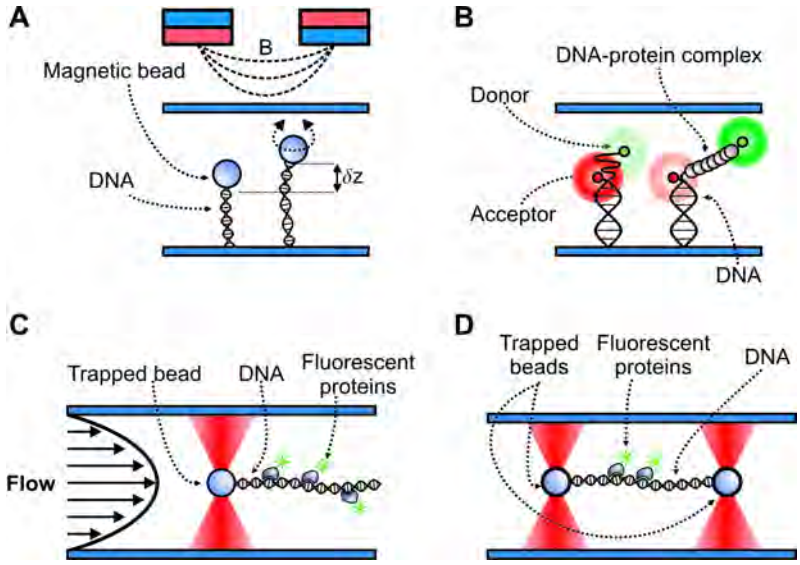

Figure 5.: Single-molecule techniques for studying homologous recombination. [A] Magnetic tweezers scheme. A pair of magnets is used to extend and rotate a DNA molecule tethered between the glass and the paramagnetic bead. Protein binding inducing mechanical modifications of the DNA structure can be monitored in real-time following the change in twist or end-to-end length of the molecule. [B] Single-molecule FRET spectroscopy. A duplex DNA containing a single-stranded DNA overhang is labelled with a donor-acceptor fluorophores pair. The formation of a DNA-protein complex results in a change in distance between the FRET-pair and a concomitant reduction in FRET efficiency. [C] Optical tweezers combined with DNA-flow stretching and fluorescence microscopy. A DNA molecule is attached via a single-end to a optically trapped bead. The drag caused by the flow keeps the DNA in a elongated configuration and a non-uniform tension is applied along the DNA molecule. Binding and translocation of fluorescent proteins can be detected using fluorescent microscopy. [D] Dual-optical trapping and fluorescence microscopy. A single-DNA molecule is attached to two optically trapped beads and hold in an extended configuration while the force applied along the DNA applied uniformly and measured with sup-pN precision. Binding and unbinding of fluorescent proteins can be resolved via fluorescence microscopy.

The magnetic field acting on the magnetic dipole of the paramagnetic microsphere allows the extension and coiling of single biopolymers attached between the glass surface and the microsphere [154, 158]. Key advantages

Magnetic Tweezers

of magnetic tweezers over optical tweezers are the possibility to coil the DNA [96] and that many tethers can be followed in parallel [45]. Recently, methods to directly measure the torque acting on the DNA have been devised [97]. In terms of sensitivity, the capability of magnetic tweezers of achieving sub-nm resolutions has been only recently demonstrated using more sophisticated bead imaging schemes [89]. Also, the forces that can be reached using magnetic tweezers are about an order of magnitude smaller than what can be achieved with optical tweezers.

Dual DNA molecule manipulation

In an extension of the optical and magnetic tweezers methods discussed above, several laboratories have successfully embarked on methods that allow the manipulation of two DNA molecules at the same time, in order to study (protein-mediated) interactions between the two DNA molecules. So far, an optical tweezers instrument equipped with four independently steerable optical traps has been developed and applied to study the protein-mediated bridging between different DNA molecules [42] and to localize individual proteins bound to DNA [123]. More recently, this approach has been further expanded, using a combination of optical and magnetic tweezers, enabling the controlled application of torque in dual DNA-manipulation experiments [45].

Single-molecule fluorescence microscopy

A second class of single-molecule approaches to study DNA-protein interactions is single-molecule fluorescence microscopy, in particular employing single-pair Förster Resonance Energy Transfer (spFRET) (see Figure 5). FRET is a photo-physical phenomenon in which two fluorescent molecules (commonly referred as the donor-acceptor pair) exchange energy through a non-radiative process [62]. The efficiency of FRET is dependent on the nature of the two fluorophores (in particular the overlap between the fluorescence spectrum of the donor molecule and the absorption spectrum of the acceptor) and, in a highly non-linear fashion on the distance between donor and acceptor (which needs to be less than 10 nm for FRET to occur). A widely applied scheme to study DNA-protein interactions using spFRET consists in labelling the protein or the substrate of interest at a specific position with a donor-acceptor pair and monitor the change in FRET efficiency upon the progression of the biophysical interaction [140, 107] (see Figure 5). In addition, experiments and theory both validated the use of spFRET as a molecular ruler capable of resolving movements equivalent to single base pairs [74]. spFRET has been applied successfully to helicases [187], DNA polymerases [144] and protein movement on ssDNA [63].

A third and rapidly expanding category of single-molecule approaches involves combinations of DNA manipulation and visualization using fluorescence microscopy. Examples of such methodology include fluorescence microscopy combined with DNA combing or flow stretching [19]. In this approach, single DNA molecules are covalently attached with one end to a functionalized glass surface and extended by the viscous drag generated by the buffer-flow. Fluorophores bound on the DNA or fluorescently labelled DNA-bound proteins, can be visualized using Total Internal Reflection Fluorescence microscopy (TIRF-M). This approach can be expanded using "DNA curtains", a specialized patterned attachment protocol that allow multiple DNA molecules to be bound next to each other along lines perpendicular to the solvent flow, which is excellent for massive parallelization of the experiments [57]. Also, very recently, it has become possible to apply this method to ssDNA substrates using a dual attachment strategy [56]. A limitation of surface-based assays is the vicinity of the glass surface to the DNA that can cause unwanted electrostatic interactions and the inability to control the conformation of the DNA in a dynamic way. DNA flow stretching was therefore combined to optical trapping [130] (see Figure 5). In this way, only a single DNA molecule can be followed at a time. The method is, however, compatible with microfluidics, allowing rapid buffer exchange, which permits fluorescence imaging in the absence of a background of fluorophores freely diffusing in solution and the controlled triggering of the biochemical reaction [22].

Combining DNA manipulation using flow-stretching and single-molecule fluorescence microscopy

The most sophisticated approach in this category involves tethering a single DNA molecule between two optically trapped microspheres using dual-trap optical tweezers. In this way, it is possible to control both the tension and the extension of a single DNA molecule in a precise and dynamic fashion. These features are essential for high-resolution and high-sensitivity fluorescence imaging. It has been demonstrated that this approach allows manipulation of a DNA molecule with sub-piconewton resolution while visualizing individual fluorescent molecules bound to it. Hence allowing determination of the oligomeric state as well as their physical location with sub-10-nm accuracy (see Figure 5) [25, 36, 173].

Combining DNA manipulation using optical tweezers and single-molecule fluorescence microscopy

2.2 SINGLE-MOLECULE EXPERIMENTS

2.2.1 Assembly of the nucleoprotein filament

In the presynaptic phase of HR, the formation of the nucleoprotein filament is the first step catalysed by RecA and RAD51 recombinases [142]. A two-step mechanism involving nucleation and growth has been proposed for the formation of a recombinase filament [30] but a precise quantification of both nucleation and growth rate has not been possible using standard bulk biochemical assays. In addition, to obtain a full understanding of recombinase protein binding to nucleic acids would require a detailed knowledge of the different oligomeric species present in solution [161], their aggregation kinetics and their respective DNA-binding properties.

In the following section we will examine and discuss the major findings on the dynamic assembly of the nucleoprotein filament provided by single-molecule technologies. The assembly of both RecA and RAD51 recombinase filaments on single- and double-stranded DNA was addressed using a diverse set of single-molecule techniques, including magnetic and optical tweezers, FRET spectroscopy and single-molecule fluorescence microscopy.

Magnetic tweezer experiment on RAD51 and RecA filament assembly

Using magnetic tweezers, changes in end-to-end length of DNA covered with RecA or RAD51 nucleoprotein filament were measured in real-time (see Figure 6, 7 and 8) [172, 169]. Monte-Carlo simulations were performed to extract kinetic parameters characterizing RAD51 and RecA assembly [167]. On basis of these simulations, the authors proposed that RAD51-filament formation is characterized by: (i) a low ratio between growth and nucleation rate (cooperativity), approximately 200 for RAD51; (ii) pentamers of RAD51, preassembled in solution, being the units of filament nucleation and growth; (iii) RAD51-filament assembly being independent of the DNA being double or single stranded and the tension applied to the DNA. The same experimental method and analysis were also applied to E. coli RecA, and its filament formation mechanism on ssDNA was addressed [172].

Similarly to RAD51, the data suggested that RecA assembly on ssDNA occurs by nucleation and growth of preformed multimers of RecA (hexamers) that form filaments with low cooperativity (between 10 and 20). In another, technically innovative magnetic-tweezers study [6], RAD51 bind-

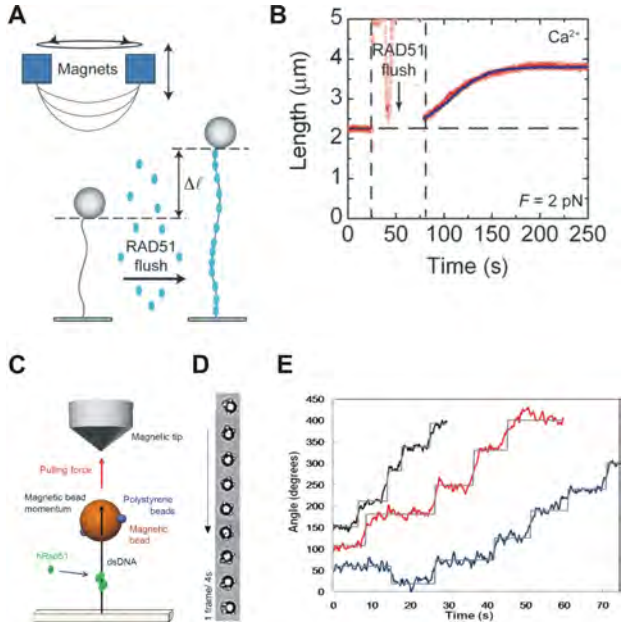

Figure 6.: RAD51 filament formation at the single-molecule level using DNA manipulation. [A] Assembly of RAD51 on ssDNA using magnetic tweezers. Binding of RAD51 induces a change in the end-to-end distance. [B] Example of an experimental trace. The increase in DNA length can be analysed to estimate the parameters of RAD51 filament formation (nucleation and growth rate). [C] Freely rotating magnetic tweezers. [D] Image sequence showing the bead rotation produced by the binding of RAD51 on dsDNA. [E] Rotation traces at different RAD51 concentration show a stepping behaviour with a typical step size of 65°(black-10 nM, red-75 nM, blue-50 nM). Figures reprinted from [169, 6].

ing to dsDNA was monitored by tracking changes in dsDNA twist instead of length. According to structural studies, the binding of RAD51 results in the elongation and unwinding of duplex DNA: each RAD51 monomer binding to dsDNA increases dsDNA length with 0.17 nm and unwinds it of approximately 45° [190].

To monitor the rotation of the magnetic bead along the vertical axis in response to RAD51 binding, a magnetic field parallel with the DNA was applied (see Figure 6). A smaller microsphere was attached to the paramagnetic bead connected to the DNA, allowing tracking of bead rotation with an accuracy of 5° (see Figure 6). Using this method, individual rotation steps of 65° were observed (see Figure 6), inconsistent with preassem-

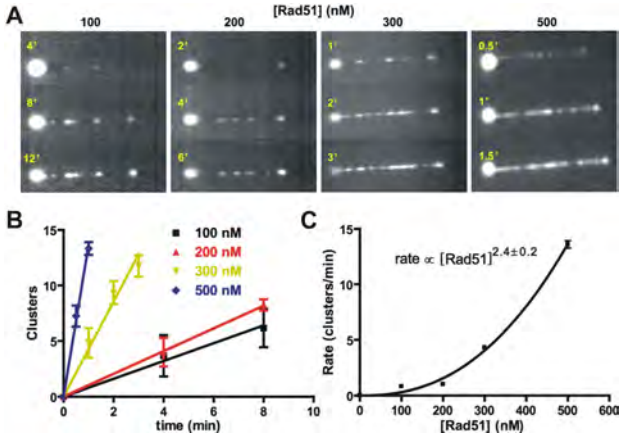

Figure 7.: RAD51 filament formation at the single-molecule level using fluorescence visualization. [A] Single optical trapping combined with flow stretching to visualize the nucleation of RAD51 on dsDNA. [B] Nucleation rate as a function of time, showing a linear dependence on the time. [C] Nucleation rate as a function of free RAD51 concentration. The experimental data is fitted with a a power-law. Figures reprinted from [72].

bled RAD51 pentamers being the active species for filament growth [169]. On basis of these observations the authors proposed a new model, where individual RAD51 monomers are responsible of the filament growth step.

Single-molecule experiment on RecA filament assembly

A single-molecule approach able to directly visualize the nucleoprotein-filament assembly made use of optical tweezers in combination with DNA flow-stretching and fluorescence microscopy [55] (see Figure 7). A DNA molecule attached to a micron-sized bead held in an optical trap was extended using buffer flow. The instrument consisted of a micro-fluidic device that allow introduction of each reaction component separately using laminar flow. In this way it was possible to expose the DNA molecule to a buffer containing fluorescently labelled RecA for a defined duration. Following this incubation step, the molecule was repositioned in an observation channel, which did not contain fluorescent RecA. Using this experimental assay, it was for the first time possible to directly visualize individual RecA nuclei on dsDNA and to quantify the rate of nucleation (of the order 10^{-6} nuclei s^{-1} bp^{-1}) (see Figure 8) It was observed that the rate of nucleation, the rate-limiting step of filament formation, depends on RecA concentration with a power-law (see Figure 8). Fitting the experimental data with the equation $k_{nucl} = k_0 [RAD51]^n$ indicated that the

nucleation step involves approximately 4 to 5 RecA monomers (n=4.5±0.5). In addition, performing multiple, subsequent incubation and visualization cycles allowed distinguishing the RecA-filament nucleation phase from the growth phase.

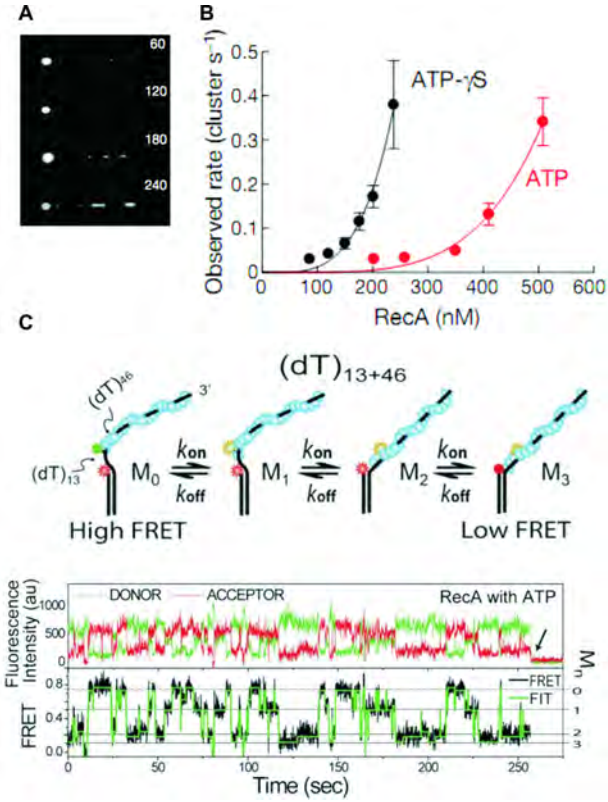

Figure 8.: RecA filament formation at the single-molecule level.[A] Optical tweezes combined with flow stretching for studying RecA assembly on dsDNA. Snapshots taken at different incubation times show an increase in fluorescence intensity due to RecA binding. [B] RecA nucleation rate at different RecA concentrations in the presence of ATP (red dots) and ATP-γ-S (black). Fit corresponds to the functions $k_{nucl} = k_0 [RecA]^n$. [C] Schematic representation of FRET-assay for determining the extension unit of RecA filament assembly. A donor-acceptor FRET pair allowed detecting RecA dynamics at the 5'-end of the filament in real-time. [D] Four distinct FRET states were observed. Fast and reversible transitions occurred between states, indicating association and dissociation of RecA. The transitions between FRET states occurred between neighbouring states ($M_i \rightleftharpoons M_{i+1}$), indicating assembly and disassembly of RecA monomers. Figures reprinted from [55, 84].

Growth occurred with a rate of 2 RecA monomers per second, indicating that the cooperativity of RecA-dsDNA filament formation is characterized by a high cooperativity, of the order 10^6.

The same experimental protocol was applied to study the assembly mechanism of human RAD51 [72]. Intriguingly, important differences were reported. First, for RAD51 nucleation was shown to involve 2 to 3 RAD51 monomers. Second, RecA requires only a few nucleation points that grow cooperatively to produce μm-long segments of continuously coated DNA molecule. RAD51, because of its lower cooperativity, reaches complete coverage of the DNA starting from many more nuclei that show limited growth. This observation is a clear indication that the cooperativity of RAD51-dsDNA filament formation is one or two orders of magnitude smaller that of RecA.

RecA filament formation using FRET spectroscopy.

The RecA-filament-formation mechanism was addressed at high temporal resolution using spFRET [84], with a donor and acceptor fluorophore attached to ssDNA in order to measure ssDNA conformational changes upon filament formation. Without RecA bound, the ssDNA is in a coiled configuration, with donor and acceptor close, resulting in a high FRET efficiency (see Figure 8). RecA binding to ssDNA leads to the formation of a stiff, elongated nucleoprotein filament, resulting in an increased distance between donor and acceptor and consequently a lower FRET efficiency. Attaching the fluorophores to different locations on the DNA, permitted to compare the kinetics of filament formation on the 3′- and the 5′-end of the ssDNA. The authors observed in the first place that stable filament formation only took place only on substrates with a single-stranded overhang exceeding 17 nucleotides. Substrates with shorter ssDNA segments allowed only the transient formation of DNA-protein complexes. The hypothesis connected to this observation was that nucleation clusters composed of smaller structures than RecA pentamers are not stable enough to form a seed for filament formation. Next, RecA binding and unbinding rates were determined for both the 3′- and 5′-ends. These measurements indicated two interesting aspects of RecA-ssDNA interaction: (i) the unbinding rate is equal at the two ends and (ii) RecA filament formation is faster at the 3′-end. The differential assembly speed of RecA at opposite ends, rather than in differences in the disassembly kinetics is therefore the reason of polar growth displayed by RAD51. Finally, the detailed analysis

of the FRET traces allowed defining that filament extension occurs via the addition of RecA monomers.

Very recently, a substantial advancement towards the understanding of RecA filament assembly has been made. Using a novel assay, Bell and coworkers [12] monitored RecA nucleation and growth on single-stranded binding protein (SSB)-coated ssDNA. First, a biotinylated dsDNA molecule was attached to a streptavidin-coated glass coverslip, it was subsequently denatured using an alkaline solution and then saturated with fluorescent SSB. Fluorescent RecA was introduced in the flow-cell and, after a rinsing step, fluorescence visualization was used to inspect the formation of a RecA-ssDNA complex. Successive cycles of incubation, buffer exchange and fluorescence visualization highlighted the complex mechanism of RecA filament formation on SSB-coated ssDNA. A first striking observation was that RecA nucleation was observed to increase quadratically with respect to RecA concentration. This suggested that RecA nucleation on SSB-coated ssDNA requires a critical nucleus composed of a dimer, rather than of a pentamer, as reported by the same group in an earlier study on dsDNA [55]. Also, the effects of recombinase mediators such as RecO, RecF and RecR (RecFOR complex) were tested at the single-molecule level using a dual optical tweezers assay combined with fluorescence microscopy. The analysis of these interactions highlighted the interplay between SSB dynamics on ssDNA and RecA nucleation and filament assembly.

RecA filament formation using DNA manipulation and fluorescence microscopy.

The authors proposed that RecA is in fact unable to form filaments on SSB-coated ssDNA and its assembly relies uniquely on the transient local unwrapping of SSB tetramers from the ssDNA. The role of RecOR and RecFOR complex is therefore to destabilize the ssDNA-SSB complex, giving the opportunity to RecA to form the nucleoprotein filament and allow the sequential steps of homologous recombination to take place. As described, several controversies have emerged from the various single-molecule studies of recombinase filament formation and a definitive molecular model describing the kinetics of filament formation is still lacking. Past studies using fluorescence spectroscopy technique [30] addressed the RecA-ssDNA interaction. It was found that increasing RecA protein concentrations does not affect the rate of binding to a fluorescent single-stranded polynucleotide [30]. The hypothesis that was put forward to explain this observation was that the formation of a RecA-ssDNA nucleus is preceded by concentration-independent activation step (either a conformational change

of the RecA protein or the dissociation of "active" RecA species from a RecA aggregates in solution). The application of single-molecule techniques allowed the direct visualization and quantification of RecA nucleation step and how it varies as a function of free RecA concentration, disproving the former hypothesis. Currently, several experiments have provided evidence supporting a nucleation step of RAD51 and RecA that requires three or more proteins bound to the DNA, irrespective if ssDNA or dsDNA is used as reaction substrate. A consensus over the actual number has not been reached yet, and in addition, a physical and structural explanation for this minimal size requirement is missing. Whether RAD51 and RecA accomplish nucleation starting from preassembled species in solution or through the coincident binding of multiple monomers also remains controversial. In fact neither RecA nor RAD51 exists in solution in a defined oligomeric state in the absence of DNA. The kinetics of recombinase filament self-assembly in solution has been addressed using various technical approaches [161, 122]. It was found that the oligomerization state of RAD51 and RecA is highly sensitive to the environment and to the free protein concentration. In the absences of such knowledge, obtaining a quantitative picture of how recombinase filaments form on nucleic acids is a remarkably challenging task and cannot be properly addressed by the use of bulk biochemical techniques.

Unknowns in nucleoprotein filament formation

In addition, using single-molecule approaches such as magnetic and optical tweezers, it is possible to disentangle the filament growth phase from the nucleation step only if the two kinetic rates are highly separated (high cooperativity) [127]. In magnetic tweezers experiment, for example, the binding of protein to the DNA is monitored by measuring changes in DNA length (or twist), averaging over multiple, simultaneously growing filaments. Techniques employing fluorescence visualization allow discriminating the dynamics of distinct filaments. Fluorescence methods, however, suffer from the high background signal of fluorescently labelled proteins in solution, which makes it very hard to visualize the progress of filament formation in real-time. To overcome this problem, DNA molecules are subjected to cycles of incubation (in a buffer containing fluorescently labelled recombinase) and visualization (in a buffer not containing fluorescent proteins), resulting in only snapshots. In the near future, we believe that improved visualization methods, capable of limiting background-fluorescence, will allow visualization in real-time the formation of RAD51

Future directions

and RecA recombinase filament with single-monomer resolution and finally resolve these unresolved questions.

2.2.2 Conformational transition of the nucleoprotein filament

The interplay between structural and functional properties of recombinase filaments has been intensely studied, in particular by electron microscopy. The general idea that has emerged is that both RecA and RAD51 filaments can adopt two conformations, an extended, active one with a pitch of 9-10 nm and a more compressed one that is at least 20% shorter [190, 47]. The structural heterogeneity present in recombinase filaments is commonly attributed to conformational transition induced by ATP hydrolysis involving the rotation of the C-terminal subunit in RecA or N-terminal one in RAD51 [190]. Interestingly, the two filament conformations have been argued to have different biochemical functions: the extended one is active in performing stand exchange, while the compressed one appears inactive and might represent an intermediate before filament disassembly [23].

Structures and functions of RAD51 and RecA

Since electron microscopy can only provide static snapshots of these conformational changes, single-molecule techniques have been applied to address these dynamics transitions in real time. The mechanical properties of recombinase-DNA complexes were explored for the first time using optical tweezers in a set of pioneering experiments at the end of the 90s in the lab of Bustamante. A remarkable behaviour was observed for RecA-ssDNA filaments assembled in the presence of ADP [69]. Upon successive stretching and relaxing of these filaments, the force-extension curves measured in the optical tweezers displayed notable hysteresis (see Figure 9). Extending the molecule to its contour length required forces up to 15 pN. Reaching this force-threshold resulted in a plateau-like lengthening, followed by a further force increase. The relaxation curve showed a substantial lengthening but a more regular behaviour (see Figure 9). Two alternative interpretations were put forward: (i) stretching the ssDNA induces a transition of the nucleoprotein from the compressed to the extended state or, (ii) free-RecA in solution can associate with gaps opening along the filament in a force-dependent and reversible way. The latter explanation could not be excluded since the experiments were performed in the presence of protein in solution. Later, similar results were obtained in a study using magnetic tweezers [172].

Force affects RecA filament structure

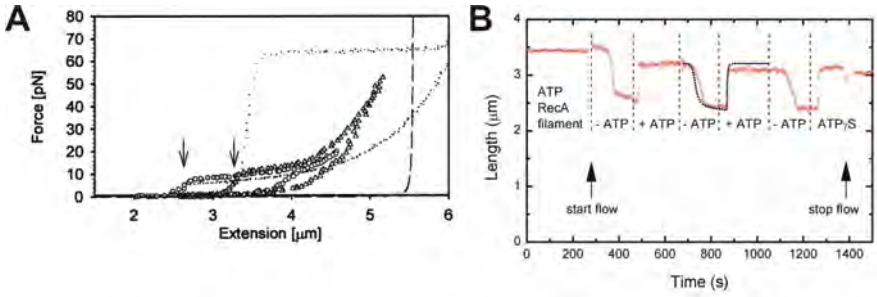

Figure 9.: Conformational transitions within RAD51 and RecA nucleoprotein filaments using DNA manipulation. [A] Stretching and releasing cycles of a single ssDNA molecule in complex with RecA-ADP using optical tweezers. The first stretching curve shows the approaching of the contour length approximately at the extension of 3 μm. At 10 pN a plateau is observed, followed by the stiffening of the molecule. The release curve shows hysteresis, indicating the occurrence of a force-induced conformational transition. [B] A RecA nucleoprotein filament is formed on ssDNA in the presence of ATP. Multiple buffer exchanges containing or lacking ATP induce reversible changes in DNA length. Figures reprinted from [69, 172].

RecA nucleoprotein filaments were assembled on ssDNA in the presence of ATP and Mg^{2+} while the DNA's end-to-end length was monitored at a constant stretching force of 3 pN. Using micro-fluidics buffers containing or lacking ATP could be flushed in reversibly, resulting in elongation or contraction of the DNA with at least 20% (see Figure 9). These experiments were conducted without RecA in solution, confirming that nucleotide exchange modulates the conformation of the RecA filament.

Single recombinase filaments on dsDNA also appear to have different conformations, as has been demonstrated in flow-stretch experiments combined with fluorescence microscopy [136]. In these experiments a fluorescently labelled dsDNA molecule was anchored to a glass surface and RAD51 was flowed into the micro-fluidics chamber. The formation of the nucleoprotein filament was monitored by visualizing the change in length of the dsDNA (see Figure 10). Upon filament formation, the dsDNA length increased, corresponding with the formation of RAD51 filaments in the extended conformation. Removing RAD51 from solution induced a dramatic shortening of the DNA, until a final length in agreement with the compressed conformation was reached.

These results indicated that RAD51 could remain DNA bound in the compressed form a significant amount of time. At high ATP concentrations (2 mM), filament compression as well as disassembly was inhibited (see Figure 10). In addition, applying cycles of rapid buffer exchange between ATP-containing and ATP-free solutions resulted in reversible transitions between compressed and elongated filaments, without RAD51 detaching from the DNA (see Figure 10). This study clearly indicates that also RAD51 filaments can adopt distinct conformations, tightly coupled to the nature of the nucleotide bound. More recently, magnetic tweezers have been used to study whether force can induce conformational transitions in RecA-dsDNA filaments [37]. In this study, single dsDNA molecules were first coated by RecA and then subjected to step-wise force increases and decreases, while monitoring their extension using video microscopy. In the absence of free RecA in solution, rapid (<1 s) force increases (from 40 to 55 pN) were followed by slow (4 nm/s) and continuous elongation of the DNA, lasting more than 100 seconds. This observation indicates that applying force to the filament can induce a conformational transition from the compressed to the elongated conformation, resulting in longer DNA tethers.

ATP-exchange modulates the structure of RAD1 filament

Single-molecule approaches have thus provided hints of the dynamic nature of recombinase filaments. Several studies have confirmed that both RecA and RAD51 form filaments on DNA differing in length and mechanical properties that can reversibly interchange. On one hand, filaments in the compressed conformation (which appears to be inactive in catalysing strand exchange) can be converted to the extended configuration if a high enough ATP concentration is present in solution. On the other hand, tension on the filament also affects filament conformation, indicating the tight coupling between the DNA substrate and the filament structure. Several of the molecular mechanisms underlying the transition between the extended, ATP-bound filament to the compressed, ADP- bound one are unclear.

First of all, what is the temporal coordination between ATP hydrolysis, ADP release and the structural compression step? In addition, what structures is adopted when both ATP and ADP are present within the same filament? Is it possible that heterogeneous structures are present within the same continuous nucleoprotein filament? Furthermore, the quantitative thermodynamic model underlying the transition between these two conformations is not known. Future single-molecule experiments, in con-

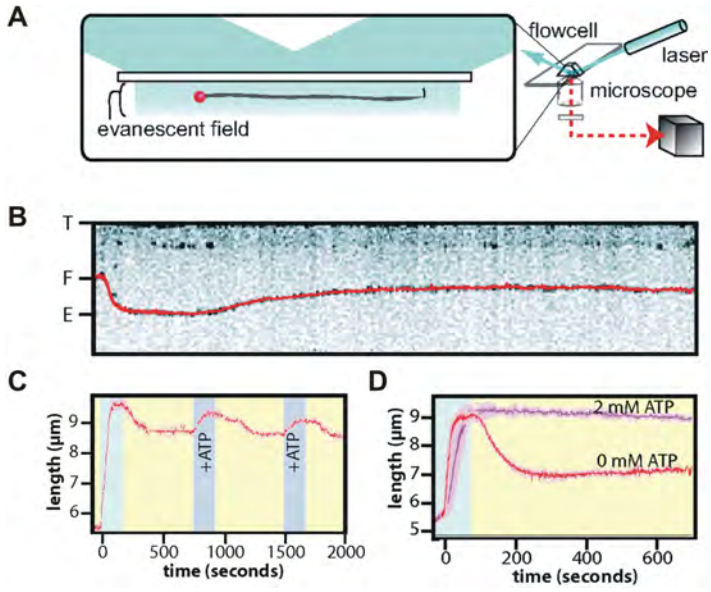

Figure 10.: Conformational transitions within RAD51 and RecA nucleoprotein filaments.[A] TIRF-microscopy combined with flow-stretching. [B] Experimental result showing lengthening and shortening due to nucleoprotein filament assembly and subsequent compression. [C] Cycles of buffer exchange show reversible transition from the extended to the compressed state and vice-versa resulting from the presence of free ATP in solution. [D] If after RAD51 assembly, ATP is depleted from solution (red trace) the nucleoprotein converts into its compressed form (final length 7 μm). When high ATP concentration is supplied to the reaction, the filament compression step is blocked. Figures reprinted from [136].

junction with non-equilibrium thermodynamic modelling will be required to gain further insights in this intriguing aspect of recombinase nucleoprotein filaments and their role in the strand exchange reaction.

2.2.3 Homology search at the single-molecule level

During the homology-search process the recombinase nucleoprotein filament needs to find, align and form a stable complex with the complementary sequence on the sister chromosome. This process needs to be fast and efficient, considering that replication takes approximately 1 to 2 hours (in S.Cervisiae [8]) and in that time a unique sequence has to be found among

the many millions of base pairs available. The strategy and mechanism of homology search is not clear at present. A mechanism purely involving 1-dimensional sliding has been ruled out both experimentally [2] and from theoretical considerations [9].

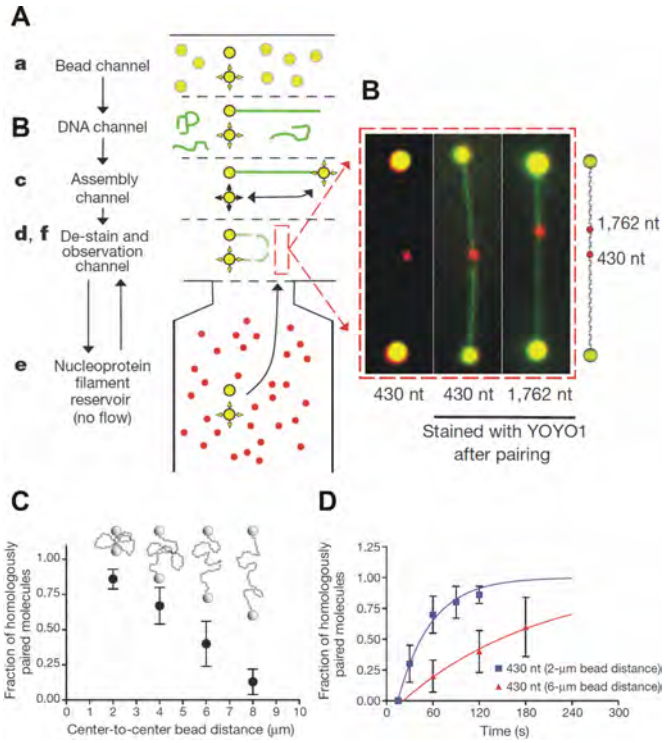

Figure 11.: Homology search mechanism performed by RecA nucleoprotein filaments. [A] Sequential multi-step assembly of the single-molecule assay. [B] Visualization of the end-product of the strand-exchange reaction. Two different fluorescent nucleoprotein filaments were used, of 430 and 1762 nucleotides respectively. Each of them is homologous to a different section of the Lambda DNA molecule used as a template. Fluorescence visualization allows confirming that strand-exchange took place at the correct. [C] The efficiency of the strand-exchange complex formation shows a strong dependence on the conformation of the DNA molecule. At the distance of only 8 μm, corresponding to approximately 50% of the contour length of the DNA molecule the strand exchange reaction is highly inefficient. [D] The speed of homologous recognition is strongly dependent on the DNA conformation. Figures reprinted from [53].

Recently, first direct insights in the homology-search mechanism have been obtained using fluorescence microscopy in combination with dual-trap optical tweezers and microfluidics [53].

In this study, a single dsDNA molecule was manipulated using optical tweezers in order to control its end-to-end length. Using micro-fluidics and an automatized microscope stage (see Figure 11), the trapped DNA molecule was transferred into a reservoir with no buffer flow present, where it was allowed to interact with fluorescently labelled ssDNA molecules pre-incubated with RecA-ATP-γ-S. After a defined incubation time, the DNA was inspected using fluorescence microscopy. Stable strand-exchange complexes were observed by monitoring the binding of fluorescent nucleoprotein filaments to the homologous sequence in the optically trapped DNA (see Figure 11). It was found that the efficiency and speed of homology pairing decreased drastically when the dsDNA was held in an extended conformation. Stretching the target dsDNA (end-to-end length more than 80% of the contour length) resulted in no binding of homologous nucleoprotein filaments. On the other hand, when the target DNA molecule was relaxed (end-to-end length 20% of the contour length), strand-exchange complexes formed practically instantaneously. In addition, homology pairing was found to strongly dependent on the length of the nucleoprotein filament used in the experiment (see Figure 11). This finding appears to be inconsistent with a search mechanism solely relying on 1-dimensional sliding of the nucleoprotein filament along the target DNA. Additional modes of search need to be available, such as hopping [58] and inter-segmental transfer (dissociation and re-association at a distal segments on the DNA) to explain the dependence of search kinetics on tension on the DNA and length of the nucleoprotein filament. The authors proposed a mechanism in which a long RecA nucleoprotein filament is simultaneously in contact with many segments of the target DNA (parallel homology sampling) through short, reversible synapsis events. When the DNA is not stretched, all conformations can be explored due brownian motion, allowing the nucleoprotein filament to interact with distant DNA segments within short time intervals and therefore accelerating the search process.

First single-molecule experiment on homology search

Another set of single-molecule fluorescence experiments addressed the issue of discriminating between homologous and non-homologous sequences in the search process by quantifying how synapse lifetime depends on the

Homologous and non-homologous sequences in the search process

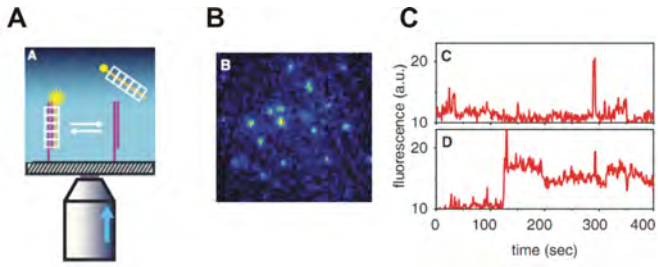

Figure 12.: **Heterologous contacts between RecA nucleoprotein filaments and target dsDNA.** [A] TIRF-based assay for studying the synapsis life-time. [B] Fluorescent image of synaptic complexes. [C] Fluorescence versus time for synapsis events using heterlogous (top) or homologous (bottom) sequences. Figures reprinted from [53, 101].

degree of homology [101]. In the assay used, short dsDNA molecules were anchored to a glass surface while fluorescently labelled RecA-coated ssDNA molecules were introduced. Stable complex formation between target DNA and nucleoprotein filaments were identified by stable and bright fluorescence spots appearing on the glass surface (see Figure 12). It was found that completely heterologous sequences did form complexes with lifetimes of tens of seconds. Fully homologous sequences, on the other hand were found to be even more stable, with lifetimes of hundreds of seconds. In addition, single mismatches were shown to significantly decrease the synapsis stability.

Dual DNA manipulation to study RecA-mediated homology search.

An innovative study, employing the simultaneous manipulation of two DNA molecules, aimed at quantifying the thermodynamics aspects of synaptic complex (see Figure 13) [46]. In that assay, a dsDNA molecule was tethered between two optical traps and subsequently melted by applying a high tension resulting in a tethered ssDNA molecule, [60, 173]. This ssDNA molecule was incubated with RecA in the presence of ATP-γ-S to obtain a stable RecA-ssDNA filament. In addition to optical tweezers, the experimental setup consisted also of magnetic tweezers, used to independently stretch and twist a dsDNA molecule tethered to a glass surface. The ssDNA-RecA complex was brought in contact with the dsDNA and interactions between both DNA molecules were assessed. The first experimental goal was to quantify the interaction between the secondary binding site (SBS) of the RecA filament and the target dsDNA. Positively twisted and uncoiled dsDNA did not interact with the nucleoprotein filament, while

slightly stretched (tension 3.5 pN) and negatively supercoiled dsDNA did interact (see Figure 13).

Increasing negative supercoiling resulted in increased strength and probability of interacting with the nucleoprotein filament. It was proposed that the negative supercoiling makes short segments of ssDNA available by the transient formation of ssDNA bubbles on the target dsDNA. These ssDNA segments, due to their high affinity for the SBS of RecA filaments [103] stabilize the strand-exchange complex. The need for negative supercoiling for observing interactions indicates that the SBS alone is not able to provide the necessary energy for melting the target dsDNA and forming a complex with the ssDNA. Spontaneous DNA breathing and supercoiling, therefore, appear to play important roles in the homology-search process. In order to be tested for homology, the target dsDNA needs to be first opened and distorted substantially from its native B-form structure, resulting in an energy penalty. When homology is found the energy penalty can be overcome by the base-pairing energy that is gained (see Figure 13). This model therefore provides a quantitative framework for the detailed energetic balance leading to successful sequence recognition.

In conclusion, the energetics and kinetics of the reaction intermediates leading to the formation of a stable synapse have been addressed at the single-molecule level. Several aspects of this process, however, are still unclear. In the first place, a quantitative model explaining how DNA conformational dynamic affects the efficiency and the speed of the homology search process is still missing. Secondly, the observation that heterologous DNA molecules can pair with high stability in presence of RecA is in apparent contradiction with the requirement of the homology search process to scan fast through the large amount of non-complementary sequences. In addition the experimental assays employed so far were not able yet to directly visualize the actual process of search and recognition of homology and were rather indirect in detecting the intermediate steps leading to a stable D-loop formation. Furthermore, the relative balance between 1D and 3D diffusive search mechanisms is during homology search it is still unclear. Although a first experiments addressing the thermodynamic aspects underlying the formation of a stable DNA-nucleoprotein complex have been performed, a precise quantification of the lifetime of the intermediates states is required to elaborate a predictive target-search model

Open questions in homology search

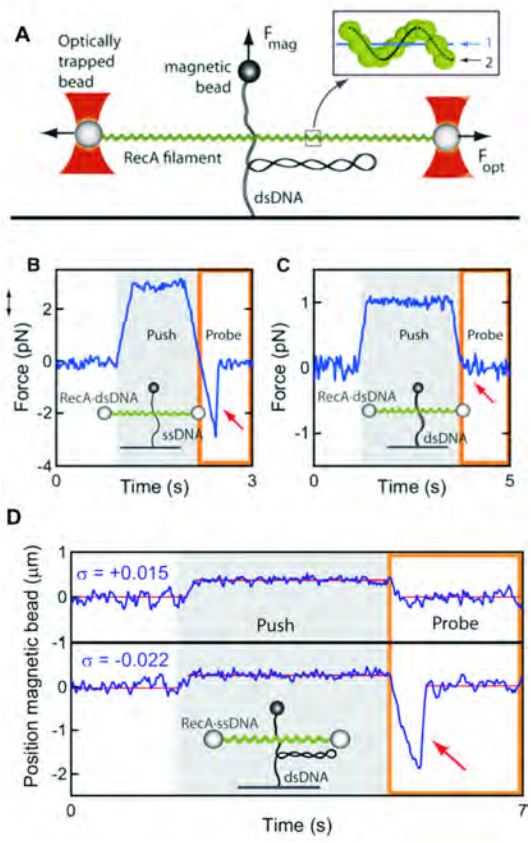

Figure 13.: Dual DNA manipulation to study RecA-mediated homology search. Dual DNA manipulation to study RecA-mediated strand exchange. [A] Dual optical trap is used to manipulate a RecA-DNA (either ssDNA or dsDNA) complex. Magnetic tweezers is used to stretch and twist a second DNA molecule (either ssDNA or dsDNA) is tethered between the glass surface and a magnetic bead. The two DNA molecules can be brought into contact and slided next to each other to probe their interaction. [B] Push-probe experiment between a RecA-dsDNA complex and a ssDNA. A force of 3 pN is required to disrupt the complex. [C] Push-probe experiment between a RecA-dsDNA and dsDNA. No interaction is observed. [D] Effect of positive and negative supercoils of dsDNA molecule. When positive supercoils are applied no interaction is observed (top panel). When negative supercoils are instead applied, a stable complex is formed that require a force of 2 pN to be disrupted. Figures reprinted from [46]

explaining how two complementary sequences find each other in the genomic haystack.

2.2.4 Strand-exchange at the single-molecule level

The nucleoprotein filament, after finding the homologous sequence, catalyses the defining event of the homologous recombination process: the transfer of information between homologous sequences, the strand-exchange. Due to its transient nature, it has been very difficult to isolate and study this key-step of homologous recombination using bulk biochemical or structural methods. Single-molecule approaches have tackled this problem, addressing its molecular mechanism in real-time on single DNA molecules.

The first single-molecule experiment on strand-exchange

In the first single-molecule study of strand exchange, a dsDNA molecule was attached to a glass surface stretched and negatively supercoiled (F=0.5 pN and 35 negative rotations). The changes in twist and end-to-end length of the tethered DNA molecule were monitored while it was strand-invaded by homologous RecA-ssDNA filaments of different lengths (see Figure 14) [168]. Because DNA bound by RecA is elongated and unwound, strand-exchange results in the removal of negative supercoils, which in turn corresponds to a drastic elongation of the torsional constrained DNA. The experiment was performed preassembling RecA on ssDNA using two different nucleotide cofactors: ATP-γ-S and ATP. When ATP-γ-S was present, a gradual and steady increase in the tether length was observed. The final length was compatible with the expected unwinding and stretching due to the invasion of the homologous DNA segment. In fact, both the final elongation as well as the duration of the length increase was linearly dependent on the size of the invading filaments. Therefore it was possible to provide an estimate of the strand-exchange rate, which was found to be approximately 2 bp/s. Substituting ATP-γ-S with ATP resulted in a drastically different behaviour. In this case, after an initial phase in which the DNA length started to increase, a long plateau was observed, followed finally by a decrease in length until the original DNA extension was reached. Two analysis methods were applied: in the first one, the total interaction time was quantified (length increase + plateau + length decrease). This quantity was also found to be proportional to the size of the invading recombinase filament, following the same linear dependence found for the ATP-γ-S.

In the second analysis method, the duration and amount of the length increase phase were quantified. It was observed that they show no correlation with the length of the invading RecA filament. A hypothesis was formulated, in which under ATP-hydrolysis conditions, strand exchange pro-

gresses throughout the homologous region only through a region (strand-exchange window) composed of 80 bases. In this model, the exchange starts at one the invading end (5'), with a rate that is equal to ATP-triggered RecA unbinding. The invading filament locally elongates and unwinds the tethered molecule, increasing the end-to-end distance. At the lagging end, instead, RecA release into solution after ATP hydrolysis and a new heteroduplex is created. Therefore, while strand exchange progresses in ATP-hydrolysing conditions, the end-to-end distance remains constant (see Figure 14). After the reaction is completed, and all RecA proteins dissociated, and three-stranded joint structure is obtained, whose length is identical to the initial length.

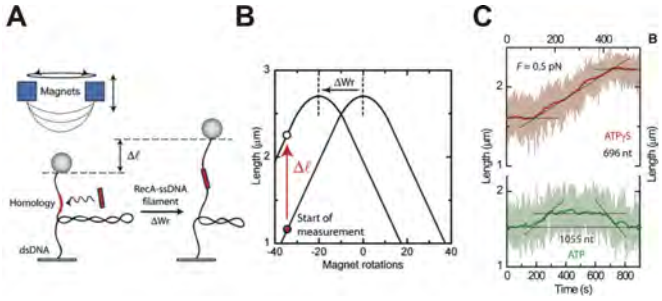

Figure 14.: Strand exchange dynamics at the single-molecule level.[A] A dsDNA molecule is held at constant force and negatively supercoiled. Strand-exchange results in the increase of the end-to-end length and a shift in the rotational offset. [B] Real-time detection of the strand exchange in the absence (red curve) and presence of ATP hydrolysis (green curve). Absence of hydrolysis produces an irreversible lengthening of the DNA. When ATP hydrolysis is permitted the lengthening is only transient and corresponds to a moving strand exchange windows of 80 bases. Figures reprinted from [168].

A FRET-assay to study RecA-mediated strand exchange

In a second study, spFRET, was used to study RecA-catalysed strand-exchange, allowing discrimination between docking of a RecA-ssDNA complex to the target dsDNA and further progress of strand exchange [132]. The experimental configuration used in the experiment is schematically represented in (see Figure 15). Acceptor-labelled RecA-ssDNA nucleoprotein filaments were assembled in the presence of ATP-γ-S and immobilized. Donor-labelled dsDNA was injected into the flow-cell and both donor and acceptor fluorescence intensities were monitored upon donor excitation. An example of an experimental result is shown in Figure 15. After an initial lag phase, the donor fluorescence signal suddenly increased (due to

the docking of the donor-labelled dsDNA). This state quickly converted (during an interaction time Δt_{delay}) to a more stable configuration, characterized by a high FRET efficiency, interpreted to represent the final strand-invaded complex. The design of the DNA substrates allowed concluding that the initial binding of the duplex DNA to the nucleoprotein filament (docking) occurred at different random positions involving just a few bases. The irreversible conversion from this intermediate state to a high FRET value was interpreted as the actual occurrence of the strand exchange reaction. Therefore the distribution of strand-exchange times (Δt_{delay}, the delay time between the formation of the first intermediate and the stable highest FRET configuration) was fitted with a Gamma distribution ($\Delta t^{N-1} e^{-k\Delta t}$), under the assumption that strand exchange involves N hidden rate-limiting steps. Performing this analysis with substrates of different lengths it was found that strand invasion proceeds in steps involving 3 bases and is characterized by a stepping rate of 70 bp/s (see Figure 15). The observation that strand invasion occurs in 3 bp steps is in good agreement with high-resolution structural data [33], which shows that bases in the RecA-ssDNA complex are grouped in triplets. A remarkable behaviour was observed when monitoring the dynamics of the displaced strand of the dsDNA, which is displaced by the nucleoprotein filament. After an initial docking phase (Δt_1), a phase lasting 3 seconds involving rapid fluctuations in FRET efficiency was detected (see Figure 15). The authors proposed that these fluctuations are the results of intermittent interactions between displaced DNA strand and the secondary binding site on the RecA filament.

Open questions in strand-exchange

How recombinase filaments mediate the transfer of strands from one DNA molecule to the other remains largely obscure. The two single-molecule experiments presented, which addressed this key biological step, present important differences and few similarities. First of all, the estimated strand-exchange rates are very different, (70 bp/s in the spFRET experiment and 2 bp/s in the magnetic tweezers study). One possible explanation is that strand exchange is highly sensitive to the torsional constrains imposed on the target DNA molecule (the DNA ends are free in the spFRET experiment and engaged by the glass and bead surfaces in the magnetic tweezers experiment) and the buffer conditions used (100 mM sodium acetate and 10 mM magnesium acetate in the spFRET experiment and 10 mM $MgCl_2$ in the magnetic tweezers experiment). Because stand-exchange can proceed in the absence of ATP hydrolysis, it is likely

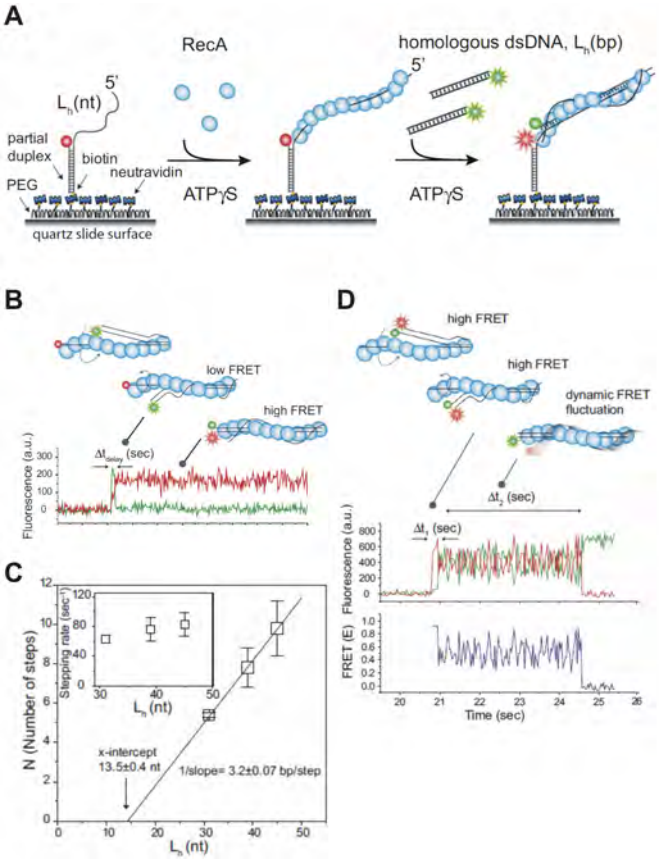

Figure 15.: Strand exchange dynamics at the single-molecule level.[A] A dsDNA molecule is held at constant force and negatively supercoiled. Strand-exchange results in the increase of the end-to-end length and a shift in the rotational offset. [B] Real-time detection of the strand exchange in the absence (red curve) and presence of ATP hydrolysis (green curve). Absence of hydrolysis produces an irreversible lengthening of the DNA. When ATP hydrolysis is permitted the lengthening is only transient and corresponds to a moving strand exchange windows of 80 bases. Figures reprinted from [168] .

that experimental circumstances affecting the stability of the DNA duplex, such as electrostatic screening and supercoiling, play an important role in determining how fast the two strands exchange. Both studies, in fact, point to a model in which the intrinsic dynamic of the double helix plays a crucial role in determining the kinetic of the strand exchange reaction, as anticipated by bulk studies [185, 61, 11]. Finally, what is the driving force

behind the directionality and progression of the strand exchange reaction? How can unidirectional motion be obtained in the absence of ATP hydrolysis between two states having an equal amount of paired DNA bases? Fortunately, due to the rapid development of single molecules techniques, it is expected that these questions can be addressed.

2.2.5 RAD51 disassembly from dsDNA

The final step of HR is the disassembly of recombinase proteins from dsDNA. Disassembly of RAD51 filaments has been examined by the previously described optical tweezers / flow stretching strategies (see Figure 5) [72].

Single-molecule experiments on RAD51 disassembly

In one paper, the filament disassembly was monitored in different buffer conditions after forming the RAD51 filaments in the presence of ATP and either Ca^{2+} or Mg^{2+}, When RAD51 filaments were assembled in Ca^{2+}-ATP conditions and successively exposed to Mg^{2+} (in the presence of ATP) they did not disassemble (see Figure 16). It is well known that Ca^{2+} induces and preserves the active and extended conformation of the RAD51 filament, by blocking ATP hydrolysis [23]. To explain the inhibited disassembly when the filament was transferred from a Ca^{2+} to a Mg^{2+}-containing buffer the authors implicate the slow exchange of the divalent cation bound to RAD51. In contrast, RAD51 filaments formed and visualized in a buffer containing Mg^{2+}-ATP (in the absence of Ca^{2+}), allowing ATP hydrolysis, showed clear signs of filament disassembly: shortening of the dsDNA and disappearance of the fluorescent RAD51. Remarkably, not all RAD51 disassembled from the DNA. This observation was interpreted to be caused by the putatively and surprisingly long time ADP-bound RAD51 filaments remain bound to dsDNA, in the order of tens of minutes. The existence of a long-lived RAD51-bound state subsequent to ATP hydrolysis has important consequences for the progression of the homologous recombination in vivo, blocking the following steps of the reaction. The authors proposed that recombinase mediators such as the translocating motor RAD54 are be needed to fully disassemble ADP-bound nucleoprotein filaments.

High tensions slow down RAD51-disassembly

A different approach, involving dual-trap optical tweezers, quantitative single-molecule fluorescence microscopy and microfluidics provided more detailed insight in filament disassembly. In contrast to the flow-stretching approach discussed above, the use of two optical traps allows applying a

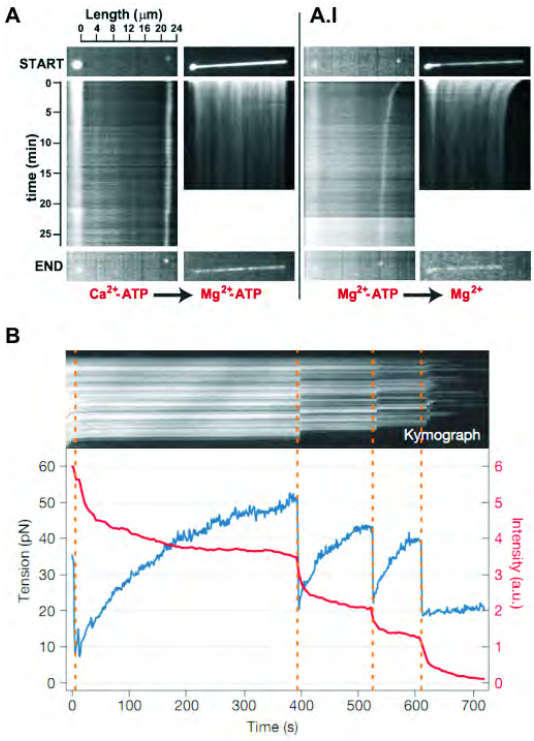

Figure 16.: RAD51 disassembly from dsDNA. [A] Flow-stretching assay for RAD51 disassembly. RAD51 filaments are assembled in the presence of $CaCl_2$ and disassembly is observed in the presence of $Mg(OAc)_2$. A very slow reduction in the DNA-length is observed. [A.I] DNA-RAD51 filaments assembled in the presence of $Mg(OAc)_2$ shows a significant reduction in length when exposed to a buffer lacking ATP. Disassembly does not run to completion. [B] The effect of DNA tension on RAD51 disassembly studied using dual-optical trapping and fluorescence microscopy. RAD51-dsDNA filaments are formed in the presence of $CaCl_2$ and disassembly is observed in $MgCl_2$. The trap position is kept constant. Disassembly induces a fluorescence intensity drop (red line) and a correlated force increase (blue line). Disassembly eventually stalls when the force reaches forces of 50 pN (t∼400s). Releasing the tension to 20 pN (t∼400s) allows the disassembly reaction to reinitiate, generating tension across the DNA. Figures reprinted from [72, 174].

well-defined tension on the tethered DNA, constant over its whole length [174] (see Figure 16). Using this approach, it was observed that high tensions slow down RAD51-disassembly, effectively stalling the process at forces above 50 pN, even under conditions favouring ATP hydrolysis.

Upon a sudden release of the tension, large bursts of RAD51 disassembly were observed. Furthermore, RAD51 disassembly did not occur in a continuous manner, but in bursts, interrupted by pauses, with exponentially distributed duration. A new model for RAD51 disassembly was proposed. (i) ATP hydrolysis occurs throughout the filament, independently from the applied tension. (ii) RAD51 monomers within the filament (and not on one of the ends) will remain DNA bound, irrespective of the nucleotide bound (if ATP or ADP). (iii) RAD51 monomers at filament ends will release from the DNA after ATP hydrolysis. The actual detachment (and not ATP hydrolysis) depends on tension: at low tension monomers will fall off almost instantaneous (until an ATP-bound RAD51 remains on the end), at high tension (50 pN), detachment can be totally inhibited. To explain the force-dependent dissociation rate, it was hypothesized that the complex between dsDNA and a RAD51 monomer on a filament end has to contract, before detachment can take place. This contraction is hindered by applying tension on the DNA. The elastic energy stored in the filament due to the DNA elongation (dsDNA is lengthened of 50% compared to its B-form when in complex with RAD51 or RecA) is therefore the driving force for the release of the nucleoprotein filament from the dsDNA.

Open questions in nucleoprotein filament disassembly

These results might provide an alternative explanation for the incomplete filament disassembly in the flow-stretching experiments discussed above [72]. In that experiment, the DNA was extended using flow stretching with a solution containing a high sucrose concentration (10% w/v). This method is probably capable of exerting high enough tensions to severely influence the disassembly process. Despite this inconsistency, both single-molecule studies propose possible molecular strategies to efficiently remove RAD51 from dsDNA. One option, for example would consists in increasing the rate of ATP hydrolysis only at the filament-end and exploiting the natural hydrolysis rate of RAD51 to catalyse the low-affinity DNA binding state rather than actively wiping off RAD51 by RAD54 translocation through DNA bound RAD51 filaments. A second open question concerns the molecular mechanism of RAD51 disassembly. Specifically, the temporal coordination between the ATP-hydrolysis, the structural change and the release into solution is unknown. Also, the structural reason why individual monomers cannot dissociates from internal regions of the filament but only from disassembling ends is unclear.

2.3 DISCUSSION

As discussed in detail above, over the last two decades, single-molecule approaches have tremendously aided deciphering the individual steps of genetic recombination. DNA manipulation and fluorescence visualization have resulted in a better understanding of recombinase-filament assembly: the rate-limiting step is nucleation on the DNA, involving two to six recombinase monomers. Force-extension measurements have identified dynamics between different conformations of recombinase filaments and how these dynamics depend on ATP-hydrolysis state. Homology search and strand exchange have been studied in separation, resulting in numerous insights in the enigmatic processes. Finally, DNA flow-stretching and optical tweezers studies in combination with fluorescence microscopy have enabled the study of recombinase disassembly at the level of individual nucleoprotein filaments, shedding light on the interplay between disassembly, conformational change and nucleotide hydrolysis.

Future technological and theoretical developments will permit the further elucidation of important questions in HR research. For example, the physical and structural basis of the number of recombinase monomers required for nucleation is still under intense debate. Also direct visualization and characterization of the reaction intermediates in homology search and strand exchange would help to obtain better insight in these processes. Another future challenge lies in studying the role of the many mediators involved in assisting recombinases to perform HR. Such measurements will serve in the verification of existing hypotheses on HR regulation and might shed new insights in the mechanisms of DNA repair.

3 THE SINGLE-MOLECULE APPROACH

COMBINING OPTICAL TRAPPING, FLUORESCENCE MICROSCOPY AND MICRO-FLUIDICS FOR SINGLE MOLECULE STUDIES OF DNA-PROTEIN INTERACTIONS

Complexity and heterogeneity are common denominators of the many molecular events taking place inside the cell. Single-molecule techniques are important tools to quantify the actions of biomolecules. Heterogeneous interactions between multiple proteins, however, are difficult to study with these technologies. One solution is to integrate optical trapping with micro-fluidics and single-molecule fluorescence microscopy. This combination opens the possibility to study heterogeneous/complex protein interactions with unprecedented levels of precision and control. It is particularly powerful for the study of DNA-protein interactions as it allows manipulating the DNA while at the same time, individual proteins binding to it can be visualized. In this work, we aim to illustrate several published and unpublished key results employing the combination of fluorescence microscopy and optical tweezers. Examples are recent studies of the structural properties of DNA and DNA-protein complexes, the molecular mechanisms of nucleoprotein filament assembly on DNA and the motion of DNA-bound proteins. In addition, we present new results demonstrating that single, fluorescently labeled proteins bound to individual, optically trapped DNA molecules can already be tracked with localization accuracy in the sub-10 nm range at tensions above 1 pN. These experiments by us and others demonstrate the enormous potential of this combination of single-molecule techniques for the investigation of complex DNA-protein interactions.

3.1 INTRODUCTION

The complexity of molecular biology

Molecular biology of the cell represents a vast field of research that encompasses thousands of processes. Complexity, randomness, heterogeneity represent the common denominators of the many events taking place in the cell. Thanks to the development of new physical techniques, it has become possible, over the last two decades, to study biomolecules at the single-molecule level in a quantitative fashion. The single-molecule toolbox is composed of a wide assortment of techniques, including optical, magnetic and atomic force microscopy [120, 121], single-molecule fluorescence microscopy, total internal reflection microscopy (TIRFM), Forster-resonance energy transfer (FRET) [140, 115].These techniques permit researchers to raise new exciting questions about the complex behavior of biomolecules, such as: how do translocating enzymes couple their chemical step (NTP hydrolysis) with their mechanical action? What kinetic schemes do proteins adopt to bind to DNA? What is the coupling of their rate-limiting step with the structural properties of the nucleic acid template? What is the actual relevance of off-pathway processes in the enzyme's kinetic scheme?

Applications of the Single-Molecule Toolbox

Single-Molecule Biophysics for studying DNA-protein interactions

The application of single-molecule techniques has yielded important new information on the erratic and often surprising features of many proteins and biopolymers: DNA helicases display pausing and are capable of switching between lead motor subunits during unwinding [66, 157, 156], DNA and RNA polymerases exhibit backtracking, force-induced exonucleolysis activity and a variety of different paused states [183, 148], recombinase proteins bind to DNA in a non-linear [55, 72, 109] and in a torque-dependent [170] manner while their unbinding is a multi-step process that is tightly coupled to the mechanical state of the DNA substrate [174].

Limitations of Optical Tweezers technique

Although widely and successfully employed as scientific tools, both manipulation techniques as well as single-molecule fluorescence detection exhibit drawbacks that limit their capabilities in deciphering single-molecule interactions. For example, in a typical experimental configuration using optical trapping, the enzymatic activity [183], the DNA-protein association [106, 32] or the structural properties of the DNA [178] are detected by monitoring the elastic properties of the DNA tethered between the two optically trapped beads (see Figure 17). In such configuration, outstanding levels of force resolution can be achieved [1, 148, 70]. The only experi-

mental readout, however, is a global feature of the double-stranded DNA template (dsDNA) (i.e. DNA length or stiffness). Therefore, it is not possible to discern between local and global effects of protein-DNA interaction.

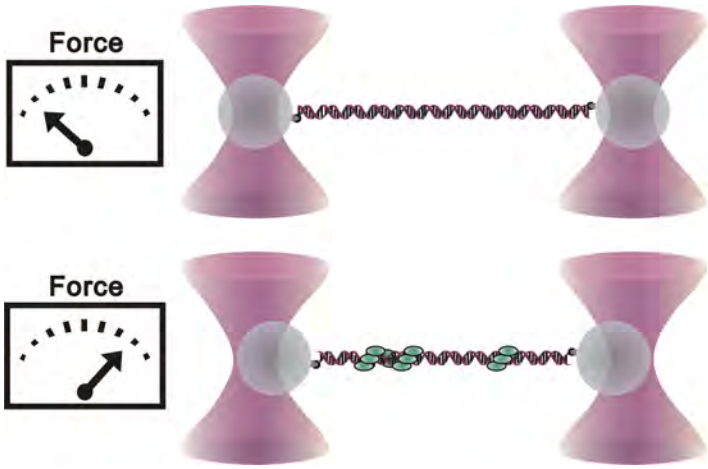

Figure 17.: Dual optical trapping assay for studying DNA-protein interactions. Detecting the tension on a single dsDNA molecule allows studying protein-binding events which cause changes in dsDNA mechanical properties.

As a consequence, potentially crucial details such as the precise location of the interaction, the number of bound proteins and the effect of unspecific protein binding may escape notice.

Limitations of Single-Molecule fluorescence microscopy techniques

Single-molecule fluorescence microscopy, on the other hand, provides access to biochemical insights that are complementary to those obtained using optical manipulation techniques. By using short dsDNA fragments as reaction templates (with a length of less than 100 base pairs), protein-binding kinetics [84], enzymatic translocation velocities [118] and conformational changes of the enzyme can be investigated [40]. Typical approaches include monitoring the light intensity arising from the fluorescently label [101] or the FRET efficiency of a donor-acceptor [118, 188](see Figure 18). When long (up to tens of kilobases) surface-anchored DNA molecules are used, flow-stretching (see Figure 18) or combing are employed to extend the DNA and fix its conformation. In such configuration, protein motion, including diffusion and hopping events, together with the multimerization state of the DNA-bound proteins, are detectable with high accuracy at the single-molecule level [50, 20, 58]. Such methods, how-

ever, result in limited control of DNA tension. Since many enzymatic reactions display a marked dependence on the tension applied on the substrate [183], many relevant features are not experimentally accessible using this approach.

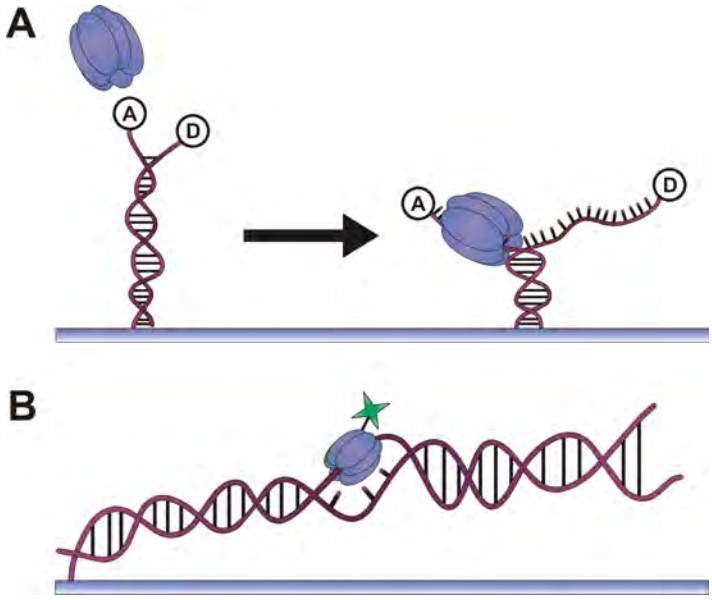

Figure 18.: Single-molecule fluorescence approaches for studying DNA-protein interactions. [A] Reaction progression by a single enzyme can be monitored in real time by detecting changes in FRET efficiency between donor (D) and acceptor (A) labels. [B] Single-molecule fluorescence tracking allows studying enzymatic translocation on a flow-stretched dsDNA molecule bound onto a glass surface.

Advantages of combining Optical Tweezers with Single-Molecule Fluorescence

In addition, general concerns are represented by undesirable and potentially interfering effects due to glass-DNA/protein interactions.
One way to expand the capabilities of single-molecule techniques, in particular in the field of DNA-protein interactions, lies in combining optical trapping and fluorescence microscopy. The key advantages of integrating these two approaches include: (i) measurement of the mechanical state of the DNA-protein complex is complemented with quantification and localization of DNA-bound fluorescent proteins; (ii) mechanical control and visual input of the reaction, allows studying DNA-protein interactions that do not involve global structural changes of the DNA (for example protein sliding, diffusion and hopping); (iii) the ability to detect two independent

data sets (force and fluorescence signal) can serve as an intrinsic experimental control. In general, correlating mechanical with fluorescence information allows studying biological processes at the single molecule level from multiple points of view, providing the opportunity to look at molecular interactions from a more complete perspective.

Detection limit of Optical Tweezers combined with Single-Molecule Fluorescence

The purpose of this review is to discuss recent applications of fluorescence microscopy in combination with optical trapping in the field of DNA-protein interactions. In addition, we present new experimental results demonstrating the accuracy limits of tracking individual fluorescent proteins bound to single DNA molecules held between two optical tweezers. We conclude this manuscript by making several propositions for future technological developments using this combination of manipulation and visualization techniques.

3.2 APPLICATIONS OF COMBINED OPTICAL TRAPPING AND SINGLE–MOLECULE FLUORESCENCE MICROSCOPY TO NUCLEIC ACIDS AND NUCLEIC ACIDS–PROTEIN INTERACTION

In the following section we divide our review according to three distinct types of scientific questions that have been addressed using a combination of optical trapping and fluorescence microscopy: (i) studies of structural and mechanical properties of DNA; (ii) studies of the dynamics of protein binding and unbinding to DNA; (iii) studies of single proteins moving along DNA.

3.2.1 Structural properties of nucleic acids and nucleic acids–protein complexes

DNA is the universal carrier of genetic information. The mechanical and physical properties of DNA play a prominent role in many aspects of life, such as DNA replication, transcription, protein binding and chromosome organization. In addition, protein binding to DNA often results in complexes showing drastically changed elastic and mechanical properties

[32].These processes have been studied extensively using optical trapping and single-molecule fluorescence microscopy.

Single-Molecule studies of DNA dynamics

One of the earliest examples of investigating the mechanical properties of DNA with a combination of DNA manipulation and fluorescence microscopy techniques was during the mid-90s in the lab of Chu. In a series of experiments, several key assumptions of polymer dynamics were tested by direct visualization of optically trapped DNA in a solvent flow field [126, 125, 93, 130]. These studies provided a profound insight in the mechanics and dynamics of DNA at low tension (<10 pN).

Discovery of the DNA overstretching transition

In later studies, optical tweezers were used to apply higher forces to individual dsDNA molecules [155, 158]. Thanks to the sophisticated level of control, it was possible to identify a characteristic force (65 pN) at which DNA enters a highly cooperative transition during which the molecule elongates to 170% of its original length (see Figure 19).

Two models for explaining DNA overstretching: S-DNA vs force-induced melting

The molecular details of this "overstretching transition" have remained unsolved for almost 15 years. Two models persisted: (i) "S-DNA" [35], which envisions the transition as a gradual unwinding of the DNA double helix while the hydrogen bonds and base stacking remain intact; (ii) force-induced melting of DNA [138, 139], which assumes that the base pairing is lost, yielding two single DNA strands. In order to unambiguously resolve the molecular details of the overstretching transition, van Mameren et al. [173] probed the structure of DNA by directly visualizing it using multi-color fluorescence microscopy in combination with optical tweezers. Specific markers were used to probe single- and double-stranded sections of individual DNA molecules during the overstretching transition. Three key observations were made: i) the affinity of the DNA for specific double-stranded ligands (YOYO-1 and POPO intercalators) linearly decreases during the progress of the overstretching transition; ii) the affinity for single-stranded DNA (ssDNA) ligands (mitochondrial single-stranded binding protein and recombination protein A (RPA)) shows the opposite behavior; iii) the separation of the two phases nucleate from the DNA ends or single-stranded nicks (see Figure 19). Taken together, these results demonstrated that, under these conditions, DNA overstretching is caused by force-induced melting, nucleating from free DNA ends.

Proteins induce changes in the elastic properties of DNA

Optical trapping experiments focusing on the mechanical properties of DNA-protein complexes generally measure changes in the DNA elastic properties (such as persistence length, bending stiffness and contour length)

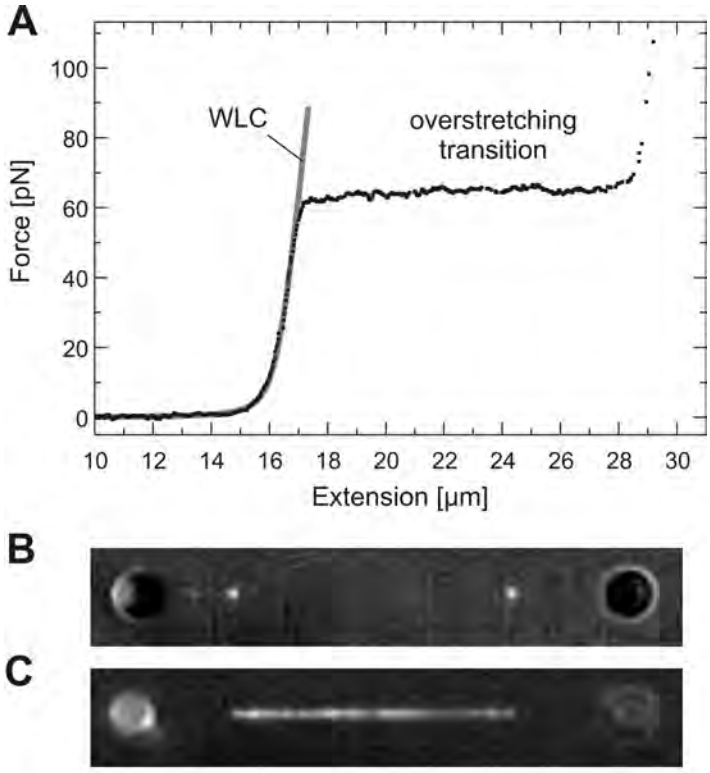

Figure 19.: DNA mechanical properties and DNA overstretching transition. [A] Stretching curve of a 16.4 μm long dsDNA molecule. The force-distance curve follows the Worm-Like Chain model until 65 pN; at higher forces dsDNA enters the overstretching transition. [B-C] Multi-color fluorescence imaging shows spatial segregation of ssDNA (mtSSb specific binding-panel B) and dsDNA (YOYO specific binding- panel C) regions. Figures reprinted from [173]

caused by protein binding. Elastic properties are generally obtained from fitting the Worm-Like Chain model to experimental Force-Extension measurements of the DNA-protein complex [32, 117]. For example, recombinases, such as RecA and RAD51 play a central role in homologous recombination, an essential DNA repair mechanism [160, 16].
These proteins form rigid nucleoprotein filaments in which the DNA structure is drastically distorted [14, 135, 114, 69]. Their binding behavior on double- and single stranded DNA has been characterized by a variety of techniques. Electron microscopy and AFM studies revealed that upon

RecA/RAD51 binding, both forms of DNA undergo mechanical transitions into a longer and stiffer structure [48, 145].

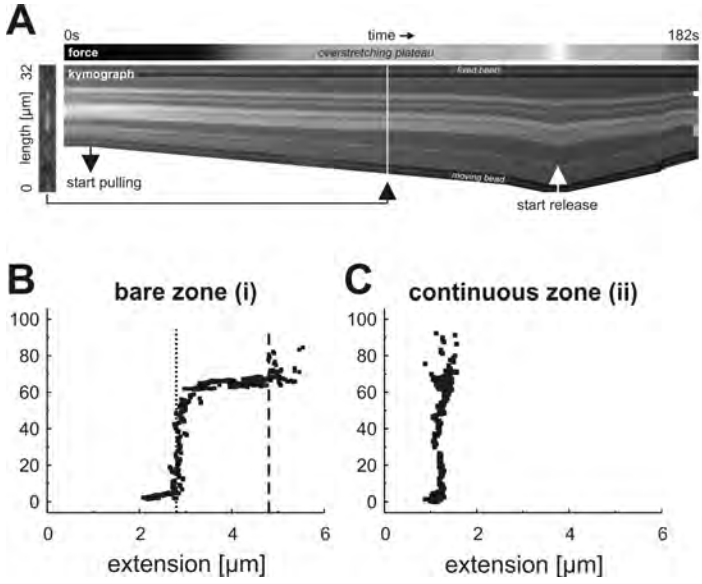

Figure 20.: Heterogeneity in the elastic properties of dsDNA-RAD51 complexes dissected using concurrent fluorescence microscopy and optical tweezers.[A] Series of fluorescent images of a dsDNA molecule partly coated with fluorescent RAD51. Kymograph (right) is generated from successive frames during the extension experiment. [B] Force-extension curve of a bare segment of the dsDNA (i). [C] Force-extension curve of a dsDNA segment coated with RAD51 (ii). Figures reprinted from [175].

Mechanical properties of recombinase nucleoprotein filaments

Optical and magnetic trapping studies have characterized the persistence length and the bending stiffness of individual DNA molecules in association with recombinases under various conditions [69, 150, 13]. In all these studies, however, overall changes in DNA elasticity, of the whole molecules were determined, averaging over regions with non-homogeneous recombinase binding. By combining optical trapping with fluorescence microscopy the non-uniform elasticity of dsDNA only partly covered with RAD51 patches was dissected [175]. By analyzing fluorescence images during stretching experiments force-extension curves of distinct DNA segments could be unraveled, exhibiting very different elastic behavior according to the amount of RAD51 locally bound (see Figure 20). Regions with RAD51 bound hardly extended upon applying forces of up to 90 pN, while

"bare" DNA show the usual elastic behavior, including overstretching (see Figure 20). This experiment highlights that protein-DNA complexes may exhibit heterogeneous elastic properties, depending on the local protein binding over the DNA molecule. In such a case, optical trapping alone would only reveal an averaged elastic behavior of bare and protein-covered DNA, precluding determination of the actual physical properties of the RAD51 nucleoprotein filament.

3.2.2 Dynamic Binding and Unbinding

Many regulatory processes in the cell are controlled by binding and unbinding of proteins to DNA.

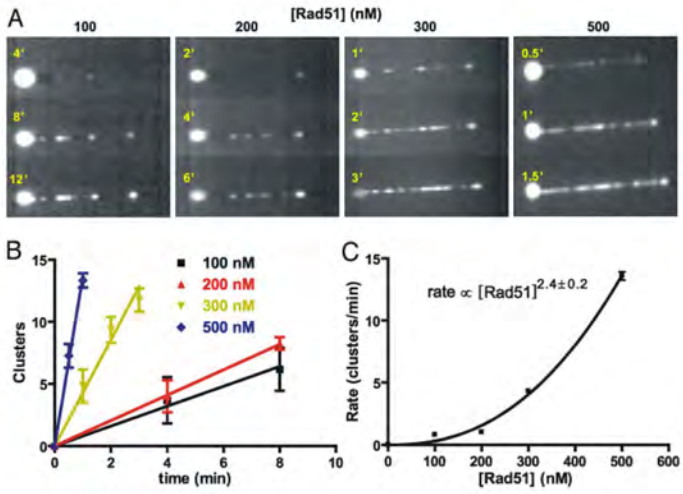

Figure 21.: RAD51 nucleation mechanism on dsDNA studied using a single optical trap and flow-extended DNA combined with fluorescence microscopy. [A] Series of images showing the progression of the RAD51-DNA binding reaction at different time-points using different RAD51 concentration. [B] Time-dependence of RAD51 cluster formation. Figures reprinted from [72].

Assembly and Disassembly of RAD51 on dsDNA

Protein binding often results in local distortion of the DNA conformation, resulting in kinking, looping, wrapping, bridging or compression or extension of the DNA [32]. In many cases, the binding of proteins to DNA is regulated by other proteins or is cooperative. Moreover, extension or shrinkage of protein multimers on the DNA can be directional. Combin-

ing optical trapping and single-molecule fluorescence microscopy allows to quantitatively studying such effects in great detail and in real time. Examples are studies of the assembly and disassembly kinetics of RAD51 on dsDNA. By holding a dsDNA molecule in a single optical trap and extending it in a buffer flow, Hilario et al. [72] studied the binding dynamics of fluorescent RAD51 using fluorescence microscopy, requiring two to three RAD51 monomers (see Figure 21), is followed by filament elongation. RAD51 binding on dsDNA yields hybrid structures with segment of bare dsDNA interrupted by RAD51 nucleoprotein filaments consisting of hundreds of RAD51 monomers. Combining optical trapping and epifluorescence microscopy also revealed the mechanism of RAD51 nucleoprotein filament disassembly from dsDNA (see Figure 22). Van Mameren et al. [174] showed that disassembly of isolated RAD51 patches displays long pauses and sudden bursts of detachment. By accurately quantifying the fluorescence intensity of fluorescently labeled RAD51 it was possible to determine that on average 5 to 10 RAD51 monomers are involved in a single disassembly burst. Pause duration was found to be similar to the average time required to hydrolyze ATP. In addition, the disassembly rate was shown to decrease with increasing tension applied to the dsDNA, leading to stalled disassembly at 50 pN (see Figure 21). Thanks to this multi-faceted approach it was possible to formulate a mechanistic model of RAD51 disassembly. The disassembly process starts with force–independent ATP hydrolysis that occurs all over the filament. RAD51 monomers can only dissociate, with a force-dependent rate, when the terminal monomer has hydrolyzed its ATP, resulting in bursts of disassembly (see Figure 21) that take place up to the next ATP-bound RAD51 monomer. Taken together, these single-molecule studies show that studies of complex biological processes can benefit from approaches that allow simultaneous monitoring of distinct physical parameters, which is possible with the combination of optical trapping and fluorescence microscopy.

3.2.3 Proteins moving on DNA

The key players in genome maintenance processes like replication, transcription and translation are motor proteins that convert chemical energy (NTP hydrolysis) into motion coupled to structural changes of the DNA. Using single-molecule experiments mechanistic features such as DNA-tension-

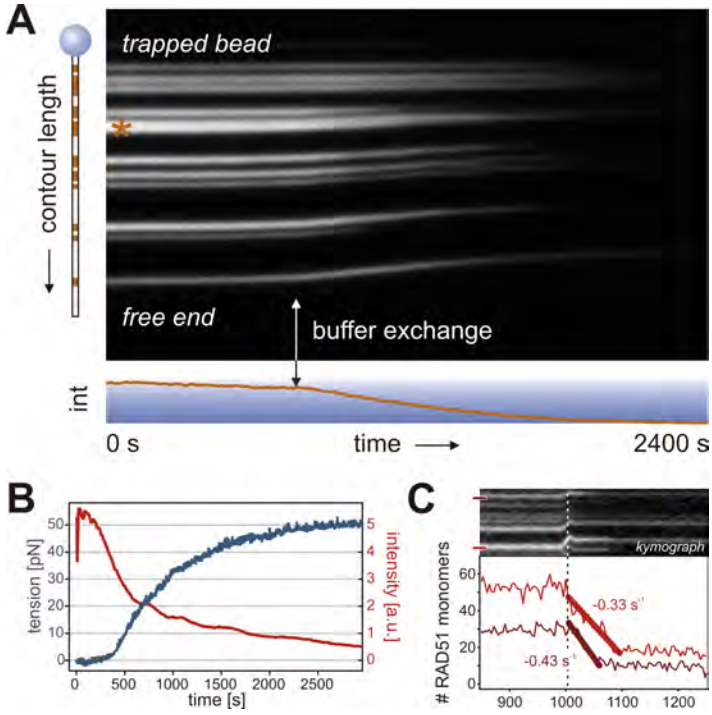

Figure 22.: RAD51 disassembly from DNA at the single-molecule level. [A] Kymograph of a partly RAD51-coated DNA molecule undergoing disassembly upon rapid buffer exchange allowing ATP hydrolysis. [B] RAD51 disassembly can be detected by monitoring simultaneously the fluorescence intensity (thin, decreasing curve) and the tension across the molecule (thick, increasing curve). The anti-correlation of the curves shows the interplay between the mechanical tension and the disassembly process. [C] Monitoring the fluorescence intensity from individual RAD51 patches shows that disassembly occurs in sudden burst and includes long pauses. Figure reprinted from [174].

dependent protein translocation velocities, direction reversal [183], motor switching [156], and 1-dimensional diffusion [20] have been revealed. To study these processes in detail, it is beneficial to not only have full control over the tension and the extension of DNA, but also to monitor in real time the location of the enzyme on the DNA, its conformation and the presence of additional proteins. Combining optical trapping and fluorescence microscopy provides such levels of control.

Flurescence detection of single RNAp enzymes

Harada et al. [67] studied the 1-dimensional diffusion of E. coli RNA polymerase in real time using a custom-fabricated glass cover slip that al-

lowed the integration of TIRF microscopy and optical trapping. Using this approach, efficient background reduction was achieved and site-specific enzyme binding of the polymerase to its promotor sites could be observed.

DNA unwinding by RecBCD at the single-molecule level

In another study, the processive unwinding of dsDNA by the RecBCD helicase was studied, using a flow-extended dsDNA molecule attached to an optically trapped microsphere in combination with epi-fluorescent visualization of helicase activity. In an initial study [15], it was found that an individual RecBCD-complex is capable of continuously unwinding 40000 base-pairs, at an average velocity of 440 bp/s. In a next experiment [157] the effect of the recombination hotspot χ, a specific 8-bp DNA sequence involved in the regulation of homologous recombination, on RecBCD activity was studied. Using a dsDNA template containing theχ-sequence in a known position it was shown that upon χ-recognition, RecBCD enters a paused state of approximately 5s (5.0s $\pm$0.5s), after which the enzyme re-establishes its unwinding activity but at a reduced velocity. RecBCD represents an example of a highly complex molecular machine, whose behavior presents so many different facets (pausing, lead-motor switching, heterogeneity in enzymatic activity and high processivity) that only a versatile approach such as the combination of optical trapping and fluorescence microscopy is capable to account for.

3.3 LOCALIZATION ACCURACY OF INDIVIDUAL FLUORESCENT PROTEINS BOUND TO OPTICALLY TRAPPED DSDNA

In the following section we present new experiments in which we show that single, fluorescently labeled proteins can be readily observed and localized with high precision, only when sufficient control can be exerted on the mechanical state of the dsDNA molecule.

To demonstrate the single-protein resolution of our combined trapping and fluorescence instrument we visualize individual Alexa555-labeled EcoRV restriction enzymes or Cy5-labeled UvrA molecules, stably bound to a dsDNA molecule (λ-DNA, length = 48.5 Kbp) held between two optically trapped microspheres in a stretched configuration, at a tension of 40 pN, using epi-illuminated wide-field fluorescence microscopy. DNA-protein

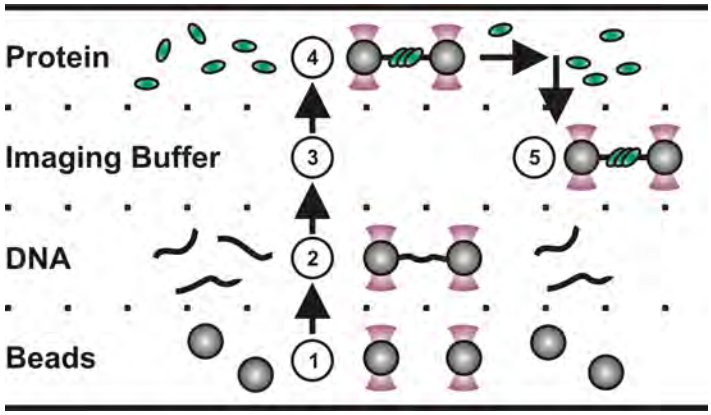

Figure 23.: **Assay for in situ assembly of DNA-protein complexes for single-molecule measurements.** Typical experiments in our multi-channel laminar flow-cell involve 5 steps: 1) Catching two beads in the optical traps. 2) Capturing a DNA molecule between the beads. 3) Measurement of a force-extension curve to ensure that only one DNA molecule tethers the beads. 4) Incubation with fluorescent protein of interest. 5) Visualization of the fluorescentproteins in imaging buffer.

complexes can be readily assembled using our custom laminar-flow system, which allows us to introduce different buffers and components in separate laminar flow channels. After assembly of an EcoRV-DNA construct, single fluorescent spots can be readily discerned (see Figure 24). Integrating the fluorescence intensity over the spot yields an intensity time trace (see Figure 24) showing clear single-step photobleaching, the typical signature of a single fluorophore.

Single protein imaging on a single DNA molecule

Single-molecule sensitivity is achieved thanks to the laminar flow system which permits imaging in the absence of unbound fluorescent protein (imaging buffer). Bleaching times of single fluorophores are on average 30 s, demonstrating that enhanced photobleaching due to the simultaneous presence of fluorescence and trapping laser beams is limited in this configuration [171, 91]. Most likely, this is due to the spatial separation of trapping and fluorescence excitation light in our experimental assay where relatively long DNA molecules are used. Under these conditions, there is no need for temporal separation of excitation and trapping light using modulated laser beams [21, 92, 163]. The capability of resolving single photobleaching steps demonstrated here can be exploited to quantify

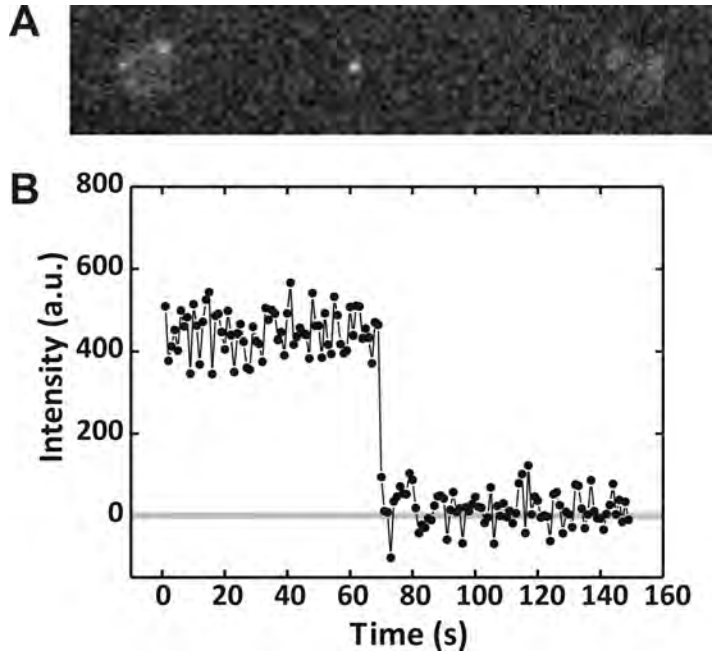

Figure 24.: Combined optical trapping and fluorescence microscopy is capable of detecting single Alexa555 fluorophores. [A] Fluorescence image of a single EcoRV restriction enzyme labeled with Alexa555, bound to a single DNA molecule held between two optically trapped beads and stretched at a constant tension of 40 pN. [B] The time-evolution of fluorescent intensity shows single-step bleaching.

the total number of proteins bound to DNA, as has been employed in the RAD51 disassembly experiments discussed above [174].

3.3.1 The influence of dsDNA flexibility on imaging single, dsDNA-bound fluorescent protein

The role of DNA flexibility in fluorescence detection

Double-stranded DNA is a flexible polymer with a persistence length of 50 nm, therefore large spatial fluctuation are expected to take place due to thermal excitation. By changing the end-to-end distance of a single, optically trapped dsDNA molecule while simultaneously recording fluorescent snapshots of Cy5-labeled UvrA, we investigated the effect of these fluctuations on our ability to resolve single fluorophores.In relaxed dsDNA configurations (L/L_0<0.8 and F<1 pN), the fluorescent spot due to the flu-

orescently labeled proteins is hardly visible and substantially blurred. At higher extensions and tensions the spot sharpens substantially and gains peak intensity (see Figure 25). To quantify this effect, we fit the intensity profile with a spherical 2-dimensional Gaussians function. We report a clear decrease of the fitted Gaussian width (σ) with increasing levels of tension, from 405 nm at very low tension to a limit of 150 nm at tensions above a few pN (see Figure 26). This high-force limit is close to the diffraction limit of our instrument using Cy5 (full-width-at-half-maximum = $0.61\lambda/\mathrm{NA}$ = 340 nm and consequently σ=145 nm). To confirm that this experimental outcome is consistent with the physical properties of dsDNA, we decompose the dsDNA motion in its independent modes and use the equi-partition theorem to estimate the fluctuations of the molecule using the following formula:

$$\sqrt{\langle u^2(x)\rangle} = \sqrt{\sum_{n>1} \frac{2k_BT}{L\left(K\left(\frac{n\pi}{L}\right)^4 + F\left(\frac{n\pi}{L}\right)^2\right)} \sin^2\left(\frac{n\pi}{L}x\right)} \qquad (1)$$

Where x represents the position along the dsDNA molecule, L the length of the dsDNA (L=16400 nm) and K the dsDNA bending stiffness ($K = k_BT \times L_p \sim 4$ pn nm $\times$ 50 nm = 200 pN nm^2). In order to compare with the experimentally observed fluorescent spot widths, these theoretically determined fluctuations need to be convolved with the optical resolution of our microscope, yielding the red curve (see Figure 26). The quantitative agreement between model and experimental data is striking. Note that our model is based on first principles and does not contain any fitting parameters.

These results show that the thermal fluctuations of a dsDNA molecule can be effectively suppressed by exerting a mild force of 1 pN on the dsDNA, yielding imaging conditions that are only limited by optical diffraction. The binding of most DNA-binding proteins is hardly affected by such small tension on the DNA, making high-resolution imaging of individual protein bound to single, optically-trapped dsDNA molecules, generally feasible.

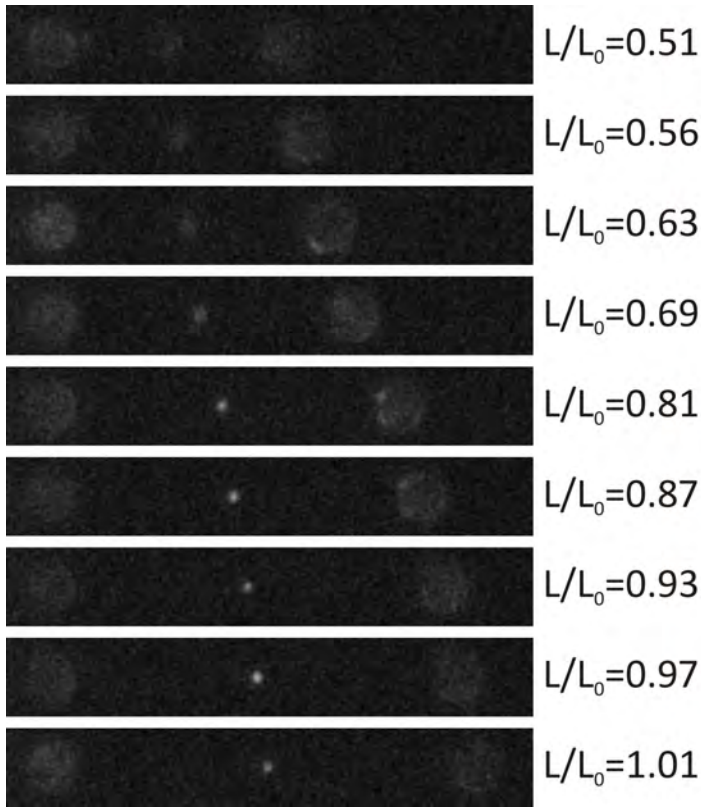

Figure 25.: **Image blurring due to dsDNA mechanical fluctuations at different end-to-end distance.** A single dsDNA molecule (λ-DNA, length 16.4 μm) with a single fluorescent protein bound (UvrA with Cy5 label) is held at different extensions while fluorescence snapshots are taken (exposure time 1s).

3.3.2 Sub-10 nanometer localization accuracy of single fluorescently-labeled proteins on optically trapped dsDNA

Localization accuracy vs optical resolution

Diffraction effects limit the resolution of an optical microscope to the Abbe limit (resolution = $0.61\lambda/\mathrm{NA}$, corresponding to about 340 nm using 700 nm and high-numerical aperture objectives). Resolution, however, is not what ultimately limits the accuracy with which a single fluorophore can be localized. By using Gaussian fitting, in fact, localization accuracies in the nanometer range can be achieved, depending on signal-to-noise ratio [164, 186]. Here we investigate whether we can apply similar localization approaches to single fluorophores bound to suspended dsDNA molecules

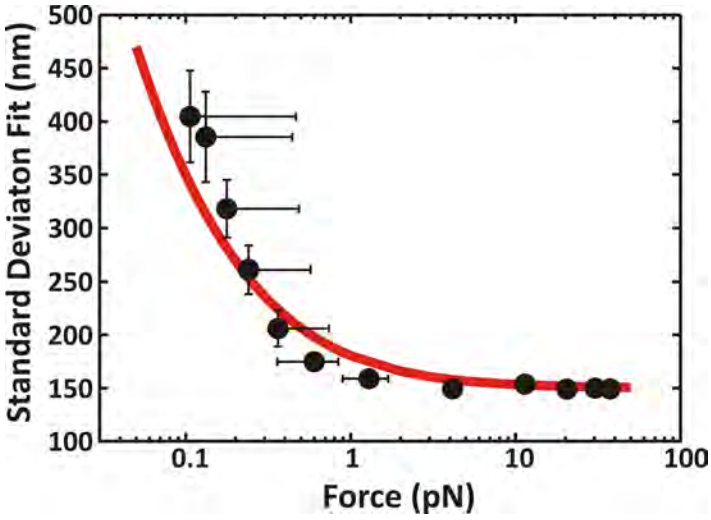

Figure 26.: **The width of the detected fluorescent spot depends on the mechanical state of the dsDNA molecule**. The values of the standard deviation obtained from the two-dimensional Gaussian fitting (black circles) decrease with the applied tension. The asymmetry of the error bars is a consequence of the logarithmic scale used (for clarity, the error bars have not been drawn on the low-force side for the low force data points). This behavior is well described taking into consideration the brownian fluctuation of the DNA molecule and the finite Point Spread Function of our microscope (continuous curve).

and what localization accuracy can be achieved in this configuration. Using the same data and Gaussian fits as presented above we quantify the localization accuracy by measuring the standard deviation of the obtained position-trajectories. As expected, we find a strong dependency of localization accuracy on dsDNA tension (see Figure 27) The accuracy ranges from 200 nm in the very low tension regime (F<0.1 pN), to sub-10 nm range at tensions above 1 pN.

A physical explanation for the dependence of location accuracy on applied tension can be found in the force-dependent blurring of the fluorescent spots due to fluctuations of the dsDNA. As demonstrated in Figure 26, dsDNA fluctuations are significant, on the scale of the point-spread function at tensions below 1 pN, resulting in substantial broadening of fluorescent spots and decreased localization accuracy. At forces above 1 pN the accuracy is not limited by dsDNA fluctuations, which apparently average out on the 1 s timescale of our experiments, but by the signal-to-

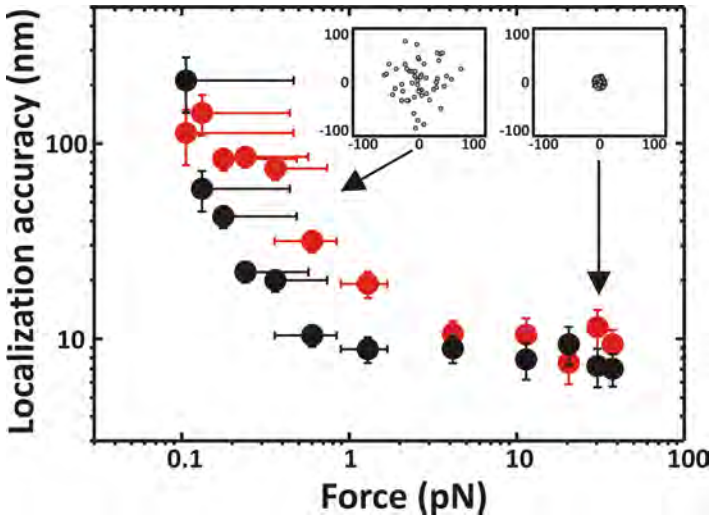

Figure 27.: Single-particle tracking accuracy is modulated by DNA tension. Localization accuracy in the direction longitudinal (black dots) and transversal (grey dots) to the DNA reaches the sub-10 nm level at forces above 1 pN. In the inset, actual fitting results are displayed.

noise ratio. Even better localization accuracies could be obtained if longer integration times or higher excitation intensities (at the expense of the fluorophore lifetime) are applied (data not shown). Once accurate localization of single-fluorophores is coupled to the knowledge of the beads positions it is possible to obtain precise information of the absolute location of protein binding.

Sequence-specific binding of EcoRV detected using Optical Tweezers combined with Fluorescence Microscopy

We probed our capability in determining the position of protein binding sites of using fluorescently labeled EcoRV and λ-DNA. We deduced the position and the orientation of the λ-DNA by tracking the bead location and size and by using their extremities to infer the actual λ-DNA attachment points. Figure 28 represents an example in which we compare the location of known EcoRV binding sites (dotted lines) with the fluorescence image obtained from three individual EcoRV enzymes bound to the DNA (see inset). The Gaussian fits clearly coincide with known binding sites. From our measurement the average deviation between fit and sequence location is 14 ± 7 nm, demonstrating that sequence-specific interactions can be detected with high precision. We have demonstrated that combining optical trapping with fluorescence microscopy allows simultaneous monitoring and controlling the mechanical state of a single dsDNA molecule

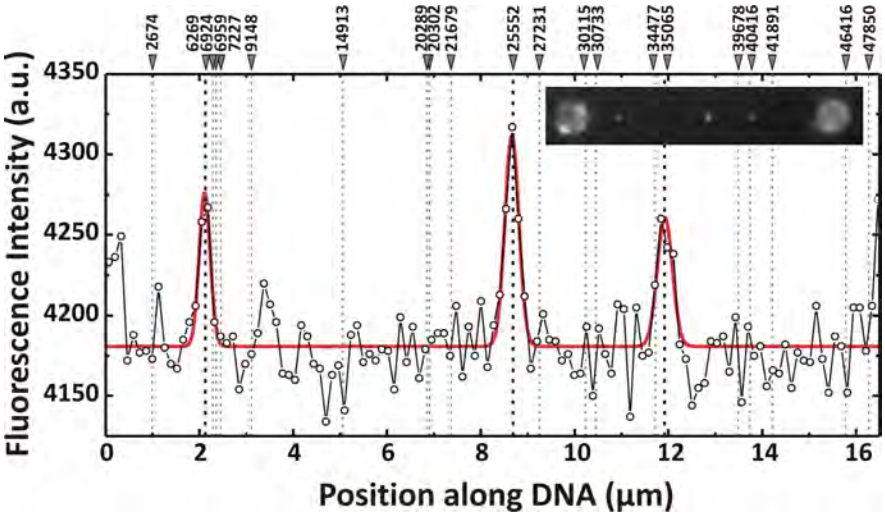

Figure 28.: **Detection of specific binding of restriction enzyme EcoRV.** Gaussian fitting of the fluorescent spots corresponds to known binding sites of EcoRV along λ-DNA with a precision of 14 ± 7 nm. EcoRV binding sites are represented with dotted lines. A series of fluorescent images is stacked and displayed in the inset.

at the sub-pN level, while the position of individual organic-dye-labeled proteins, using our illumination conditions, can be determined with an accuracy of 8 nm using integration times of 1 s. The high flexibility of dsDNA requires that a tension of more than 1 pN is applied in order to suppress dsDNA conformational fluctuations and allow localization accuracies below 10 nm. This accuracy is highly relevant to many biological problems in the realm of DNA-protein binding, since it is approximately equivalent to the typical binding size of proteins.

3.4 DISCUSSION

To address complex DNA-protein interactions displaying a high level of complexity in a well-controlled manner, it is important to develop innovative techniques able to probe the reaction in a multi-faceted, versatile fashion. One of such approaches is combining DNA manipulation and single-protein visualization. With this combination, information on DNA-protein interactions can be obtained far beyond the capabilities of the indi-

vidual techniques.

Different routes for integrating DNA manipulation with fluorescence visualization

In the past years, several different routes have been successful in integrating optical trapping and single-molecule fluorescence microscopy. Harada et. al [67], in their pioneering work, positioned the optically manipulated dsDNA in proximity of a glass-etched pedestal, therefore obtaining efficient fluorescence excitation and background rejection via Total Internal Reflection (TIR). While possible, this approach suffers from the requirement of a custom-fabricated glass flow-cell, applicability only to long dsDNA-tethers, and the obligation of low-protein concentration for achieving single-molecule sensitivity.

A second approach is to attach an optically trapped bead on a surface-anchored dsDNA fragment while applying TIR fluorescence illumination [21, 92, 163]. While it has been shown that some organic dyes (TAMRA) can be used in this configuration, the same cannot be said for commonly used chromophores (Cy3, Alexa555) due to the enhanced photobleaching rate caused by the proximity of the high-power trapping light [171, 91, 92]. To circumvent this problem, the trapping and the fluorescence excitation beams are alternately modulated at high frequency (50 kHz) to avoid their simultaneous presence in the sample [21, 163]. Using this strategy, fluorophore lifetimes of tens of seconds were obtained. This approach, although generalizable to different situations, presents some disadvantages: i) it is technically demanding ii) it is impossible to directly localize the fluorescent probe. In fact, without a priori knowledge of its position, the only readout is the actual intensity count. A second possibility to avoid the enhanced photo-bleaching consists in using quantum-dot labeling [17, 26]. Quantum dots exhibit superior photo physical properties in terms of number of emitted photons and resistance to photo-damage. Quantum dots, however, are rather large and might influence the enzymatic process under study [133].

Our results show that by using long DNA tethers (16.4 μm) and common organic-dye fluorophores (Alexa555 and Cy5) single-molecule fluorescence sensitivity with long fluorophore lifetimes (approximately 60 frames at 1 sec/frame) can be achieved while retaining the capability to perform high-resolution force measurements. The concurrent use of a laminar flow-cell system and of a computer-controlled microscope stage, allows an efficient use of this approach for protein-DNA interaction studies, as the interaction time can be controlled with a resolution in the sub-second domain while

the actual fluorescence imaging takes place in a background-free environment.

While this work focused on the organic-dye labeled proteins, we have also routinely used eGFP as a fluorescent probe and achieved single-molecule sensitivity with similar localization accuracies as presented here for organic dyes. While eGFP-labeling of proteins is more straightforward and better controlled, a severe limitation in particular in complex in vitro experiments, is its inferior brightness and mediocre photostabilityc [147].

Visualizing single proteins along a single dsDNA molecule can nevertheless be achieved using different single-molecule assays. Single-optical-trap and surface-based dsDNA flow-stretching, for example, have repeatedly been applied to directly image individual DNA-bound proteins. While it has been shown that fluorescent centroid localization is possible with a precision of 1 nm [186], this level of accuracy has never been obtained for protein movement on dsDNA. This limitation can be explained by the large mechanical fluctuations of the dsDNA due to Brownian motion. The presence of these fluctuations affects the spatial resolution, as the localization accuracy depends on the width of the fluorescent spot [164].

The importance of Optical Tweezers for achieving high localization accuracy

Our approach exploits optical manipulation to confine the dsDNA motion to achieve ideal imaging conditions (diffraction-limited fluorescence spots). According to our observations, a mild longitudinal force (F=1 pN) is sufficient to achieve high resolution and high localization accuracy (8 nm) in single-protein tracking, therefore putting forward combined optical trapping and fluorescence microscopy as a powerful solution for visualizing single proteins along a single dsDNA molecule.

Our results represent a first step towards the integration of more sophisticated fluorescence approaches within the optical tweezers platform.

Among the vast and mostly unexplored alternatives, combining multicolor fluorescence microscopy with optical trapping represents a straightforward improvement that could greatly advance our understanding of protein-protein interactions, providing the means to address biological problems of high complexity. In fact, by using spectrally separated fluorescent labels it will be possible to directly visualize individual components of multi-proteins processes and understand the mechanism of their concerted action. Another interesting evolution is represented by the incorporation of Forster Resonance Energy Transfer (FRET) spectroscopy. This approach will allow monitoring the relative movement of individual pro-

tein domains and studying the coupling between the mechanical, chemical and structural rearrangements during the enzymatic cycle. New scenarios for DNA-protein binding studies could be opened once optical trapping and confocal fluorescence microscopy are integrated into a single instrument. The confocal approach efficiently rejects out-of-focus fluorescence and allows excitation only within a very limited volume. In this way the dynamic proteins-DNA interactions can be followed in real time even at relatively high protein concentration.

Future application of super-resolution fluorescence to Optical Tweezers

Ultimately, a goal in the continuous road of technological advancement is to integrate super-resolution microscopy (STED, PALM and STORM for example) with optical trapping. This technology will allow observing the local structure of DNA-protein complexes with unprecedented detail. The capability of monitoring the tension along a single dsDNA molecule at the pN level together with ability to detect the presence, the number, the conformation and the position of individual fluorescent proteins with ultra-high accuracy will allow to perform innovative and exciting single-molecule experiments and decipher the details of DNA-protein interaction in a quantitative and precise fashion.

.

4 GENERATING SSDNA FOR OPTICAL TWEEZERS

A TOOLBOX FOR GENERATING SINGLE-STRANDED DNA IN OPTICAL TWEEZERS EXPERIMENTS

Essential genomic transactions such as DNA-damage repair and DNA replication take place on single-stranded DNA (ssDNA) or require specific single-stranded/double-stranded DNA (ssDNA/dsDNA) junctions (SDSJ). A significant challenge in single-molecule studies of DNA-protein interactions using optical trapping is the design and generation of appropriate DNA templates. In contrast to double-stranded DNA (dsDNA), only a limited toolbox is available for the generation of ssDNA constructs for optical tweezers experiments. Here, we present several kinds of DNA templates suitable for single-molecule experiments requiring segments of ssDNA of several kilobases in length. These different biotinylated dsDNA templates can be tethered between optically trapped microspheres and can, by the subsequent use of force-induced DNA melting, be converted into partial or complete ssDNA molecules. We systematically investigated the time scale and efficiency of force-induced melting at different ionic strengths for DNA molecules of different sequences and lengths. Furthermore, we quantified the impact of microspheres of different sizes on the lifetime of ssDNA tethers in optical tweezers experiments. Together, these experiments provide deeper insights into the variables that impact the production of ssDNA for single molecules studies and represent a starting point for further optimization of DNA templates that permit the investigation of protein binding and kinetics on ssDNA.

4.1 INTRODUCTION

Optical trapping is a powerful single-molecule technique that uses the gradient forces created by highly focused laser beams to trap and manipulate micron-sized particles [7]. In the last two decades, numerous highly sophisticated optical-tweezers experiments have been carried out to study fundamental cellular processes, such as DNA replication [183], transcription [70], recombination [52] and compaction [32].

Applications of single-molecule techniques

These studies have revealed unexpected features of proteins interacting with DNA that were previously obscured in ensemble-averaged bulk methods. More recently, the capabilities of optical trapping have been extended by incorporating fluorescence microscopy techniques, allowing visualization and localization of individual proteins bound to a DNA molecule with nanometer accuracy, while holding the DNA at a defined tension with sub-piconewton resolution [36, 25]. The use of dual-trap optical tweezers for DNA manipulation in combination with fluorescence microscopy imposes strict requirements on the design of DNA templates: (i) the DNA molecules need to be specifically labeled (with for example biotin or digoxigenin) at their extremities in order to be attached to functionalized microspheres; (ii) the length of the DNA molecules should be 1 μm or longer to avoid polarization cross-talk between the traps [100], enhanced photobleaching of fluorophores [171] and oxidative attack of the DNA [39, 91]. These prerequisites have rendered the use of ssDNA in optical tweezers very difficult because of two main reasons: (i) the biochemical challenges to obtain long, end-labeled ssDNA molecules and (ii) the difficulty to tether ssDNA molecules from solution between two trapped microspheres. As a result, most of the single-molecule experiments performed on ssDNA-protein interactions made use of short oligonucleotides in combination with FRET spectroscopy [140].

Cellular processes involving ssDNA

Yet, in the living cell, long stretches (1000 nucleotides) of ssDNA coated with ssDNA specific proteins are present during many fundamental processes. For example, during DNA replication, the ssDNA used as a template by DNA polymerases, is often found in complex with single-stranded binding proteins [180]. In homologous recombination, recombinase proteins of the RecA/RAD51 family assemble on long segments of ssDNA and catalyse strand exchange between homologous DNA molecules [142]. Hence, "there is a need to develop methods that can image multiple pro-

teins on a long ssDNA as has been demonstrated for proteins on dsDNA" [63].

Labeling DNA molecules for optical tweezers experiments

Over the last two decades, end-labeling of (long) dsDNA molecules with biotins has become the standard for single-molecule experiments, using either biotinylated oligonucleotides [154, 177, 88] or the incorporation of biotinylated nucleotides with a DNA polymerase [155]. In previous studies, it has been shown that such dsDNA constructs can be used for the generation of ssDNA templates for single-molecule experiments. To obtain the ssDNA, often a combination of force-induced melting with either formaldehyde [155] or sodium hydroxide denaturation [169] was used. Force-induced melting is described as the transition from dsDNA to ssDNA when dsDNA is kept under tension of more than 65 pN [173, 60]. When the DNA molecule is labeled on both ends of the same strand, force-induced melting can result in the release of the complementary strand, yielding ssDNA [69, 99, 155]. Alternatively, ssDNA was generated by digesting one of the strands with exonucleases [78]. However, clearing the fluidic devices of these chemicals or enzymes before experiments can be tedious. Incomplete removal of chemicals could lead to a change in pH, ionic conditions and different electrostatic properties of the glass surface, while contamination with enzymes could interfere with experiments. A systematic investigation of the parameters that impact force-induced melting as a method to generate long ssDNA templates is, however, lacking.

Generating and preserving ssDNA in optical tweezerse experiments

Maintaining ssDNA in optical tweezers for a prolonged time is more challenging than dsDNA, since the appearance of a single nick results in breaking of the molecule and the end of the experiment. Chemla et. al. have found that reactive oxygen species (ROS) created at the polystyrene surface of the microspheres due to presence of the intense trapping laser can lead to the loss of the DNA tether [91]. It was found that the mechanism of tether-loss involves the modification of the biotin-streptavidin and digoxigenin-antidigoxigenin bond linking the DNA to the trapped polystyrene bead. Use of larger microspheres moves the tethering point of DNA away from the area of ROS production and thereby reducing this issue. The impact of the presence of ROS on the actual integrity of tethered ssDNA has not been explored yet.

In this study, we describe protocols that combine, improve and generalize known methods for the labeling, melting and preservation of DNA in optical tweezers to generate reliable, long segments of ssDNA for studying

protein-ssDNA interactions. In particular, we adapted existing methods to straightforwardly label both ends of the same strand of kilobase-long dsDNA constructs of different lengths, with the option to also label one end of the complementary strand. We show that force-induced melting under medium to low ionic conditions can be reliably used to generate ssDNA without the need of adding aggressive chemicals or enzymes. Moreover, we show that force-induced melting makes it possible to generate ssDNA/dsDNA junctions by using specific nicking enzymes. Next, we quantified methods that preserve the lifetime of ssDNA tethers kept between optically trapped microspheres. We show that the lifetime of ssDNA tethers is extended by almost an order of magnitude when we double the size of the microspheres from 2 micron to 4 micron. The easy production of ssDNA together with the increase of the lifetime of ssDNA in a tethered configuration from a few minutes to nearly half an hour opens many possibilities of addressing exciting scientific questions on processes occurring on ssDNA.

4.2 MATERIALS & METHODS

In all the following protocols, ligation is performed using T4 DNA ligase in 1x T4 DNA ligase buffer (Fermentas). Biotinylated (biotin-14-dATP and biotin-14-dCTP, Invitrogen) and non-modified nucleotides (Fermentas) are incorporated using Klenow exo- DNA polymerase (Fermentas). All modified and non-modified oligonucleotides are from Biolegio. Unless stated otherwise, restriction enzymes are from Fermentas.

4.2.1 Labeling procedure for the generation of the long ssDNA construct

The labeling of lambda DNA (see Figure 30.A) is adapted from earlier techniques to label with oligonucleotides [88]. Lambda DNA (Roche) is a linear molecule of 48,502 bp in length with two single-stranded 12-nt overhangs on both 5′-ends. To label the 3′- and 5′-end of the same strand, we used three oligonucleotides [88]. First, the 5′-end of Lambda DNA and oligonucleotide 1 and 2 were phosphorylated for 30 min at 37°C in a reaction containing 14 nM Lambda DNA or 10 μM of the oligonucleotide and 0.25 U/μl of T4 Polynucleotide Kinase in 1x T4 Ligase buffer (Fermentas).

Next, oligonucleotides 1 and 3 were annealed to the overhangs of Lambda DNA in a 10:1 oligonucleotide: DNA ratio (total volume 500 μl) by heating the reaction to 65°C for 5 minutes, after which the heat block was switched off. When the heat block was cooled down to room temperature, the ligation reaction was initiated by adding T4 DNA ligase (0.02 U/μl) and carried out for two hours. Next, oligonucleotide 2 was annealed in a 100:1 ratio to the Lambda DNA construct by incubation at 45°C for 30 minutes. As before, the reaction was slowly cooled down to room temperature by switching of the heat block. Subsequently, the oligonucleotide was ligated to the DNA at room temperature. Finally, the DNA was purified by ethanol precipitation. Ethanol precipitation was achieved by adding 1/10 volume of NaOAc (3 M, pH 5.6) and subsequently 2.5 volumes of cold 96% ethanol (-20°C). The sample was mixed by inverting 2-3 times and incubated on ice for 15 minutes. Next, the reaction was centrifuged at 12,000 g for 30 minutes at 4°C, resulting in the formation of a visible pellet of DNA. We carefully discard the supernatant without disrupting the pellet. The reaction was washed with 0.7 mL cold 70% ethanol and centrifuged for 10 minutes (12,000 g) at 4°C. Finally, the pellet was dried at room temperature and subsequently resuspended in 50 μL of 10 mM Tris-HCl pH 7.5.

4.2.2 Labeling procedure for the generation of the short ssDNA construct

Two vectors were used for the biotinylation of short dsDNA on the same strand (3'-5' labeling): pTR19-ASDS (10,729 bp, kind gift of Dr. Y.J.M. Bollen, VU University Amsterdam) and pKYB1 (8,393 bp, New England Biolabs). In both cases, the biotinylation strategy (see Figure 30.B) followed a similar approach: on one end, biotinylated nucleotides were incorporated to a single-stranded overhang; on the other end of the same strand, a biotinylated oligonucleotide was ligated as depicted in figure 2B. To this end, the circular plasmids were first digested with EcoRI and ApaI in the case of pTR19-ASDS and EcoRI and KpnI for pKYB1 (Fermentas, FastDigest restriction enzymes). The complementary nucleotides, biotin-14-dATP and dTTP (Invitrogen), were incorporated into these overhangs. Digestion and labeling were conducted simultaneously (45 minutes at 37°C) in a reaction containing: plasmid DNA (pTR19-ASDS or pKYB1) (20 nM, in total 3 μg), biotin-14-dATP (66 μM), dTTP (66 μM), EcoRI (0.05 FDU/μl), ApaI or KpnI (0.05 FDU/μl), 0.2 units/μl Klenow exo- DNA polymerase and

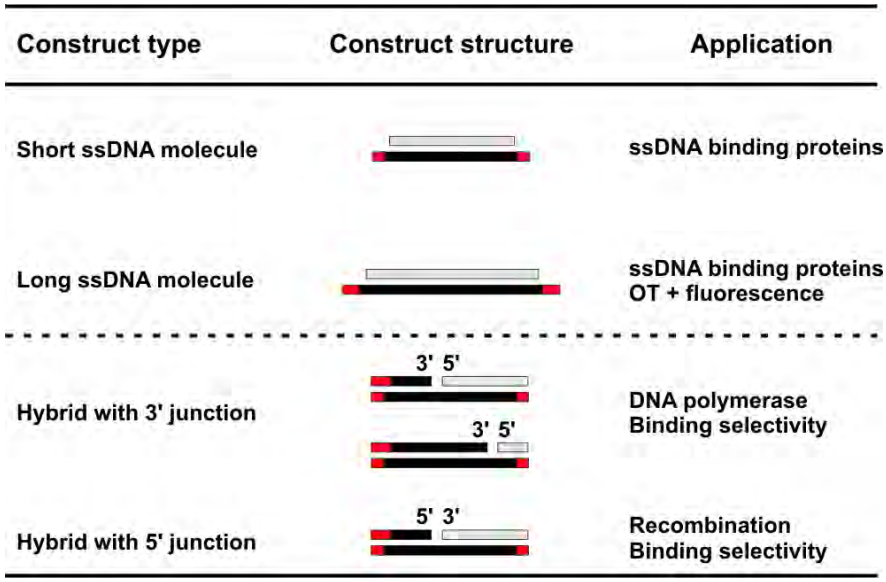

Figure 29.: **Schematic representation of the ssDNA constructs developed and used in this study.** Red: biotinylated extremities required for the attachment to the microspheres. Black: central section available for the enzymatic reaction. Light grey: untethered section that is displaced upon force-induced DNA melting.

1x FastDigest buffer. The reaction was terminated by heat inactivation (10 minutes at 80°C). DNA was purified using ethanol precipitation, as described before. For pTR19-ASDS, the restriction digestion resulted in a 9,896 bp and an 824 bp fragment. For pKYB1, the digestion yielded an 8,356 bp and a 37 bp fragment. The 9,900 bp (pTR19-ASDS) fragment containing a 3'-overhang was separated and purified on an agarose gel using the QIAquick gel extraction kit (Qiagen). For the pKYB1 construct, the 8,356 bp fragment was purified with the QIAquick PCR Purification Kit (Qiagen). Next, biotinylated oligonucleotide 4 for pTR19-ASDS or biotinylated oligonucleotide 5 for pKYB1, was annealed to this construct (50:1 ratio oligonucleotide: DNA) by heating the reaction mixture to 65°C for 5 minutes, followed by slow cooling down to room temperature. Subsequently, the ligation reaction was initiated by adding T4 DNA ligase (0.2 U/μl). After 2 hours, the reaction was terminated by heat inactivation (10 min at 65°) and the DNA was purified with the QIAquick PCR Purification Kit. The resulting DNA constructs are 9,900 bp or 8,360 bp long with two

biotinylated dATPs at the 3'-end, and a 25 nucleotides overhang containing 4 biotinylated dTTPs at the 5'-end of the same strand.

4.2.3 Labeling procedure for the generation of the ssDNA-dsDNA hybrid

Double stranded DNA plasmid pKYBI (8,393 bp, New England Biolabs) was digested with BaeI to create two non-complementary 3'-overhangs in a reaction containing: plasmid DNA (10 nM, 3 μg), 1x NEB buffer 4, 0.1 U/μl BaeI (New England Biolabs). The reaction was terminated by heat inactivation (20 min at 65°C) and the restricted DNA was purified using QIAquick PCR Purification kit. In the next step, two oligonucleotides were annealed to the 3'-overhangs. Depending on the desired polarity of the junction, one or both oligonucleotides were labeled with biotins on the 5'-end (see Figure 30.C). The ligation reaction was carried out at room temperature for 2 hours in a reaction containing BaeI-restricted pKYBI, oligonucleotide 1 and 2 (50:1 ratio) and 60 Weiss units of T4 DNA ligase. The reaction was terminated by heat inactivation (10 min at 65°C) and purified using the QIAquick PCR Purification kit. In the next step, the 3'-ends are filled in using Klenow exo-. For the final construct with the 5'-overhang, only one of the overhangs was filled in with biotinylated nucleotides (see Figure 30.C-left). For the final construct with the 3'-overhang, both overhangs were filled in with biotinylated nucleotides (see Figure 30.C-right). Finally the DNA was nicked either in the bottom strand (using Nb.BbvCI, New England Biolabs) or the top strand (using Nt.BbvCI, New England Biolabs). A typical reaction to create the construct containing a 6.6 kb ssDNA 5'-overhang is performed in one single step containing: 0.5 pmol of DNA (pKYBI with annealed biotinylated oligonucleotides 6 and 7), 1x Tango Buffer (Fermentas), 66 μM biotin-14-dCTP, 80 μM dATP, 0.2 units/μl Klenow exo- DNA polymerase and 0.4 units/μl Nb.BbvCI (New England Biolabs). The reaction was heat inactivated at 80°C for 20 minutes and finally purified using QIAquick PCR Purification kit.

4.2.4 Optical Tweezers setup

A detailed description of the optical tweezers instrument can be found elsewhere [59, 25]. In short, a Nd:YAG laser (3 W continuous wave, 1064 nm, Ventus 1064, Laser Quantum) was used to generate two optical traps.

Oligo	Sequence
1 - Long ssDNA	5′- ggg cgg cga cct gga caa - 3′
2 - Long ssDNA	5′- agg tcg ccg ccc ttt ttt tTt TtT - 3′
3 - Long ssDNA	5′- TtT tTt ttt ttt aga gta ctg tac gat cta gca tca atc ttg tcc - 3′
4 - Short ssDNA - pTR19-ASDS	5′- cTc TcT cTc tct tct ctc ttc tct tgg cc - 3′
5 - Short ssDNA - pKYB1	5′- cTc TcT cTct ctt ctc tct tct ctt gtac - 3′
6 - ssDNA/dsDNA	5′- gTg TTg gtt ttg ttg tgg gat gg - 3′
7 - ssDNA/dsDNA	5′-TcT cTc cttc ctc ctt tca agc a - 3′

The laser beam was split into two orthogonally polarized beams using a polarizing beam splitter cube (10BC16PC.9, Newport). The two beams were expanded with a 1:2.67 telescope system. One beam was steered by laterally displacing a telescope lens. Two traps were produced with a high-numerical aperture water-immersion objective (Plan Apo 60X, numerical aperture = 1.20, Nikon). Two microspheres (1.87 μm, streptavidin-coated, Spherotech) were held in these traps, and their microscope image was digitized using a frame-grabber board (IMAQ PCI-1409, National Instruments). We determined the distance between the two microspheres using a LabVIEW program (National Instruments), applying template-directed pattern matching. The displacement of the trapped microsphere with respect to the trap centre was detected using a position-sensitive detector (DL100-7PCBA Pacific Silicon Sensor Inc.), low-pass filtered with a cut-off frequency of 145 Hz and digitized using a 16 bit data-acquisition board (PCI 6229, National Instruments). Force and distance were simultaneously recorded by a Labview program, operating at a sampling rate of 25 Hz.

4.3 RESULTS

DNA constructs suitable for optical tweezers experiments can be divided in two classes: constructs that are completely ssDNA and ssDNA/dsDNA hybrids. In the first class, dsDNA is labeled with biotins on only of the strands such that it can be converted entirely into ssDNA tethered between the trapped microspheres. Different types of ssDNA constructs are needed for different experimental configurations or biological processes under investigation. To study ssDNA–protein interactions resulting in measurable

changes in the mechanical properties of the DNA, the use of short and thus stiffer ssDNA molecules (contour lengths shorter than about 4 μm) is advantageous to increase sensitivity [116].

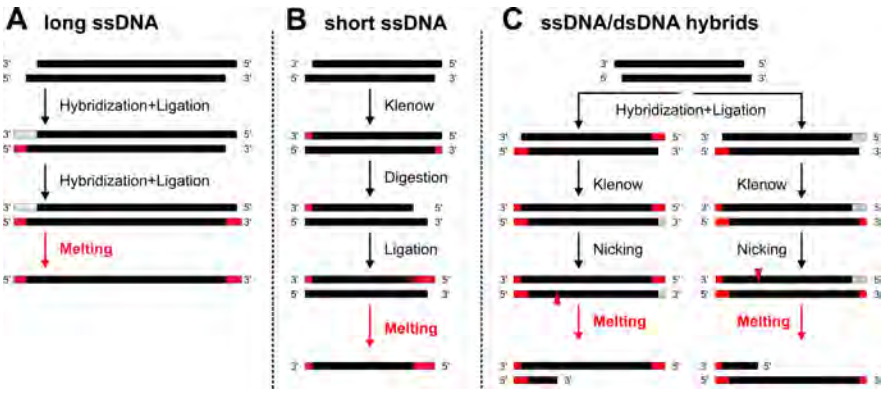

Figure 30.: Strategies for DNA labeling to generate ssDNA constructs using force-induced DNA melting. [A] Labeling protocol for the long ssDNA molecule. Oligonucleotide 1 (unlabeled-grey) and oligonucleotide 2 (4 biotins-red) are hybridized and ligated to create a 5′ labeled end. Oligonucleotide 3 (4 biotins-red) is hybridized and ligated to produce the 3′-labeled end. Force-induced DNA melting allows the production of the long ssDNA molecule template. [B] Protocol for the short ssDNA molecule: a linearized plasmid is filled in with Klenow exo- polymerase, digested with a restriction enzyme and labeled with a biotinylated oligonucleotide. [C] The single-stranded and double-stranded DNA junction (SDSJ) construct is made by annealing two oligonucleotides to a linearized plasmid. The new overhangs are filled in with Klenow exo- polymerase and finally the DNA molecule is nicked using a specific nicking enzyme.

On the other hand, many proteins interact much weaker with ssDNA, without producing measurable changes in the mechanical properties of the template. In this case, a general method to study ssDNA-protein interactions consists of holding a ssDNA molecule between optically trapped microspheres and simultaneously visualizing interacting fluorescently labeled proteins [176, 25, 36]. Efficient application of this approach requires long ssDNA molecules to avoid the simultaneous presence of intense trapping and fluorescence excitation lasers in the vicinity of the fluorophores [171]. We thus designed constructs with different lengths: a short ssDNA (8,393 nt and 10,729 nt) and a long ssDNA (48,502 nt) (see Figure 29). A second, different class involves DNA molecules that can be converted into

ssDNA/dsDNA hybrids, having a junction with defined polarity and position (see Figure 29). Such molecules can be used as template for characterizing substrate specificity (ssDNA or dsDNA) of DNA-binding proteins, for mimicking the physiological invading template of homologous recombination or for exploring the activity of molecular motors such as DNA polymerases, with specific activity at the ssDNA/dsDNA junction.

4.3.1 DNA labeling and generation of single-stranded DNA using Optical Tweezers

In order to generate ssDNA by force-induced melting, only one strand of the dsDNA template has to be attached to the microspheres. Biotinylation is thus performed on the 3'- and 5'-end of one of the template strands. In our approach, we use sequential annealing and ligation of biotinylated oligonucleotides to linearized DNA templates. For generation of long ssDNA constructs (48517 nucleotides), we use linearized Lambda DNA and anneal and ligate oligonucleotides (oligonucleotide 1 and 2) to first biotinylate the 5' end of the template. A third modified oligonucleotide (oligonucleotide 3) is then hybridized and ligated to biotinylate the 3'-end of the template (see Figure 30.A). For shorter DNA constructs (8,393 nt and 10,729 nt), we first linearize DNA plasmids (e.g. pKYBI, pTR19-ASDS) using restriction enzymes to create suitable overhangs. A polymerization and digestion reaction creates a 3'-labeled end and a 3'-overhang. The final labeling is then performed by hybridizing and ligating a biotinylated oligonucleotide, (oligonucleotide 4 for pTR18-ASDS and Oligonucleotide 5 for pKYB1) in a similar fashion as for the long ssDNA construct (see Figure 30.B). To create DNA-hybrid constructs containing SDSJs with a defined polarity, we label DNA molecules on three of the 4 ends and introduced a nick at a defined position on the strand with only one labeled end (see Figure 29). Upon application of forces higher than 65 pN using optical traps, the untethered segment melts away, producing a hybrid of ssDNA and dsDNA with a defined junction. For generating this type of DNA constructs (see Figure 30.C), an oligonucleotides-based approach was used, similarly to that used for the first class of molecules. The first step consisted of the digestion of the DNA to create two non-complementary overhangs. Next, oligonucleotides were annealed and ligated to the extremities of the linearized DNA molecule, creating new 5'-overhangs. Depending on the

desired polarity (3′ or 5′) and the location of the junction (either at 20 or at 80% of the length of the DNA molecule), we used either biotinylated or non-biotinylated oligonucleotides. The new 5′-overhangs were filled in using Klenow exo-polymerase with either biotinylated or regular nucleotides. In the final step, a specific nicking enzyme was used to create a nick in the single-end-labeled strand. Finally, the constructs were tested at the single-molecule level using optical tweezers (see Figure 31).

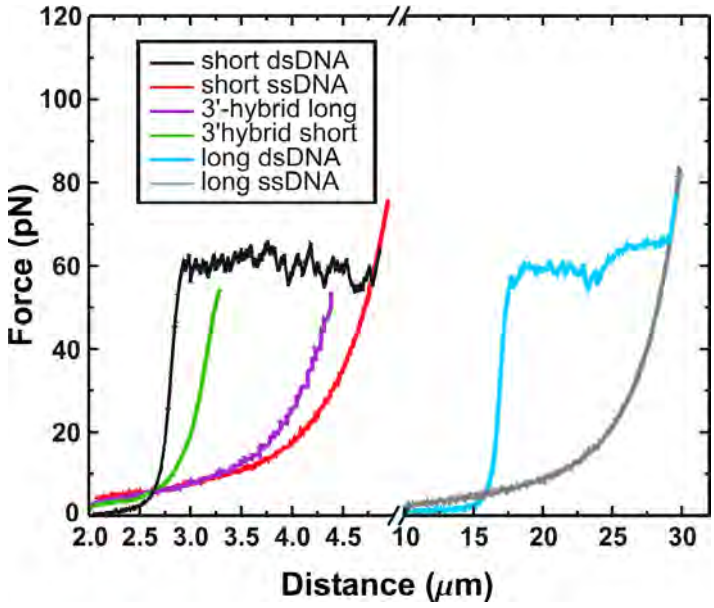

Figure 31.: Force-extension curves of different ssDNA constructs. Black: short dsDNA construct showing the typical low-salt saw-tooth pattern in the overstretching transition. Further increase of the bead separation induces melting of the untethered segment. Red: short ssDNA construct. Green and purple curves show the ssDNA-dsDNA hybrid constructs with 5′-overhang composed respectively of 20% and 80% of ssDNA. The cyan curve corresponds to the stretching curve of Lambda DNA. The light grey curve represents the force- distance behavior of the long ssDNA construct.

4.3.2 General Applicability of force induced DNA melting

Force-induced melting[173, 60] is a crucial step in our protocol for the generation of the ssDNA constructs.

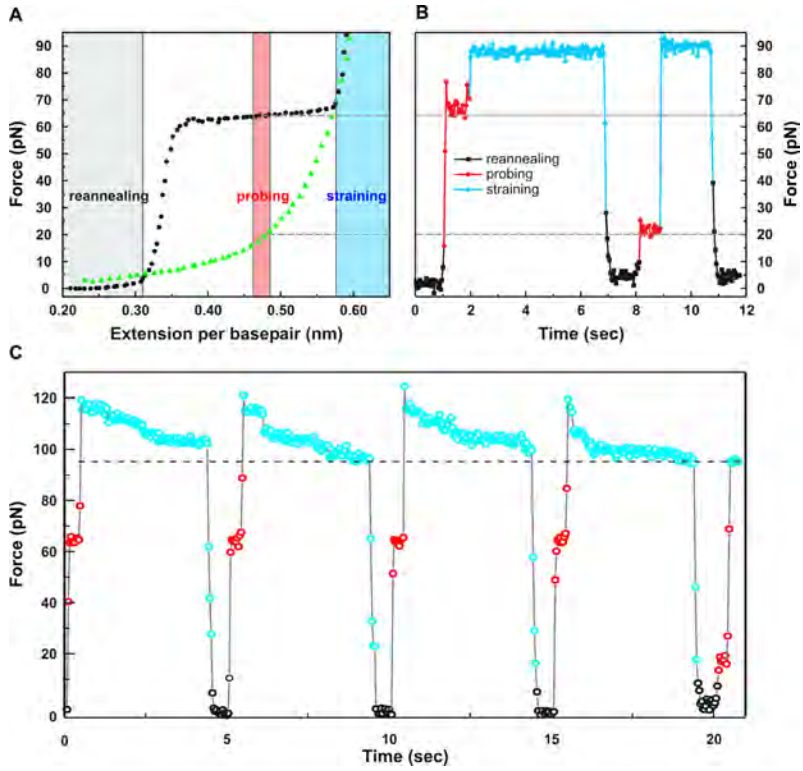

Figure 32.: **Characterization of force-induced melting using the short ssDNA construct (pTR19-ASDS).** [A] Force-extension measurement of dsDNA (black dots) and ssDNA (green triangles). To convert dsDNA into ssDNA, the molecule is exposed to cycles of successive straining, reannealing and probing. [B] Force-time traces at 50 mM NaCl. The extension is cycled between the straining, reannealing and probing regime, as indicated in panel A. The force drop from 65 pN to 20 pN in the second probing interval reveals that the conversion of dsDNA to ssDNA is completed within the prior 5 seconds straining interval. [C] Details of the dynamics of the final strand separation for the pTR19-ASDS DNA extended to a force of 120pN in 150mM NaCl. In the straining regime, the force drops significantly, until, after the fourth cycle, a force level of 95 pN is reached. At this force the DNA is fully melted to ssDNA, as can be seen in a force value of 20 pN in the last probing regime.

Therefore, we determined efficiency and time scale of force-induced melting for different DNA lengths at different ionic conditions. Our procedure involved three distinct steps (see Figure 32.A). First, the dsDNA was extended beyond overstretching to more than 0.58 nm per base pair (corresponding to a tension of approximately 80 pN, which we designate as the

"straining regime"). For a time ts (straining time), the dsDNA was allowed to melt. Second, the DNA was relaxed to a tension below 5 pN for a period of time (approximately 10 seconds) allowing the DNA molecules that only partially melted, to reanneal completely. After the reannealing step, the DNA has become either entirely double-stranded (when the melting process had not completed during the straining period), or single-stranded DNA (when melting had completed). Third, to probe the state of the DNA, we extended the molecule to 0.47 nm per base pair and measured the tension on the DNA. At this extension, the tension on dsDNA is 65 pN, while that on ssDNA is about 20 pN (see Figure 32) making it straightforward to discriminate between the two. We cycled multiple DNA molecules, one at a time, through such cycles of straining – reannealing - probing, until they melted completely into ssDNA, broke, or melted into an ssDNA/dsDNA hybrid.

We attribute the latter two events to the presence of nicks: breakage occurs in case the biotinylated strand is nicked; incomplete melting in case the non-biotinylated strand is nicked and only a segment of the strand is released in solution during melting. The melting efficiency (at different ionic strengths) is defined as the probability of producing a complete ssDNA tethers within a defined straining time. The melting efficiency can be therefore calculated only in experiments where complete melting take place and an intact ssDNA tether is finally produced. We restricted our analysis to only complete melting events, which amounts to approximately 30% of theλ-DNA molecules tested and about 50% of the shorter DNA tethers. This is in agreement with the nicking probability increasing with DNA length. The probability of a stable ssDNA molecule can be increased by reducing the amount of freeze- thaw cycles. Furthermore, longer dsDNA molecules, like lambda DNA, should be pipetted slowly and mixed gently, since shear forces in the liquid can potentially damage the molecule. Also, chemical impurities in the form of DNases, reactive oxygen species or other forms of mutagenic chemicals in the microfluidic system will give rise to a higher occurrence of nicks. In general, careful handling and use of freshly made DNA gives best results. Figure 32.B shows two typical probing–straining–reannealing cycles at 10 mM Tris-HCl pH 7.8 and 50mM NaCl. At the start of the experiment, the DNA was entirely double-stranded, as can be seen from the force value of 65 pN in the first probing interval. Within the next 5 seconds of straining, the molecule

completely melted into ssDNA, as is evident from the tension of only 20 pN measured in the second probing interval. For each DNA molecule showing such a tension drop in the probing period, we confirmed the complete melting into ssDNA by a complete force-extension measurement (see Figure 32). Previous single-molecule experiments have shown that the ionic strength of the buffer has a strong effect on the DNA melting process [60]. To obtain further insight in the melting process, we performed experiments at increasing salt concentrations. We observed that the dynamics of DNA melting changed significantly when raising the salt concentration. In Figure 30.C, we show an experiment similar to that in Figure 30.C, but performed at 150 mM NaCl and with a substantially higher mechanical strain applied (120 pN instead of 80 pN). In the straining regime, the force dropped significantly due to force-induced melting, until, after the fourth cycle, a force of 95 pN was reached as expected for fully melted DNA. Indeed, the DNA molecule fully melted into ssDNA, as is evident from the force of 20 pN in the successive probing cycle. To explore more systematically the impact of ionic strength, we repeated this experiment for the pTR19-ASDS DNA construct (N=121), with a constant straining force of 75 pN at different salt concentrations. We quantified our results by determining the melting efficiency, which we defined as the number of probing-straining-reannealing cycles required to fully melt all dsDNA molecules into ssDNA. This number equals one if all DNA molecules are converted to ssDNA in one cycle; less if it takes more attempts and zero if no melting occurs for this given straining time for all probed dsDNA molecules. Figure 33.A shows the melting efficiency of the pTR19-ASDS DNA construct for various straining times and ionic strengths. At 5 mM NaCl, a straining time of 1 second was sufficient to melt all probed DNA molecules. At the higher salt concentrations, the straining time had to be increased to 3 seconds (50 mM NaCl) or 5 seconds (150 mM NaCl), to obtain complete conversion into ssDNA after one cycle. Next, we increased the straining force to 110 pN to investigate the effect of DNA tension on the melting efficiency. We performed these experiments in 150 mM NaCl, using a straining time of 4 seconds to ensure that not all DNA would melt within one cycle. At a straining force of 110 pN, the melting efficiency was 0.6 ± 0.1 (mean$\pm$standard error of the mean), higher than at 75 pN (0.4 ± 0.1), as expected.

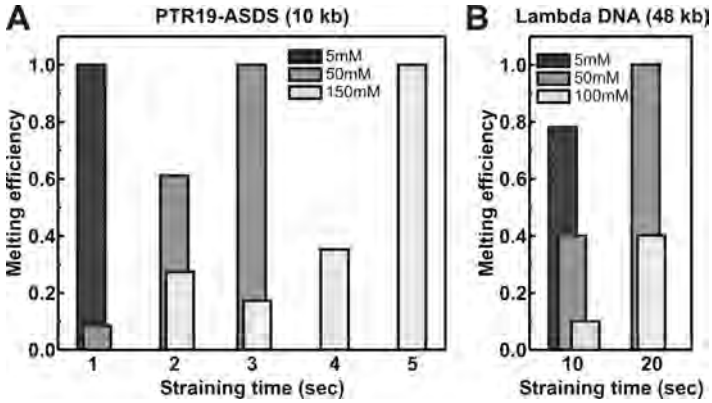

Figure 33.: Efficiency of force-induced melting for ssDNA production. [A] Histogram of melting efficiency at different salt concentrations and straining times, using the pTR19-ASDS DNA construct exposed to a straining force of 75 pN. [B] Melting efficiency for the long dsDNA constructs at different salt concentrations and straining times. The straining force, in this case, was set to 95 pN.

We also repeated the experiment with the SDSJ and the long ssDNA constructs. For the SDSJ DNA construct, we observed a very similar melting time for the untethered segment as for the short ssDNA construct. Upon release and successive extension of the molecules, we observed a change in the mechanical properties of the tethers that are compatible with the expected ratio between single and double-stranded DNA (see Figure 31). Finally, for the long ssDNA construct, although longer straining times (10-30 seconds) and higher tensions (about 110 pN) were required (see Figure 33.B), we could melt away the untethered strand, confirming the general applicability of force-induced DNA melting for molecules of different lengths and sequences (see Figure 31).

4.3.3 Preserving the integrity of ssDNA molecules during Optical Tweezers experiments

A significant challenge in optical-tweezers experiments is to preserve the integrity of the tethered DNA to allow for measurements lasting tens of minutes. Biotin-streptavidin and digoxigenin-antidigoxigenin bonds, the commonly used strategies to attach single DNA molecules to polystyrene microspheres, can be affected by the intense 1064 nm radiation used for

the optical trapping. Two effects play a role: (i) the generation of ROS on the polystyrene surface can affect the protein-ligand interactions and (ii) the short-lived ROS can cause DNA damages, including ssDNA breaks, close to the microspheres [91, 39]. It has been shown that increasing microsphere size and lower trapping power produce more stable dsDNA tethers [91]. To test whether this approach can also be used to prolong the lifetime of the substantially more fragile optically trapped ssDNA tethers, we applied the following experimental procedure: (i) dsDNA was tethered between two optically trapped microspheres using moderate light power (500 mW per trap), (ii) force-induced melting was performed at low salt condition (10 mM Tris-HCl pH 7.6, 10 mM NaCl) to produce ssDNA, (iii) ssDNA was held at the constant tension of 20 pN until breakage occurs in the observation buffer (20 mM Tris-HCl pH 7.6, 100 mM NaCl). We found that indeed the use of polystyrene microspheres with larger diameter significantly extended the lifetime of a ssDNA molecule in optical traps: tethers between 1.87 μm diameter microspheres had an average lifetime of 3 ± 1 minutes (mean$\pm$SD, N=71), whereas tethers between 4.26 μm diameter microspheres had a six-fold longer lifetime (18 ± 10 minutes, mean$\pm$SD, N=33). Considering that the presence of ROS affects the bond establishment between biotin and streptavidin and not the actual bond-lifetime [91], we can conclude that the tether loss can be attributed to the single-stranded breaks generated by the presence of ROS at the polystyrene surface [91]. Furthermore, we studied the effect of the trapping light power on the lifetime of ssDNA tether in the presence of beads with large diameters (4.26 μm). Increasing the trapping power from 500 mW to 3 W per trap induced a drastic shortening of the ssDNA lifetime from 18 to 2 minutes (2 ± 2 minutes, mean$\pm$SD, N=13). Confirming that the intensity of the trapping laser does negatively impact the lifetime of the ssDNA. Consequently, we can conclude that microspheres of larger diameter and the use of minimal trapping light result in more stable ssDNA tethers, which can be used for tens of minutes in single-molecule experiments.

4.4 DISCUSSION

Currently, many methods studying cellular processes on ssDNA, such as fluorescence polarization anisotropy, surface plasmon resonance and FRET-

based techniques, employ short homopolymeric substrates [63]. Using kilobase-long and heterogeneous sequences of ss DNA substrate mimics more closely the in vivo situation. The ability to perform single-molecule experiments on these substrates can complement, verify and extend the understanding of essential cellular processes occurring on ssDNA. Here we have provided detailed and generalized protocols for the force-induced generation of long ssDNA and SDSJ templates for optical tweezers experiments. We circumvent the many technical challenges for the manipulation of long ssDNA – the difficulty to label and form a ssDNA tether in flow - by the use of force-induced melting. First of all, we use well-established labeling techniques to label dsDNA on the same strand. Next, a tether is formed by flow-stretching dsDNA between two optically trapped microspheres and ssDNA is created using force-induced melting. By adapting this method, no addition of denaturing chemicals or exonucleases is necessary and there is no need for an extra cleaning step of the flow cell. We also report a straightforward and efficient protocol for the formation of ssDNA/dsDNA junctions constructs to study DNA polymerases or the differential binding of a protein to ss- and dsDNA. The use of a junction construct has been reported previously, where it was created by an exonuclease [78]. However, that approach did not allow the control of position and orientation of the junction, because exonuclease III only digests 400 nucleotides in the 3′- 5′ direction. By using a nicking enzyme in combination with force-induced melting, we were here able to create different oriented junctions at well-defined positions. We have also shown that force-induced melting is a generally applicable method that can be used irrespective of DNA sequence and length. In addition, we have demonstrated that force-induced melting can be employed over a broad range of salt concentrations up to the physiological range. Finally, as shown previously for dsDNA [91], the use of larger microspheres increased the lifetime of ssDNA tethers, allowing optical tweezers experiments on a single ssDNA tether for tens of minutes. We quantified that there is a six-fold lifetime increase when 4.26 μm microspheres are used instead of 1.87 μm microspheres. The protocols to generate ssDNA using optical tweezers presented here represent a convenient toolbox for reliably generating ssDNA substrates for optical-tweezers experiments without the use aggressive chemicals or enzymes. These protocols will facilitate future single-molecule experiments on a large number of genomic transactions, like the

assembly of RecA/Rad51 filaments, the binding-specificity of proteins and the dynamics of DNA polymerases.

5 FORMATION OF RAD51 FILAMENTS

VISUALIZATION AND QUANTIFICATION OF RAD51 FILAMENTS AT SINGLE-MONOMER RESOLUTION

The RAD51 nucleoprotein filament is the molecular species responsible for the reaction of homologous recombination (HR), an essential pathway of double-strand break DNA repair. Fundamental aspects of the mechanism of RAD51 filament-formation concerning its nucleation, selectivity for single-stranded DNA and growth rate, remain unclear. Here we combine fluorescence microscopy, optical tweezers and microfluidics to quantify the assembly of RAD51 filaments with single-monomer resolution. We show that the filaments are seeded from RAD51 nuclei that are heterogeneous in size, reflecting the presence of a range of RAD51 oligomeric species in solution. We propose that the heterogeneity arises from the energetic balance between RAD51 self-assembly in solution and the size-dependent interaction of the nuclei with DNA. The process of RAD51 nucleation is intrinsically selective, strongly favoring filament formation on single-stranded DNA. Furthermore, using a new single-molecule fluorescence recovery after photobleaching (FRAP) assay we can independently observe filament nucleation and growth, permitting direct measurement of the cooperativity of RAD51 filament formation. Our findings yield a comprehensive quantitative understanding of RAD51 function in HR and could make the suggested regulation by recombination mediators such as BRCA2 redundant. Finally, the strong preference of RAD51 for ssDNA implies a structural basis for recently proposed break-independent role of RAD51 at active replication forks.

5.1 INTRODUCTION

Biological and medical relevance of RAD51 filament formation

The formation of RAD51-nucleoprotein filaments on ssDNA is a crucial step in homologous recombination (HR), an important DNA-repair pathway activated in response to DNA double-stranded breaks. In vivo, nucleoprotein filament assembly and disassembly are regulated by accessory proteins [159, 142]. Defects in HR are involved in carcinogenesis [73] and are targeted by anti-tumour drugs [110]. The tumour suppressor protein BRCA2, for example, directly interacts with RAD51 and is involved in the assembly of RAD51 filaments on ssDNA. It has been proposed that RAD51-filament formation follows a two-step mechanism, consisting of a nucleation and a growth phase [109, 169, 6, 72]. Nucleation, the minimal form of stable RAD51 binding, has been proposed to represent the critical step of filament formation [76]. Currently, the physical mechanism underlying the minimal size requirement is unknown and the number of RAD51 monomers constituting a single nucleus has never been measured directly.

Is RAD51 filament-formation selective?

Also, RAD51 can form filaments on both ssDNA and dsDNA. A proposed role for recombination mediators, is to remodel RAD51 filaments [124] and selectively load RAD51 onto ssDNA [27, 151, 83, 165, 28]. However, experiments comparing RAD51-filament formation rates on ssDNA and dsDNA and the effect of recombinase mediators in modulating RAD51 binding selectivity have yielded contrasting outcomes [105, 109, 27, 162, 68, 28]. The persistence of these controversies is due to the fact that the direct visualization and counting of individual RAD51 proteins binding on ssDNA and dsDNA of identical sequence and length has, until now, remained impossible.

A new approach to study RAD51-ssDNA interaction

In this study, we combined fluorescence microscopy, dual-trap optical tweezers, micro-fluidics [25] and force-induced DNA melting [60] to monitor individual RAD51 nuclei on both ssDNA and dsDNA with single-monomer resolution. From this analysis, we have built a physical model that explains both the minimal size requirement for RAD51 nucleation and the reported non-linearity in the binding rate observed at the single-molecule level [55, 169, 72, 12]. Next, we adapted the FRAP technique to our single-molecule assay and determined nucleation and growth rates separately, therefore measuring directly the cooperativity of RAD51 polymerization for ssDNA and dsDNA at different forces without the need of any mathematical modeling. Using force-induced melting of duplex DNA

and gapped DNA constructs we revealed unequivocally a strong intrinsic binding preference of RAD51 for ssDNA. Finally, our approach was used to clarify the effect of BRCA2 BRC4 on RAD51 filament formation on ssDNA in different assembly conditions.

5.2 MATERIALS & METHODS

5.2.1 Combined optical tweezers, fluorescence microscopy and microfluidics setup

The experimental setup has been described elsewhere in detail. In brief, our combined dual optical trapping and single-molecule fluorescence setup is built around an inverted microscope (Nikon Eclipse TE2000-U). Optical traps are generated by a powerful near-IR laser (Ventus 1064 nm, 3W, Laser Quantum, Cheshire, Uk). An optical isolator (Newport 1030-1080 ISO-FRDY-OPT) is placed directly in front of the laser output to prevent coupling of back-reflections into the laser cavity. A combination of a zero order half-wave plate (WPH10M-1064, Thorlabs) and a polarizing beam splitter (10BC16PC.9, Newport, Irvine, CA) is used as a power regulator. A second zero order half-wave plate (WPH10M-1064, Thorlabs) and polarizing beam splitter (10BC16PC.9, Newport, Irvine, CA) are used to set the linear polarization and split the laser into two independent beams. After splitting, a Galilean telescope (1:2.67) is used to obtain the desired beam diameter (approximately 8 mm) and to steer the trap position. In one path, computer-controlled steering is achieved by displacing the first telescope lens with motorized actuators (T-LA28, Zaber Technologies Inc., Richmond, BC, Canada). The two beams are recombined using a second polarizing beam splitter (10BC16PC.9, Newport, Irvine, CA) and coupled into a high-NA water-immersion objective (PlanApo 60X, NA 1.2, Nikon) via a dichroic mirror (950 dcsp, Chroma Tech Corp, Rockingham, VT). The focusing power of the objective produces a three-dimensional optical trap where individual beads can be trapped and manipulated. Force detection is achieved by collecting the transmitted trapping light via a high NA oil-immersion condenser (Achromat/Aplanat, NA 1.4, Nikon) and imaged on a position-sensitive diode (DL100-7PCBA3 - Pacific Silicon Sensor) using a

single achromatic lens. Rejection of the unwanted polarization is achieved by a polarizing beam splitter (10BC16PC.9, Newport, Irvine, CA).

The end-to-end distance of the DNA is monitored by acquiring bright-field images of the trapped beads. Illumination of the sample is performed by a blue LED (LXHL-NB98 Luxeon Star/O, Lumileds) a single lens and a dichroic mirror and images are recorded using a CCD camera (CCD-902K, Watec) and digitized by a frame grabber.

Fluorescence excitation is performed using wide-field strategy. Alexa-Fluor 555 is excited by a 532 nm laser (GCL-0.25L, 25 mW, Crystal laser, Reno, NV). The fluorescence excitation beam is first expanded and then coupled into the microscope via a dichroic mirror (z532rdc, Chroma Technology Corp.) and a lens. The emitted fluorescence signal is passed through a band-pass filter (hq575/50m, Chroma Technology Corp.) and imaged on an EMCCD camera (Cascade 512B, Princeton instruments, Monmouth Junction, NJ) and read using the Winview software.

A glass, custom-fabricated, multi-channel laminar flow-system is used to obtain parallel flow and to rapidly exchange buffer during the experiment. Image analysis is performed using a custom-written program in Labview (National Instruments).

5.2.2 RAD51 fluorescent labeling

RAD51 (isoform Q313, variant C319S) fluorescent labelling with Alexa555 was performed as previously described [114]. The degree of labelling, as characterized using mass spectrometry was 1.3. This method allowed us to exclude the presence of unlabelled RAD51 proteins in the preparation. Therefore we expect that 1 out 4 RAD51 proteins contains a non-specifically attached fluorophore. Biochemical characterization showed that RAD51 (C319S) is proficient in ATP hydrolysis, strand-exchange and DNA binding. Also this fluorescent RAD51 mutant has been extensively used and characterized in previously published single-molecule work [135, 114, 173].

5.2.3 Preparation of DNA construct

To produce a 38.412 kbp construct having biotin labels on the ends of the same strand we started our reaction by digesting Phage Lambda dsDNA (0.25 mg/mL) with ApaI Fast Digest (30 minutes at 37°C). This reaction

yielded two different products, a 10 kbp and a 38.4 kbp dsDNA. Afterwards, in the same tube, we added Klenow buffer (final concentration 0.28x), nucleotides (dGTP, dTTP, final concentration 0.067 mM), biotin-modified nucleotides (biotin-14-dACTP and biotin-14-dCTP, final concentration 0.043 mM) and Klenow DNA polymerase exo- (final concentration 0.07 U/μL). The polymerization was carried out at 37°C for 30 minutes. The reaction was heat-inactivated (10 minutes at 75°C) and ethanol precipitated. The pellet was resuspended in 50 μL of 10 mM Tris pH 7.5.

The second part of the protocol consisted in annealing of a primer containing 4 biotin d-TTP (incubation 15 minutes at 65°C, primer sequence: 5 '-cTcTcTcTctcttccttctcttggcc 3', final concentrations 1 μM, capital letters indicate biotin-positions). The hybridized primer was ligated with T4 DNA Ligase (45 minutes at RT, T4 DNA Ligase final concentration: 1 U/μl). The reaction was heat inactivated (5 minutes at 65°C) and ethanol precipitated.

To produce a 48.512 nt ssDNA melting Lambda DNA was biotinylated at the 3' and 5' end of the same strand using three oligonucleotides. First, the 5'-end of Lambda DNA and oligonucleotide 1 (5'- ggg cgg cga cct gga caa-3') and 2 (5'- agg tcg ccg ccc ttt ttt tTt TtT-3') were phosphorylated for 30 min at 37°C in a reaction containing 14 nM Lambda DNA or 10 μM of the oligonucleotide and 0.25 U/μl of T4 Polynucleotide Kinase in 1x T4 Ligase buffer (Fermentas). Next, oligonucleotides 1 and 3 (5'- TtT tTt ttt ttt aga gta ctg tac gat cta gca tca atc ttg tcc-3') were annealed to the overhangs of Lambda DNA in a 10:1 oligonucleotide: DNA ratio (total volume 500 μl) by heating the reaction to 65°C and slowly cooling down to room temperature. The ligation reaction was then initiated by adding T4 DNA ligase (0.02 U/μl) and carried out for two hours. Next, oligonucleotide 2 was annealed in a 100:1 ratio to the Lambda DNA construct by incubation at 45°C for 30 minutes. Subsequently, the oligonucleotide was ligated to the DNA at room temperature. Finally, the DNA was purified by ethanol precipitation.

5.2.4 Experimental Conditions

Beads catching, DNA tethering, RAD51 incubation and fluorescence imaging were performed in the following conditions (unless otherwise mentioned): 25 mM Tris pH 7.5, 100 mM KCl, 1 mM CaCl2, 0.5 mM ATP and 10 mM DTT. DNA overstretching and melting was performed in 10 mM Tris pH 7.5, 25 mM KCl, 1 mM CaCl2, 0.5 mM ATP and 10 mM DTT.

5.2.5 Fluorescence Anysotropy measurements

Fluorescence anisotropy measurements were recorded in a PHERAstar FS plate reader (BMG Labtech; Germany) equipped with a fluorescence polarisation optic module (excitation = 485 nm; emission = 520 nM). The anisotropy was measured at 37°C in black 96-well half area, flat bottom, NBS plates (Corning; USA). The instrument was set to top optic measurement mode and the gain and focal height were set using the instrument software against free fluorescein (Fluorescein Sodium; Fluka) in 50 mM Tris-HCl pH 8.0 (mP = 35).

Wild-type human RAD51 (100 nM) was incubated with increasing concentrations of human BRC4 peptide at room temperature for 10 minutes in binding buffer (50 mM Tris-Acetic Acid pH 8.0, 150 mM KCl, 2 mM $MgCl_2$, 2.2 mM ATP, 1 mM DTT). After equilibration for 5 minutes at 37°C, the binding reaction was initiated by the addition of 10 nM (final concentration) Fluorescein-labelled ssDNA, using the PHERAstar FS built-in injectors. Reading intervals were 0.2 second for the first 2.5 seconds, followed by 1 second intervals for 1 minute, using 50 flashes per data point. Steady-state measurements were taken every 5 minutes, using 200 flashes per time point until the signal was stable.

RAD51 concentrations were determined by UV spectroscopy using theoretical extinction coefficients determined from the amino acids sequence (http://www.expasy.ch/tools/protparam.html). Human BRC4 peptide (LKE PTL LGF HTA SGK KVK IAK ESL DKV KNL FDE KEQ M) concentration was determined by amino acid analysis (Protein and Nucleic Acid Chemistry Facility, Department of Biochemistry, University of Cambridge). A 60 nucleotide long 5'-fluorescein-labeled ssDNA was purchased from Integrated DNA Technologies (IDT, USA). The DNA sequence (5' F-ATG GTG TGT GTA GGT TAA TGT GAG GAG GAG AGG TGA AGA AGG AGG AGA GAA GAA GGA GGC 3') was designed to minimize secondary structure and dimer formation using the NUPACK nucleic acid package (http://www.nupack.org).

5.3 RESULTS

5.3.1 RAD51 nucleation on ssDNA

Single-molecule approach

To quantify directly the rate and size of RAD51 nucleation on ssDNA, we used force-induced melting to denature a dsDNA molecule labelled with biotins at the 3′ and 5′ ends of the same strand using dual-trap optical tweezers in order to obtain a ssDNA tether [60]. Next, we employed a multi-channel microfluidic system [22, 59, 25, 51] and incubated the ssDNA molecule at a defined tension (in the 5 to 50 pN range) with fluorescently labelled (Alexa555) RAD51 [114] in the presence of ATP and Ca^{2+}. After incubation, the ssDNA molecule was repositioned in the imaging channel and inspected using fluorescence microscopy. The number of fluorescent RAD51 spots appearing after a given incubation period were counted in a low-coverage regime to insure single-nucleus resolution (less than 10 spots per ssDNA molecule at 100 mM KCl, 1 mM $CaCl_2$, 0.5 mM ATP) and divided by the length of the ssDNA molecule. The thus determined nucleation rates were found to depend strongly on RAD51 concentration (see Figure 34.A)), ranging from 10^{-7} $s^{-1}nt^{-1}$ to 10^{-5} $s^{-1}nt^{-1}$ ([RAD51]=7.5 to 75 nM). The nucleation rates (k_{nucl}) did not depend linearly on the RAD51 concentration but could be well described by a power-law ($k_{nucl}=k_0[RAD51]^n$). The fitting parameter n, the Hill coefficient, has been interpreted before to represent the minimum number of monomers required to obtain a stable nucleusv[55, 72, 12]. Our fit yields $k_0=(1\pm1)x10^{-8}$ s^{-1} nt^{-1} and n=1.5±0.3. According to the canonical interpretation, this would indicate that RAD51 nucleation requires a dimer [55, 169, 72, 12]. In order to get a deeper understanding of the nucleation process, we determined the nucleus size directly, by counting the number of RAD51 monomers in a nucleus using calibrated fluorescence intensity [25]. The calibration was performed using intensity drops due to photobleaching of the fluorescent labels. Under our experimental conditions, a single Alexa555 produced 460±160 counts per 500 ms (mean±standard deviation, see Supplementary Figure S38) [25]. To estimate the size of RAD51 nucleation, care was taken to discriminate between filament nucleation and growth by using low RAD51 concentrations (12.5 nM) and short incubation times (70 seconds). In this regime, we detected on average a single RAD51 nucleus per incubation. Experiments addressing filament growth

Nucleation rate of RAD51

Composition of RAD51 nucleus

and cooperativity (discussed later) allowed us to conclude that under these conditions, 90% of the observed clusters resulted from an individual binding event from solution, hence they reflect dominantly RAD51 nucleation. We found that RAD51 nuclei are heterogeneously distributed in size (see Figure 34.B), ranging from individual RAD51 monomers and dimers (see supplementary figure S40) up to a significant population of hexamers, indicating that preassembled species of RAD51 can readily nucleate on ssDNA without the need of remodelling factors. We confirmed that RAD51 in solution is distributed in a collection of distinct oligomeric states using cross-linking gel experiments (see supplementary figure S41), these oligomeric states in solution have also been reported before [189, 44, 122].

Size-dependent stability of RAD51 nuclei

The observation that the concentration dependence of the RAD51 nucleation rate follows a 1.5 power-law, while the size of RAD51 nuclei is broadly distributed might indicate that the stability of RAD51 nuclei on ssDNA is size-dependent. To test this, nucleation experiments were performed at low RAD51 concentration (12.5 nM RAD51, 0.5 mM ATP, 1 mM CaCl2, 100 mM KCl and 70 seconds incubation time) and the resulting RAD51 nuclei were observed for extended periods of time (up to 30 minutes, in the absence of RAD51 in solution) by taking fluorescence snapshots every 30 seconds in order to minimize photo-bleaching. In Figure 34.C an example illustrating the intrinsic instability of RAD51 nuclei is shown. One of the nuclei stayed bound on the ssDNA for the whole measurement, while the other one disappeared suddenly. It is highly unlikely that the sudden fluorescence intensity drop was caused by the simultaneous photobleaching of both fluorophores at once. Therefore, we attributed such intensity drop to the release into solution of the entire RAD51 nucleus. Next, we correlated the lifetime of the nucleus to the number of RAD51 monomers (see Figure 34.D), finding that RAD51-nucleus stability (cumulative probability of remaining bound to ssDNA for longer than 6 minutes) depends on size, in agreement with our initial hypothesis. The clear correlation between size and lifetime indicates that the initial phase of filament formation is characterized by the unstable binding of small RAD51 nuclei, needing additional monomers or mediator proteins to stabilize the nascent filament. Next, we tested whether the RAD51-nucleation rate is influenced by monovalent salt concentration. We found that the rate of RAD51 nucleation on ssDNA decreases approximately by 10-fold by increasing the salt concentration from 50 mM to 400 mM KCl. Finally, the RAD51-nucleation

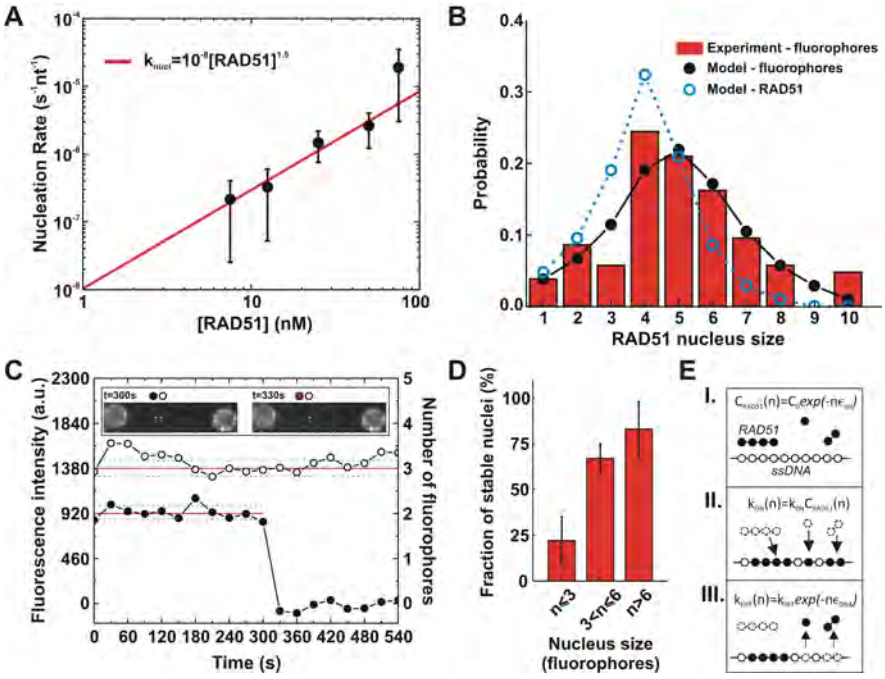

Figure 34.: RAD51 nucleation on ssDNA. [A] RAD51-concentration dependence of nucleation rate; black dots: experimental data (error bars represent the standard deviation); red line: power-law fit ($k_{nucl} = k_0[RAD51]^n$) yielding an exponent n of 1.5±0.3. [B] Histogram of nucleus sizes; red bars: experimental data (N=105); black, solid circles: model fit of distribution of number of fluorophores per nucleus; blue circles: distribution of expected number of RAD51 monomers per nucleus obtained from model fit (see Supplementary Information). [C] Fluorescence intensity time traces of individual RAD51 nuclei bound to ssDNA. Solid circles: RAD51 nucleus consisting of 2 fluorophores, detaching between 300 and 330 seconds. Hollow circles: RAD51 nucleus consisting of three fluorophores remaining ssDNA bound for more than 9 minutes. [D] Bar diagram showing how stable nucleus fraction depends on nucleus size. Error bars: standard deviation according to binomial distribution statistics. [E] Kinetic model of RAD51 filament formation in which assembly and disassembly are regulated by the free energy parameters ϵ_{sol} and ϵ_{DNA}.

rate on ssDNA was determined in the presence of Mg^{2+}. The nature of the divalent cation (Ca^{2+} or Mg^{2+}) has important consequences for filament stability [174] and ATP-hydrolysis [166]. We observed that the rate of RAD51 nucleus formation on ssDNA was in the same order of magni-

tude when either Ca^{2+} or Mg^{2+} is used ($1.9x10^{-5}$ s^{-1} nt^{-1} in Ca^{2+} and $0.7x10^{-5}$ s^{-1} nt^{-1} in Mg^{2+}, [RAD51]=75 nM).

5.3.2 RAD51 filament growth

Single-molecule FRAP for measuring RAD51 cooperativity

Next, we focussed on the growth phase of RAD51-filament formation on ssDNA. We disentangled the nucleation from the growth phase by adopting a single-molecule fluorescence recovery after photobleaching method (sm-FRAP): after a first incubation step, nuclei were visualized in the imaging channel, their position recorded and afterwards completely photobleached. This was followed by subsequent incubation, detection and photobleaching cycles. Fluorescence images obtained from consecutive incubations were superimposed and growth events were scored when fluorescent patches colocalized (see Figure 35). The number of RAD51 monomers added per incubation was determined from the fluorescence intensity, revealing that also filament growth occurs by incorporation of various types of RAD51 multimers, including monomers (see supplementary figure S42). Also, the probability of RAD51 growth was determined, which was defined as the fraction of filaments exhibiting growth, divided by the incubation time. The measurements obtained should be taken as a lower estimate, since some of the nuclei might have disassembled from the DNA during subsequent incubations, but were still accounted for in the normalization. Following this procedure, we estimated the probability of RAD51 nuclei growth to be $(8\pm6)x10^{-4}$ s^{-1} $filament^{-1}$ (mean±SD, N=32) at 12.5 nM RAD51. The ratio between growth and nucleation rate, referred to as the cooperativity, could therefore be directly measured without the need of mathematical modelling. We found that the cooperativity value for RAD51 filament formation on ssDNA is about 2500 (considering that the nucleation rate at 12.5 nM is $3.3x10^{-7}$ $s^{-1}nt^{-1}$).

5.3.3 RAD51-filament formation is highly substrate-specific

We also tested how the rate of RAD51-filament assembly is affected by the DNA substrate. ssDNA and dsDNA molecules were kept under a tension of 20 pN, incubated in 75 nM RAD51, moved to the observation channel and fluorescence images were taken. Figure 36 shows images of RAD51

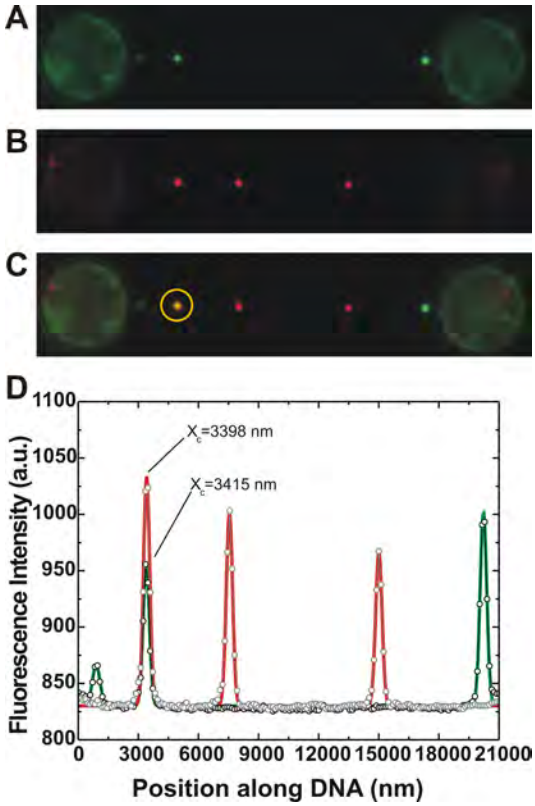

Figure 35.: Sm-FRAP allows detection of RAD51 growth on ssDNA. [A] Fluorescence image showing 3 individual fluorescent RAD51 nuclei on ssDNA. Subsequent continuous laser illumination resulted in complete photobleaching of the nuclei (not shown). [B] Fluorescence image of the same ssDNA-RAD51 complex after an additional incubation period. Fluorescent image shows the appearance of three distinct fluorescent patches. [C] Superposition of image [A] and [B] allows distinguishing new nucleation events from RAD51 growth. In the yellow circle we show that two of the fluorescent patches obtained from consecutive incubations co-localize exactly. [D] Line profile and Gaussian fitting of image A and B confirm the co-localization of the two patches with a resolution below 20 nm. This confirms the direct separate detection of RAD51 nucleation and growth on ssDNA.

filaments bound to ssDNA and dsDNA after incubations of 15 and 480 seconds, respectively.

Compared to the ssDNA, the dsDNA contained a far lower number of filaments, directly demonstrating that the nucleation rate of RAD51 for

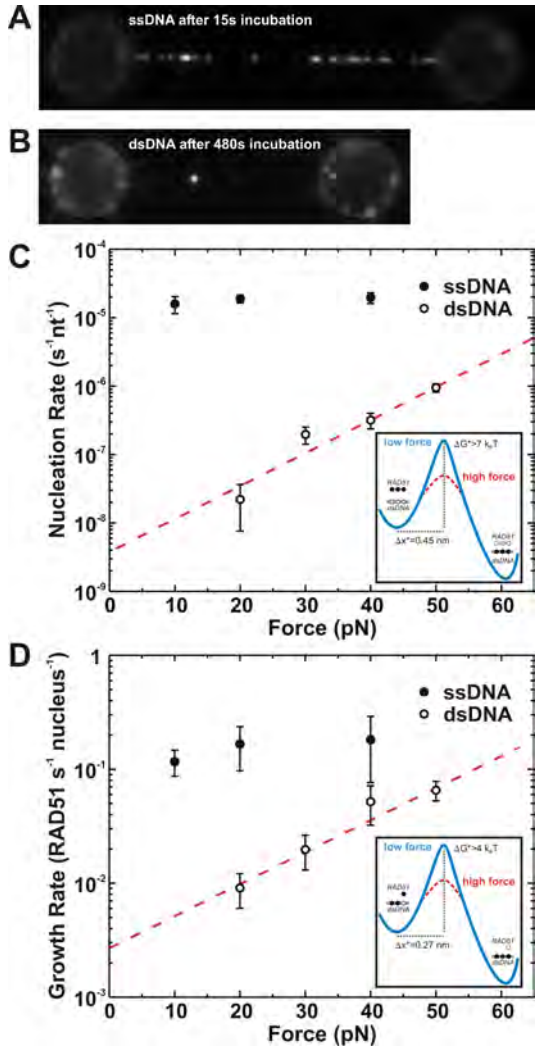

Figure 36.: Selectivity of RAD51 binding. [A] ssDNA molecule after RAD51 incubation ([RAD51]=75 nM); [B] dsDNA molecule after RAD51 incubation ([RAD51]=75 nM). [C] Rate of RAD51 nucleation versus applied tension for ssDNA (solid circles) and dsDNA (hollow circles). In the inset the proposed free energy diagram of the RAD51 nucleation process. [D] Rate of RAD51 filament growth versus applied tension for ssDNA (solid circles) and dsDNA (hollow circles).

ssDNA is much higher than for dsDNA. This result was confirmed in different buffer conditions using a gapped DNA construct containing both an ssDNA and a dsDNA segment (see supplementary figure S43). To quan-

titatively describe the differential affinity, nucleation and growth rates (using the sm-FRAP method) were determined for both ssDNA and dsDNA at various applied tensions (see Figure 36.C and Figure 36.D).

RAD51 nucleation and growth rates as a function of DNA tension

From the graphs, two key aspects are immediately clear: (i) nucleation and growth are systematically faster on ssDNA than on dsDNA, within the force regime explored; (ii) nucleation and growth are strongly force-dependent on dsDNA, but are not on ssDNA. At zero tension nucleation is 5000-fold faster on ssDNA than on dsDNA; in addition, growth is also faster on ssDNA than on dsDNA (approximately 100 times). Values for the cooperativity could be obtained both for ssDNA ($\sim$2500) and dsDNA ($\sim 10^6$ at zero tension down to $6x10^4$ at 50 pN). We independently confirm that RAD51 binding is faster on ssDNA substrates using fluorescence anisotropy measurements (see supplementary figure S44). Taken together, these results show that RAD51 has a strong intrinsic preference for forming filaments on ssDNA over dsDNA in the absence of recombinase mediators, such as BRCA2.

The force dependence of nucleation and growth on dsDNA could be well fitted with an Arrhenius-law based model ($k(F)=k(0)Exp[-F\cdot\delta x/k_BT]$, where F is the force acting on the dsDNA, δx the distance to the transition state along the reaction coordinate and k_BT the thermal energy [174]. The fits yield δx_{nucl}=0.45±0.05 nm and $k_{nucl}(0)=(4\pm3)x10^{-9}$ s^{-1} bp^{-1} for nucleation (see Figure 36.C) and δx_{growth}=0.27±0.03 nm and $k_{growth}(0) = (3\pm1)x10^{-3}$ s^{-1} $filament^{-1}$ for filament growth (see Figure 36.D).

5.3.4 Effect of BRC4 on RAD51 filament formation

In cells, homologous recombination is tightly regulated by so-called recombination mediator proteins [73, 159, 142].

We studied the kinetics of RAD51-filament assembly on ssDNA molecules of various lengths and sequences in the presence of the BRC-repeat peptide BRC4, one of the RAD51-binding domains of BRCA2. RAD51-filament formation was measured at the single-molecule level using long random sequences of ssDNA (48'512 nt) in both sub-stoichiometric (1:0.5 (RAD51:BRC4)) and excess quantities of BRC4 (1:1 and 1:5). When pre-incubated with RAD51, BRC4 blocked RAD51 filament formation at all concentrations tested and in different buffers (see Figure 37).

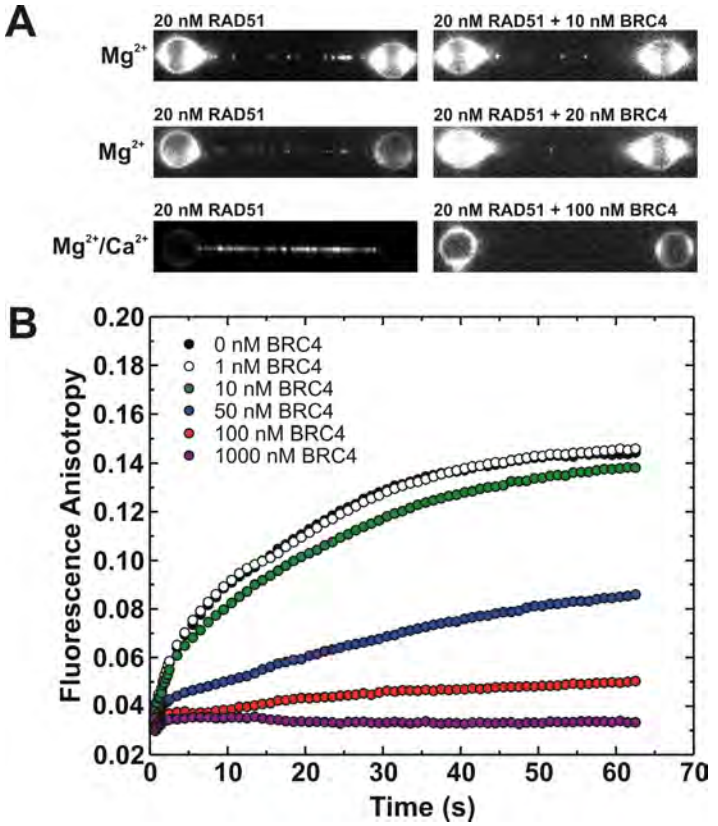

Figure 37.: Effect of BRC4 on RAD51-filament formation. [A] FInhibitory effect of BRC4 on RAD51-nucleoprotein-filament assembly on ssDNA. From left to right: filament formation in absence and in the presence of BRC4 at indicated RAD51:BRC4 ratios. RAD51 concentration was 20 nM in all measurements. A clear inhibitory effect was observed in Mg^{2+}, Mg^{2+}/Ca^{2+} (20mM Tris pH 7.5, 10 mM $MgO(Ac)_2$, 2 mM $CaCl_2$, 2 mM ATP) and Ca^{2+} buffer. [B] Fluorescence polarization anisotropy measurements of the rate of RAD51 (100 nM) assembly on fluorescein-labelled 60-nucleotide long ssDNA (10 nM) confirmed that BRC4 repeats inhibits RAD51 binding to ssDNA. Each data point represents the average of three independent experiments.

BRC4 acts as inhibitor of RAD51 filament formation on ssDNA

Using sub-stoichiometric amounts of BRC4, we observed approximately a two-fold reduction in RAD51 binding to ssDNA, while inhibition was complete when BRC4 was present in excess. These observations were confirmed by ensemble fluorescence-anisotropy experiments on a short heteropolymeric ssDNA (60 nt), which showed a purely inhibitory effect of

BRC4 on RAD51 filament formation for all RAD51:BRC4 ratios tested (see Figure 37). Exposure of pre-formed RAD51 filaments to BRC4 did not result in any noticeable disassembly. Finally, using a fluorescently labeled BRC4 (BRC4-Alexa488), we found that stable association to RAD51-ssDNA filaments does not occur, differently to what has previously reported.

5.4 DISCUSSION

Several kinetic schemes have been put forward to describe the mechanism of RAD51 filament formation, differing mainly in the proposed fundamental units of nucleation, growth and cooperativity number [109, 169, 6, 72].

Kinetic scheme of RAD51 filament formation

Our approach shows that RAD51 nucleation does not involve a unique RAD51 species as previously anticipated, but is intrinsically heterogeneous. The observation that RAD51 is present in solution as oligomeric species that are competent for filament nucleation removes the requirement for a potential involvement of BRCA2 in topological remodelling of RAD51 into a form that is suitable for DNA binding.

RAD51 nucleation is regulated by size-dependent stability

We propose a novel kinetic scheme (see Figure 34.E) for RAD51 nucleation based on our findings that (i) in solution a range of RAD51 oligomeric species is present that are competent for binding ssDNA and (ii) the stability of RAD51 nuclei bound to ssDNA is size-dependent. These observations can be modelled introducing two free energy parameters with a direct physical interpretation: (i) ϵ_{sol}, describing the RAD51 monomer-monomer interaction in solution and (ii) ϵ_{DNA}, the contribution of each RAD51 monomer to the energy barrier of dissociation of the nucleus from the ssDNA. The probability of observing a RAD51 nucleus of n monomers after an incubation time period t then can be expressed as (for derivation, see Appendix A):

$$p\left(n,t\right) = \frac{k_{on}\left(n\right)}{k_{off}\left(n\right)}\left(1 - e^{-tk_{off}(n)}\right) \tag{2}$$

where k_{off}(n) and k_{off}(n) are the unbinding and binding rate of RAD51 nuclei with size n. k_{on}(n) is proportional to the concentration of RAD51 oligomers with size n in solution ($k_{on} \propto$ C(n)). For an equilibrated solution, we have: $k_{on}\left(n\right) = k_0 e^{-n\epsilon_{sol}}$). To unbind, RAD51 has to overcome an

energy barrier linearly dependent on nucleus size, therefore: $k_{off}(n) = k_0 e^{-n\epsilon_{DNA}}$).

Maximum-likelihood fitting of this model to our data (See Supplementary Information) resulted in a nucleus-size distribution that matches our experimental observations (see Figure 34.A). According to our fit, every RAD51 monomer contributes to the overall stability of the nucleus) with an amount equal to ϵ_{DNA} = 1.8±0.5 k_BT. The interaction energy between RAD51 monomers in solution depends on the concentration and is ϵ_{sol} = 1.1±0.3 k_BT at [RAD51]=12.5 nM (see Supplementary Information). In the nucleation phase, therefore, RAD51 monomers and dimers nucleate onto ssDNA very frequently because more abundant, but relatively inefficiently due to their small interaction energy with ssDNA. Larger RAD51 multimers (3-6 protomers), although less abundant, nucleate readily, forming stable seeds for filament formation.

Following our formalism, we investigated the expected effect of varying protein concentration on the observed nucleation rate and apparent Hill coefficient. We predict that the apparent Hill coefficient in the concentration range used in our experiments (7.5 to 75 nM) should vary between 1.2 and 2.1, with an average value of 1.6, which is in agreement with our experimental observation. Previous studies on recombinase proteins [55, 72, 12] interpreted the Hill coefficient as the minimal nucleation unit. Here we show that this simplistic interpretation may be in general not valid. Our thermodynamic model provides a more general framework for the interpretation of nucleation on a template by proteins capable of self-assembling in solution.

RAD51 nucleation is highly selective

Next, we investigated the mechanism leading to selective filament formation. Previous studies comparing RAD51 affinity for ssDNA or dsDNA present some incongruities. In gel-mobility shift experiments RAD51 displayed higher affinity for dsDNA[105], whilst in another study ssDNA was the preferred substrate [149]. Magnetic-tweezers experiments have resulted in contradicting models, in which RAD51 does not display substrate specificity [169] or binds faster to ssDNA [109]. Here, we directly quantified RAD51 nucleation and growth rates on single ssDNA and dsDNA molecules. We detected two striking differences in the DNA-binding kinetics of RAD51: (i) nucleation is highly substrate selective, favouring ssDNA over dsDNA; (ii) nucleation rate is independent of tension on ssDNA, while it increases exponentially with tension on dsDNA. In the case

of dsDNA, RAD51 filament formation requires a substantial amount of lengthening and therefore is energetically costly. The assisting load tilts the energy landscape of RAD51 nucleation and growth on dsDNA, decreasing template selectivity in the high force regimes. Quantitatively, the application of force on dsDNA corresponds to lowering the energy barrier for nucleation and growth up to $\sim$7 k_BT and $\sim$4 k_BT respectively, at the maximum force dsDNA can sustain (65 pN). These values, in turn, represent a lower limit for the actual energy barriers for binding dsDNA in a relaxed conformation.

Implications for in vivo homologous recombination

The strong intrinsic preference of RAD51 for ssDNA uncovered by our findings represents a simple yet powerful means of targeting the recombinase towards its physiological nucleic-acid substrate and limiting non-productive binding to dsDNA. Recent findings suggest a novel role for RAD51, independent of homologous recombination, in coating regions of ssDNA that form at replication forks in normal or stressed conditions [68, 146]. Our observation that RAD51 possesses an intrinsic affinity for ssDNA provides a physical basis for this novel biological role of RAD51. Recombination mediators such as BRCA2 and RAD51 paralogues have been often implicated to overcome the alleged lack of binding preference by directing RAD51 specifically to ssDNA [27, 151, 83, 165, 28]. Our observation that RAD51 has a strong intrinsic preference for filament formation on ssDNA indicates that BRCA2 might be less important in regulating RAD51 substrate specificity. Indeed, using both single-molecule and ensemble kinetic measurements we found that BRC4 domain of BRCA2 acts as an inhibitor of RAD51-filament formation in a concentration-dependent way. Hence, the role of BRCA2 might be restricted in promoting filament formation by displacing RPA from ssDNA [83, 98] and/or regulating ATP hydrolysis and stabilizing RAD51 filaments [28]. These putative roles of BRCA2 can now be tested, in our experimental setup, by observing directly the impact of recombinase mediators such as BRCA2 on RAD51-filament formation. Moreover, another class of mediators including Srs2, RTEL1 and RecQ5 helicases, can be investigated at the single-molecule level, in order to obtain a full picture of the regulation of RAD51-filament formation.

Our sm-FRAP approach allowed us to quantify RAD51-filament growth on both ssDNA and dsDNA. Past attempts to discriminate between nucleation and growth was hindered by experimental limitations, since the accessible experimental readout, the coverage fraction in magnetic-tweezers

Cooperativity of RAD51 filament formation and comparison with RecA

assays, represents an average behaviour of the RAD51 binding reaction. Cooperativity is a fundamental property of the RAD51-filament formation process, determining the final size and structure of the filaments. Separate detection of filament growth permitted us to measure for the first time RAD51 cooperativity. We found that the rate of RAD51 growth is $\sim$3 (ssDNA) and $\sim$5 (dsDNA) orders of magnitude larger than the nucleation. These results confirm that nucleation is a rate-limiting step of filament formation and, as such, could represent an important regulatory step during HR. A recent single-molecule study indicated that the RecA filament formation on SSB-coated ssDNA [12] is highly cooperative (cooperativity was determined to be on the order of 10^7, considering a growth rate of 30 monomer min^{-1} and a nucleation rate of $2x10^{-6}$ nt^{-1} min^{-1} at 200 nM of RecA). Whether this high value for the cooperativity stems from the intrinsic binding kinetics of RecA on ssDNA or from the inhibitory effect of SSB on the nucleation step of RecA is not clear. The striking difference between the reported cooperativity values for RecA and RAD51 (approximately 4 orders of magnitude) might indicate that RAD51-filament growth is rate-limiting during filament formation, thus requiring the intervention of recombinase mediators at this critical step of recombinational repair. To conclude, the experimental approaches developed in this study elucidated the mechanism and regulation of the crucial homologous recombination process and, in addition, provide a demonstration that single-molecule methods can now visualize directly and precisely multi-protein interactions at single-monomer resolution on individual ssDNA molecules.

A STOCHASTIC MODELLING OF FILAMENT FORMATION

We here set up a minimal model coupling RAD51 filament association/dissociation to/from, a single DNA molecule.

A.1 FILAMENT–DNA BINDING DYNAMICS IN THE LOW COVERAGE REGIME

The total coverage of the DNA molecule remains very low throughout the experiments, and we can ignore the possibility of existing filament blocking the binding of new filaments. If we let p(n,t) to be the probability that a binding position contains the left end of a filament of length n at time t, the corresponding Master equation for each binding site reads

$$\frac{\partial p\left(n,t\right)}{\partial t} = -k_{off} p\left(n,t\right) + k_{on}\left(n\right) \tag{3}$$

Here, $k_{off}\left(n\right)$ is the rate at which a filament of length n dissociates from the DNA strand, and $k_{on}\left(n\right)$ is the rate at which filaments of length n attach to a binding position from solution. Solving the Master equation we have:

$$p\left(n,t\right) = \frac{k_{on}(n)}{k_{off}\left(n\right)}\left(1 - e^{-tk_{off}(n)}\right) \tag{4}$$

For times and filament lengths such that $tk_{off}\left(n\right) \ll 1$, few filaments that have attached to the DNA have also had time to fall off, and the occupation probability grows linearly with time $p\left(n,t\right) = tk_{on}\left(n\right)$. If instead times and filament lengths are such that $tk_{off}\left(n\right) \gg 1$, the filaments on the DNA have had time to equilibrate with the buffer, and we have the time-independent distribution $p\left(n,t\right) = k_{on}\left(n\right)/k_{off}\left(n\right)$.

A.2 EQUILIBRIUM DISTRIBUTION OF FILAMENTS IN SOLUTION

We now assume that RAD51 proteins can form linear filaments in solution, with a constant interaction energy gained for every protein-protein association. These filaments are continuously formed and broken up by thermal forces in equilibrium. For the concentration of filaments of length n+m, $[RAD51_{n+m}]$, to be equilibrated with the concentrations $[RAD51_n]$ and $[RAD51_m]$, the law of mass action dictates that $[RAD51_{n+m}] = \alpha [RAD51_n] [RAD51_m]$. Here α is the association constant between filament ends, and the resulting exponential distribution of filaments is $[RAD51_n] = (\alpha [RAD51])^n / \alpha$. If we use that the total concentration of protein is $[RAD51] = \sum n [RAD51_n]$, we can rewrite the filament concentrations as:

$$[RAD51_n] = 4 [RAD51] sinh^2 (-n\epsilon_{sol}/k_B T) \tag{5}$$

$$\epsilon_{sol} = k_B T \ln \left(\frac{2\alpha [RAD51]}{1 + 2\alpha - \sqrt{1 + 4\alpha [RAD51]}} \right) \tag{6}$$

A.3 ASSOCIATION AND DISSOCIATION RATES BETWEEN DNA AND RAD51 FILAMENTS

We take the on-rate of filaments of length n to be directly proportional to the filament concentration in the buffer, and write $k_{on}(n) = k_{on} e^{-n\epsilon_{sol}/k_B T}$. We further assume each RAD51 molecule in a filament contributes a fixed amount ϵ_{DNA} to the dissociation barrier from DNA, giving $k_{off}(n) = k_{off} e^{-n\epsilon_{DNA}/k_B T}$. This defines the model in terms of two rate constants (k_{on} and k_{off}) and two energy scales (ϵ_{sol} and ϵ_{DNA}) with direct physical interpretations.

For any given time t, the maximum filament length that has had time to equilibrate with the buffer is $n^*(t) \approx (k_B T/\epsilon_{DNA}) \ln \left(t k_{off} \right)$. Interestingly, if $\epsilon_{DNA} > \epsilon_{sol}$ the nuclei length distribution on the DNA is peaked somewhere around $n^*(t)$, resulting in a typical nucleus size that shifts logarithmically with the time since incubation.

A.4 NUCLEATION RATE AND THE APPARENT HILL COEFFICIENT

The apparent nucleation rate of filaments measured in the experiment only accounts for the filaments that remain bound at the end of the incubation. In terms of our model, this is given by

$$k_{on}^{app} = \sum_{n=1}^{\infty} p\left(n, t\right) / t_{inc} \tag{7}$$

The actual total on-rate is inferred from our model parameters as:

$$k_{on}^{true} = \sum_{n=1}^{\infty} k_{on} e^{-n\epsilon_{sol}/k_B T} = \frac{k_{on}}{e^{\epsilon_{sol}/k_B T} - 1} \tag{8}$$

If we estimate the model parameters for any one known concentration, we can predict the filament distribution at any other concentration. Of special interest is the apparent Hill coefficient, since it has previously been used as a measure of the (assumed) degree of cooperative binding. We are working in the low-coverage regime—well before any saturation effects become important—and therefore define the concentration dependent apparent Hill coefficients as the derivative:

$$n_{Hill}^{app} = \left([RAD51]\right) = [RAD51] \frac{d \ln k_{on}^{app}\left([RAD51]\right)}{d\,[RAD51]} \tag{9}$$

This is the local slope in a log-log-diagram of the apparent binding rate (or nucleation rate) vs. concentration.

A.5 MAXIMUM LIKELIHOOD FITTING OF FLUOROPHORE DISTRIBUTION

We here fit our proposed model to the data using Maximum likelihood methods, yielding both estimators for the parameters themselves and the errors.

We are faced with the additional problem that the number of fluorophores f, is not unique on each monomer, but distributed according to, say, $q\left(f\right)$.The

observed number of fluorophores f in a fiber of n monomers is then distributed according to

$$q_m(f) = \sum_{f_1,\ldots,f_m}^{\infty} q(f_1)\, q(f_2) \ldots q(f_m)\, \delta_{f,\sum_{n=1}^{m} f_n} = (q*)^m(f) \tag{10}$$

Here δ is the Kronecker delta function. Letting $\theta = \left\{k_{on}, k_{off}, \epsilon_{sol}, \epsilon_{DNA}\right\}$, the probability of finding f flourophores attached to a filament starting at any particular position is given by

$$P(f,t \mid \theta) = \sum_{m=1}^{\infty} q_m(f)\, p(m,t \mid \theta) \tag{11}$$

In our system the only non-zero fluorophore probabilities are $q(1) = 3/4$ and $q(2) = 1/4$.

A.6 FITTING THE FLUOROPHORE DISTRIBUTION

To fit the model to our data, we utilized a maximum-likelihood scheme. The fit is generated by maximizing the likelihood of the observed fluorescence of the DNA molecules, given our model

$$L\left(\theta \mid \left\{N_f\right\}_{f=0}^{\infty}\right) = exp\left(-\sum_{f=0}^{\infty} N_f \ln P(f, t_{inc} \mid \theta)\right) \tag{12}$$

Here $t_{inc} = 70s$ is the incubation time, and $N_f$is the number of filaments observed with f flourophores. The total number of binding sites exposed during all experiments are $N_0 = N_{DNA}N_{Exp}$, where $N_{DNA}$is the number of binding sites per tether and N_{Exp} is the number of experiments. To estimate the model parameters we numerically minimize $-\ln N\left(\theta \mid \left\{N_f\right\}_{f=0}^{\infty}\right)$with respect to them. To estimate the error in the fit parameters, we perform the fit on 1000 bootstrapped data sets. We report the best fit of the original data, together with the standard deviation in the fit parameters as calculated over the bootstrapped data set:

$$k_{on} = 10^{-4.7\pm0.8} nt^{-1}s^{-1} \tag{13}$$

$$k_{off} = 10^{1.5\pm0.8} s^{-1} \tag{14}$$

$$\epsilon_{sol} = (1.1 \pm 0.3)\, k_B T \tag{15}$$

$$\epsilon_{DNA} = (1.8 \pm 0.5)\, k_B T \tag{16}$$

The fit of our model to the measured data set is presented in Figure 2B, and indicates that the average RAD51 oligomer size in solution was $n_{sol} = 1/\left(1 - e^{-\epsilon_{sol}/k_B T}\right)$ monomers—in good agreement with chemical cross-linking experiments performed in a similar concentration range (Supplementary Figure 3). From the fit parameters we calculated the association constant between RAD51 filaments by using our expression for ϵ_{sol}. The experiments were performed at [RAD51]=12.5 nM, giving $\alpha = 0.060 \pm 0.036/nM$. With this we have estimates for all the microscopic parameters.

Apparent vs. true nucleation rate The apparent total nucleation rate in the experiments is the number of observed nuclei divided by the total number of bases incubated across experiments, and then further divided by the incubation time, giving $k_{on}^{tot*} = 3.7 \times 10^{-7} nt^{-1} s^{-1}$. From above we know that the true total on-rate is given by:

$$k_{on}^{tot} = \frac{k_{on}}{e^{\epsilon_{sol}} - 1} \approx 1.1 \times 10^{-5} nt^{-1} s^{-1} \tag{17}$$

A.7 APPARENT HILL COEFFICIENT

Since we have estimates for all the microscopic parameters, we can make predictions regarding the expected dynamics at any concentration. The apparent Hill-coefficient calculated in the concentration range around [RAD51]=12.5 nM is 2.0. The average Hill coefficient in the concentration range used in our experiment is 1.6.

B SUPPLEMENTARY FIGURES

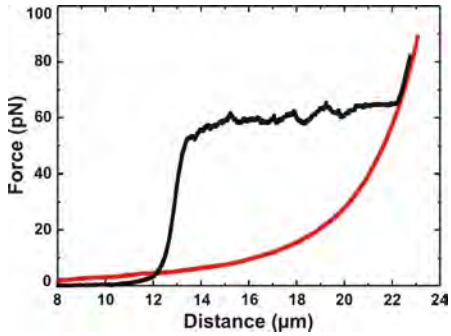

Figure S38.: Force-induced melting of dsDNA was employed to produce ssDNA templates. Force-stretching curve of a 38412 bp dsDNA(Black line). The molecule was pulled beyond the overstretching plateau (F>85 pN). The force-stretching curve (red line) confirmed the generation of a single ssDNA molecule tethered between the beads.

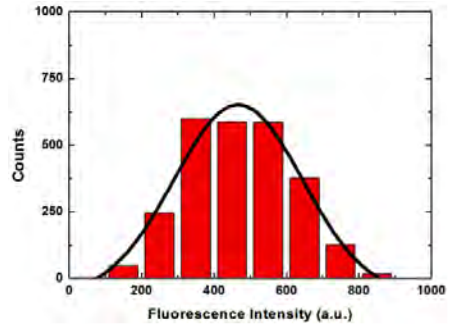

Figure S39.: DNA-protein complexes can absorb onto polystyrene beads. [A] Force distance curve of a naked DNA molecule (black) and after incubation with XRCC4-XLF (red). In the red curve a force rise and drop is detected, resembling the rupture of an intra-molecular bridge. [B] Fluorescent visualization during bead separation reveals the unspecific absorption of DNA-protein complexes onto the polystyrene bead.

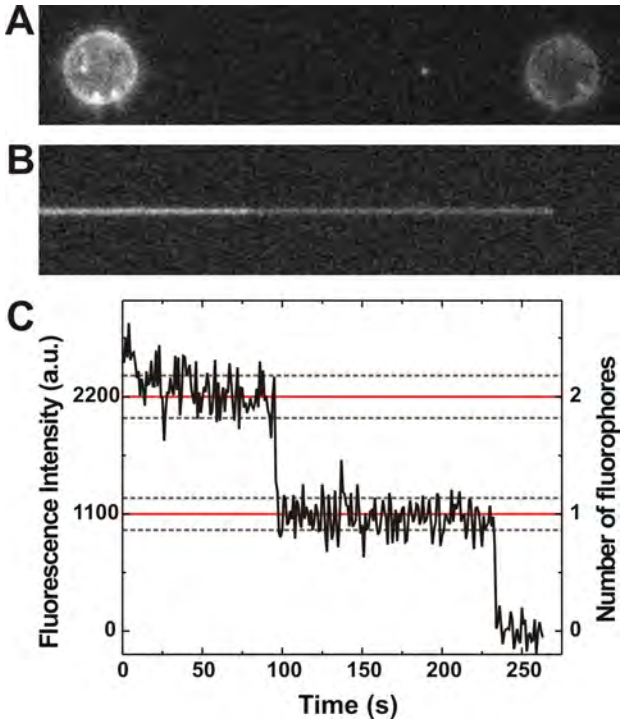

Figure S40.: RAD51 nucleus on ssDNA. Example of stable RAD51 nucleus on ssDNA composed of 2 fluorophores. [A] Fluorescent snapshot of an individual ssDNA molecule kept at 40 pN after a 70 seconds incubation in the enzyme channel containing 12.5 nM of RAD51. [B] Kymograph. [C] Fluorescence intensity shows staircase pattern. Two bleaching events can be easily recognized. In this experiment we set the camera exposure to 1000 ms and we increased the laser excitation for obtaining high S/N. The presence of two steps in the photo-bleaching trace indicates that the RAD51 nucleus was composed of two monomers, each labelled with one Alexa555 dye. Alternatively there is the possibility that we observed the presence of a single RAD51 monomers labelled with two Alexa555 dyes.

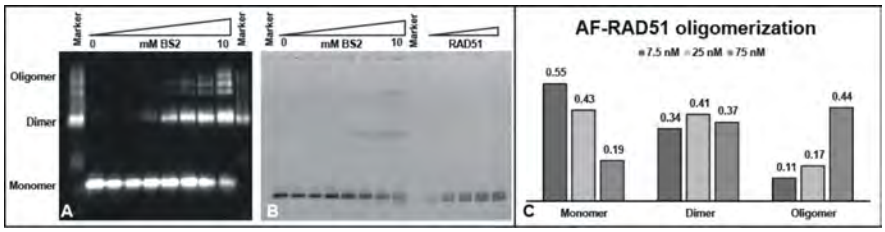

Figure S41.: Alexa-RAD51 cross-linking in solution with BS2. The cross-linked complexes were resolved by polyacrylamide gel electrophoresis. Detection of Alexa-RAD51 by anti-RAD51 Western blot [A] and typhoon scan of the Alexa fluorescence signal [B] show that with increasing cross-linker concentration more defined multimeric species of RAD51 are cross-linked. The example shows cross-linking at 75 nM RAD51. [C] The percentage of different forms of RAD51 determined from densitometry scanning of protein cross-linked at 7.5 nM, 25 nM and 75 nM RAD51 and run on SDS-PAGE.

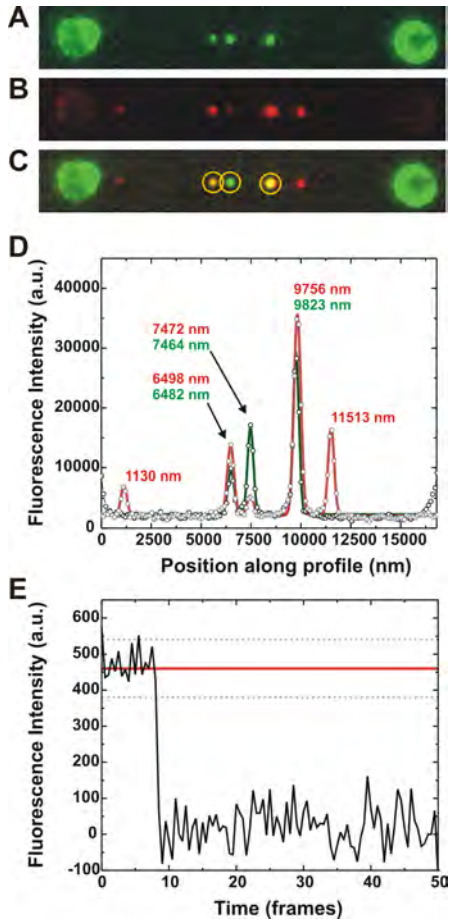

Figure S42.: RAD51 growth on dsDNA [A] Averaged fluorescence image of λ-DNA molecule (48502 bp, length 16.4 μm) held at 40 pN after incubation with 75 nM RAD51 for 70 seconds. After visualization, continuous exposure resulted in complete photo-bleaching of all the fluorescent spots (data not shown). [B] Averaged fluorescent image of the same dsDNA molecule, re-incubated with RAD51 for a second cycle of 70 seconds. [C] Overlaying figure A and B allows distinguishing between growth and new nucleation events. In the yellow circles are example of patch co-localization. [D] A line profile over a region along the dsDNA is plotted. We found that in two cases the co-localization of the patches was with sub-20 nanometers precision. [E] A photo-bleaching trace of the fluorescent spot at position 7472nm detected in the second incubation cycle (growth event) shows one individual step in agreement with our single-molecule fluorescence calibration and demonstrates in a direct way that extension of RAD51 can take place in form of individual RAD51 monomers.

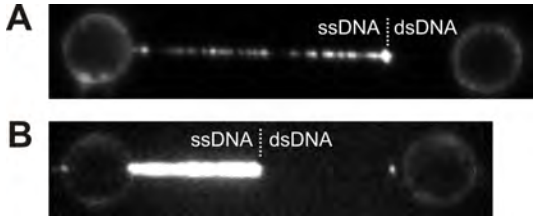

Figure S43.: Hybrid ss-ds DNA constructs reveal structural specificity of human RAD51. RAD51 filament formation rate is affected by the DNA structure. To generate the hybrid templates a λ-DNA molecule was held at 22 μm at 65 pN for 60 seconds. When single nicks are present on the unlabelled strand of the DNA, a hybrid ss-dsDNA structure can be generated. Force-distance curves were taken to verify and quantify the extent of the ssDNA and dsDNA region. The incubation time in both cases was 60 seconds and the RAD51 concentration was 75 nM. [A] Experiment in 20 mM Tris pH 7.6, 100 mM KCl, 1 mM $CaCl_2$, 0.5 mM ATP, 10 mM DTT. [B] Experiment in 20 mM Tris pH 7.6, 10 mM MgOAc, 2 mM $CaCl_2$, 1 mM ATP, 10 mM DTT.

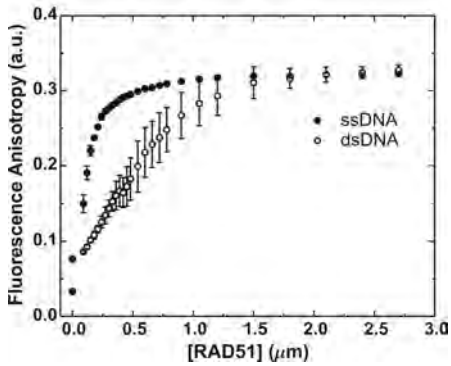

Figure S44.: Fluorescence polarization anisotropy measurement on RAD51 selectivity. Fluorescence anisotropy measurements of RAD51 binding to fluorescein labelled ssDNA (black filled circles) and to dsDNA (white filled circles). The ssDNA was a 60-nucleotide long DNA sequence. The dsDNA was constructed by annealing the fluorescein – labelled ssDNA with its complementary strand. A concentration series of RAD51 in binding buffer was titrated into wells using the PHERAstar FS built-in injectors. Binding was initiated by injecting fluorescein labelled DNA (10 nM final) and measurements were taken after 10 minutes with 200 flashes. The data points represent the average of three independent experiments (error bars = 1SD).

6 DYNAMICS OF RAD51 FILAMENTS

DYNAMICS OF RAD51 NUCLEOPROTEIN FILAMENTS ON SSDNA IS REGULATED BY ATP HYDROLYSIS AND AFFECTED BY RAD51 RESIDUE 313

The maintenance of chromosome integrity depends critically upon the accurate repair of double-stranded DNA breaks. Homologous recombination is a conserved DNA repair pathway, able to restore chromosome integrity without loss of genetic information. The human RAD51 protein is the core catalyst of homologous recombination, forming filaments on single-stranded DNA and performing the strand-exchange reaction.

Here we combined optical trapping and fluorescence microscopy to unveil the dynamic properties of individual RAD51-ssDNA filaments. We compared two naturally occurring isoforms of RAD51, K313 and Q313, and found that the alteration of a single amino acid results in dramatically different behavior of the RAD51 nuclei: RAD51-Q313 nuclei are static, and the time they remain bound to the ssDNA relates to their size. RAD51-K313 nuclei, on the other hand, can slide and hop along the ssDNA. In addition, we show that the diffusion of RAD51-K313 nuclei depends on their size: larger nuclei often bind without moving along the DNA, while RAD51 monomers predominantly display diffusive motion.

Next, we observed that RAD51-ssDNA filaments are profoundly susceptible to applied tension: filaments can occur in a compressed and an extended conformation. When ATP is bound, filaments are in the extended conformation, while in the ADP state the RAD51 conformation depends on tension: at forces above 9 pN filaments are extended and below they are compressed. Using Jarzynski's equality we revealed the free energy difference between these two conformations is approximately 4 kB_T.

Revealing the impact of a single amino acid as well as the exquisite force balance of the filament conformations demonstrates the multi-faceted and finely balanced nature of RAD51 protein, the key player of human homologous recombination.

6.1 INTRODUCTION

Homologous recombination and RAD51 nucleoprotein filament

Homologous recombination (HR) is a multi-step process able to repair endogenous and exogenous DNA double-stranded breaks (DSB). After occurrence and detection of a DSB, the broken DNA ends are processed by the end-resection machinery and 3' single-stranded DNA (ssDNA) overhangs is created [142, 76]. Subsequently, RAD51, the central catalyst of HR, forms right-handed helical filaments around these overhangs, commonly referred to as the nucleoprotein filament (NPF). The NPF is able to search for and pair with the homologous sequence in the sister chromatid in order to exchange genetic information between the DNA molecules [14].

Structure and function of RAD51 nucleoprotein filament

In vitro, the formation of the NPF can occur in presence of both ATP [174] and ADP [72]. The resulting filaments, however, display very different properties. Electron microscopy studies have revealed that human RAD51 bound to ssDNA in the presence of ATP adopts an extended conformation with a pitch of 9.8 nm [190]. The ADP-bound filament is more compact, with a pitch of approximately 8 nm and is often referred to as the compressed conformation [190]. These two states not only have distinct structural properties but also differ in terms of biochemical function: ATP-bound-extended RAD51 is able to perform strand exchange with high efficiency, while ADP-bound-compressed-RAD51 is less active, and might represent an intermediate state before disassembly [23]. X-ray crystallography identified the location of the ATP-binding pocket between adjacent monomers in the filament [38]. The monomer-monomer interface of the RAD51 filament is therefore crucial for the correct execution of homologous recombination.

RAD51 isoforms: K313 vs Q313

Interestingly, two sequences of human RAD51 (D14134.1 and D13804.1) are deposited, differing in the amino acid at the position 313, which could be either a Lysine (K313) or a Glutamine (Q313). Presumably both variants occur among the human population. Within the RAD51 nucleoprotein filament, the residue 313 lies in the proximity of the monomer-monomer interface [81] and therefore could significantly affect the behaviour of RAD51 protein. Biochemical studies proposed that this mutation regulates RAD51 strand-exchange activity through a mechanism involving a differential filament-forming ability [81].

Structural studies provided hints that the recombinase filament is a dynamic entity, able to transition between these conformations in response to nucleotide hydrolysis. The interplay between ATP hydrolysis, structural transitions and disassembly of recombinase proteins was further verified at the single-molecule level. It was demonstrated that RAD51- filaments on dsDNA can undergo multiple transitions between the extended and the compressed state without dissociating, implying that this transition is dictated by nucleotide present at the monomer-monomer interface [136]. Also, it has been revealed that high levels of tension applied on the DNA can stall the filament disassembly process (F>50 pN), possibly by a mechanism in which the above mentioned conformational transition is halted [174]. In addition force has been shown to switch the conformation of bacterial RecA filaments on dsDNA from the compressed to the extended state [37]. So far, a characterization of these dynamic transitions of RAD51 nucleoprotein filaments on ssDNA is lacking.

Structural tranistions and interplay with ATP hydrolysis

Role of DNA tension on RAD51 structure

Here, we have combined dual-optical trapping, single-molecule fluorescence microscopy, force-induced DNA melting and micro-fluidics [176, 174, 59, 25] to simultaneously control and manipulate a long ssDNA molecule while visualizing fluorescently labelled RAD51 bound to it. Our method allowed studying how the applied tension on the DNA affects the physical structure of the RAD51 nucleoprotein filament. We found that forces exceeding 9 pN are able to induce the elongation of ADP-bound RAD51 from the compressed the extended conformation. Furthermore we quantified the free-energy difference between these two structural forms, providing novel insights on the plasticity of the RAD51 recombinase filament. Next, we visualized the interaction of two naturally occurring variants of RAD51, RAD51-K313 and RAD51-Q313 on ssDNA. Our results reveal that the interaction with ssDNA of K313-RAD51 and Q313-RAD51 are substantially different. K313-RAD51 interacts with ssDNA by both sliding along ssDNA and hopping between different sites. Q313-RAD51, on the other hand, forms filaments that are static.

6.2 MATERIALS & METHODS

6.2.1 RAD51 fluorescent labeling

RAD51 (C319S) fluorescent labelling was performed as previously described [114]. Further biochemical characterization showed that ATP hydrolysis, efficiency in joint molecule formation and DNA binding properties were indistinguishable from wtRAD51.

6.2.2 Preparation of DNA construct

To produce a 48.512 nt ssDNA melting Lambda DNA was biotinylated at the 3′ and 5′ end of the same strand using three oligonucleotides. First, the 5′-end of Lambda DNA and oligonucleotide 1 (5′- ggg cgg cga cct gga caa-3′) and 2 (5′- agg tcg ccg ccc ttt ttt tTt TtT-3′) were phosphorylated for 30 min at 37°C in a reaction containing 14 nM Lambda DNA or 10 μM of the oligonucleotide and 0.25 U/μl of T4 Polynucleotide Kinase in 1x T4 Ligase buffer (Fermentas). Next, oligonucleotides 1 and 3 (5′- TtT tTt ttt ttt aga gta ctg tac gat cta gca tca atc ttg tcc-3′) were annealed to the overhangs of Lambda DNA in a 10:1 oligonucleotide: DNA ratio (total volume 500 μl) by heating the reaction to 65°C and slowly cooling down to room temperature. The ligation reaction was then initiated by adding T4 DNA ligase (0.02 U/μl) and carried out for two hours. Next, oligonucleotide 2 was annealed in a 100:1 ratio to the Lambda DNA construct by incubation at 45°C for 30 minutes. Subsequently, the oligonucleotide was ligated to the DNA at room temperature. Finally, the DNA was purified by ethanol precipitation.

6.2.3 Experimental Conditions

Experiments were performed in 20 mM Tris-HCl pH 7.5, 100 mM KCl, 1 mM $CaCl_2$, 10 mM DTT, unless otherwise specified.

6.3 RESULTS

6.3.1 Single-Molecule assay for studying RAD51 on DNA

Our approach, consisting of combining dual optical tweezers, single-molecule fluorescence microscopy and micro-fluidics has been described extensively in previous publications [176, 174, 59, 25].

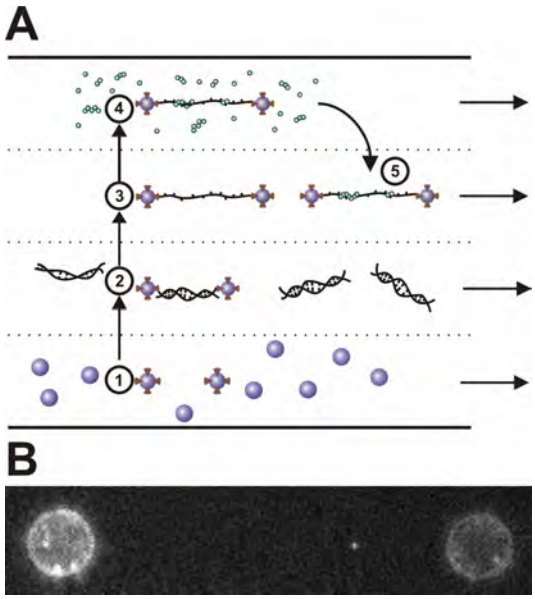

Figure 45.: Single-molecule experimental approach for studying of the mechanical and dynamic properties of RAD51 nucleoprotein filaments. [A] Microfluidics is used for the in situ assembly of the single-molecule assay and the fluorescence visualization in the absence of fluorescent background. The experiment is composed of 5 steps: (i) capture two beads in the optical traps. (ii) Tethering of a single dsDNA molecule between the beads. (iii) force-induced melting and production of a long ssDNA tether. (iv) ssDNA is exposed to the buffer containing fluorescent RAD51 for a defined amount of time. (v) the ssDNA-RAD51 complex is imaged in the absence of fluorescence protein in solution. [B] Example of an individual RAD51 nucleoprotein filament resolved on a single ssDNA molecules held in an extended configuration by dual optical tweezers.

In brief, dual-trap optical tweezers are used to trap streptavidin-coated beads Figure 45.A (4.26 μm diameter – Spherotech). Using a computer-controlled microscope stage and a micro-fluidics system, an individual

double-stranded DNA molecule (dsDNA) can be tethered between the beads. Applying tensions above 80 pN, force-melting can be triggered [173, 60]. Following this method, an intact ssDNA molecule is produced. Next, the ssDNA molecule is exposed to a buffer containing a fluorescent variant of human RAD51 labelled at a specific cysteine residue (RAD51-Q313-C319S-Alexa555 which we refer to as RAD51-Q313 or RAD51-K313-C319S-Alexa555, which we refer to as RAD51-K313) in the presence of ATP and Mg^{2+} or Ca^{2+}. After incubation (for 1 to 5 minutes), the ssDNA molecule is removed from the RAD51-containing buffer and repositioned in the imaging channel. Successful formation of RAD51-nucleoprotein filaments is verified using fluorescence microscopy in absence of RAD51 in solution (Figure 45.B).

6.3.2 RAD51 residue 313 affects the dynamic properties of nucleoprotein filaments on ssDNA

To test whether RAD51-K313 and RAD51-Q313 differ in their interaction with ssDNA, we directly visualized individual nucleoprotein filaments on ssDNA in the presence of ATP-Ca^{2+} and ATP-Mg^{2+}. When ATP hydrolysis is prohibited [23] (in the presence of Ca^{2+}), RAD51-Q313 forms static nucleoprotein filaments on ssDNA, as previously reported [114, 174].

RAD51-Q313 filaments are static. RAD51-K313 filaments are dynamic

Figure 46.A shows an example of a kymograph in which multiple static nucleoprotein filaments formed by RAD51-Q313 are detected on a single ssDNA molecule. RAD51-Q313 forms nucleoprotein filaments whose stability is dictated by their size (see Chapter 5). The decrease in fluorescence intensity in Figure 46.A follows a typical staircase pattern of single-molecule photobleaching traces, indicating that not the interaction time with the ssDNA but photobleaching limits the time RAD51-filaments can be observed under these conditions. In contrast to RAD51-Q313's static binding to ssDNA, we found that RAD51-K313 is able to diffuse along the ssDNA showing signatures of both sliding and hopping. The kymograph in Figure 46.B indicates the presence of several RAD51-K313 filaments.

We notice that some filaments are able to display longitudinal motion (see patch "a" in Figure 46.B) while others appear static (see patch "b" in Figure 46.B). We therefore can exclude that the longitudinal displacement observed for these RAD51-K313 filaments are due to the ssDNA thermal fluctuations.

RAD51-K313 hopping on ssDNA

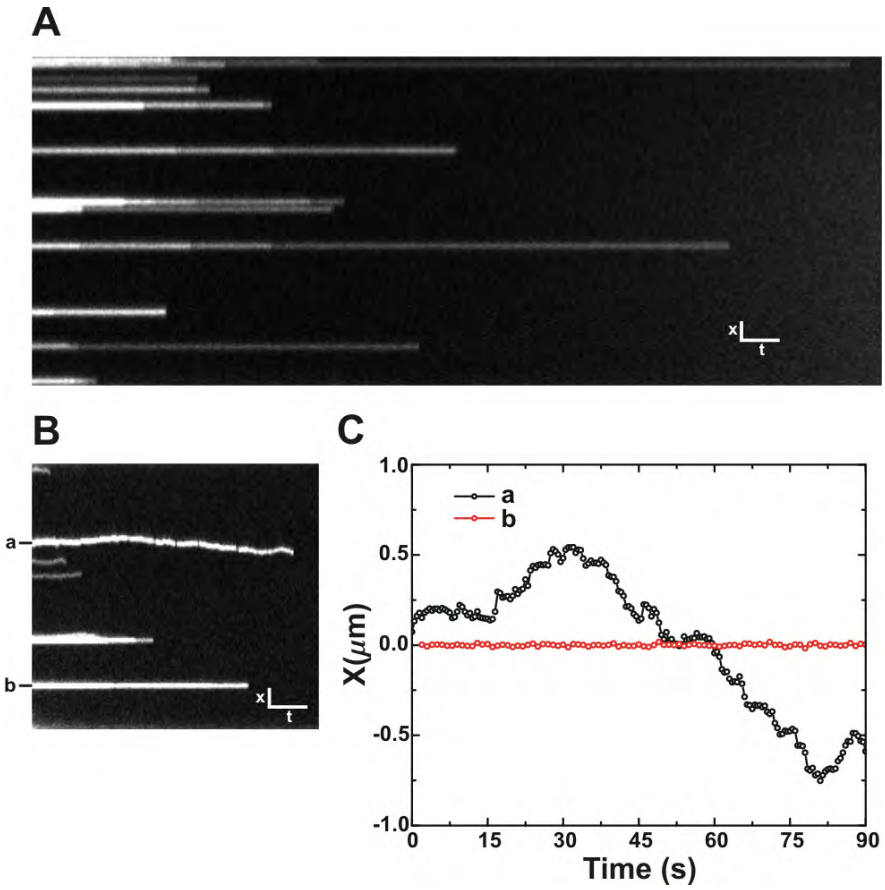

Figure 46.: Dynamic properties of RAD51 filaments on ssDNA. [A] Kymograph showing static RAD51-Q313 filaments in the presence of ATP-Ca^{2+}. [B] Kymograph showing RAD51-K313 filaments in the presence of ATP-Ca^{2+}. Most of the nucleoprotein filaments diffuse along the ssDNA (see patch a). Some filaments show no sign of displacement (see patch b). [C] Time-trajectory of single RAD51-K313 nucleoprotein filaments "a" and "b".

Remarkably, the fluorescent spots in in Figure 46.B disappear suddenly between consecutive frames, independently of their initial fluorescence intensity (see patch "a' and "b" in 46.B). This indicates that also RAD51-K313 nuclei are able to spontaneously release into solution from the ssDNA, similarly to RAD51-Q313. Kymographs were analysed using single-particle tracking [25] (see Figure 46.C).

Determination of diffusion coefficients

The diffusion coefficient of individual RAD51 filaments was determined by linear fitting of the mean-squared-displacements as a function of the time-lag. We restricted our analysis to RAD51 filaments that stayed bound on the DNA for at least 10 frames (N=270 in $MgCl_2$ and N=170 in $CaCl_2$) and obtained a diffusion coefficient of $(1.7\pm0.2)\times10^{-3}$ $\mu m^2/s$ in the case of Mg^{2+} and $(2.2\pm0.2)\times10^{-3}$ $\mu m^2/s$ in the presence of Ca^{2+} (mean$\pm$SE). In our experiment, we found that not all of the K313-RAD51 filaments show diffusive behaviour, but a fraction between 50 to 60%, according to the divalent cation present in the buffer (see Figure 47.A).

RAD51-K313: interplay between filament size and diffusive behavior

Furthermore, we noticed that the dynamic properties of bright and dim RAD51 patches tend to differ: bright patches are mostly static while dimmer ones diffuse more frequently. To further quantify this, we determined the fraction of diffusing filaments as a function of fluorescence intensity. To this end, we estimated the lowest diffusion coefficient detectable under our experimental conditions to be 2×10^{-5} $\mu m^2/s$ (based on the localization accuracy ($\sim$20 nm) and the average interaction time of the RAD51 filament in Mg^{2+}, approximately 10 to 20 seconds for small filaments). This lowest detectable diffusion constant was used as a threshold for classifying particles as diffusive or static. The histogram of the fraction of diffusive particles as a function of fluorescence intensity (Figure 47.B) indeed shows that brighter (larger) filaments have a higher probability to be statically bound to the ssDNA.

In addition to the reported diffusive behaviour, we found that in rare cases (approximately 5% of the diffusive filaments) RAD51-K313 nucleoprotein filaments exhibit displacements over micrometres within consecutive frames (see Figure 48.A and Figure 48.B). We attribute this behaviour to the release and the re-association of the filament to a different location (hopping). It is very unlikely that such large displacements are due to translocation while remaining bound to the ssDNA, considering the very low diffusivity of RAD51. In addition, Figure 48.C shows an example in which a static RAD51 filament (patch a) is located in between the unbinding and rebinding locations of another, hopping one (patch b). Considering the helical structure of RAD51 filaments, it is very unlikely that a purely sliding mechanism is responsible for the observed filament bypass. Therefore we conclude that RAD51-K313 diffusion occurs through a combination of both size-dependent sliding and hopping.

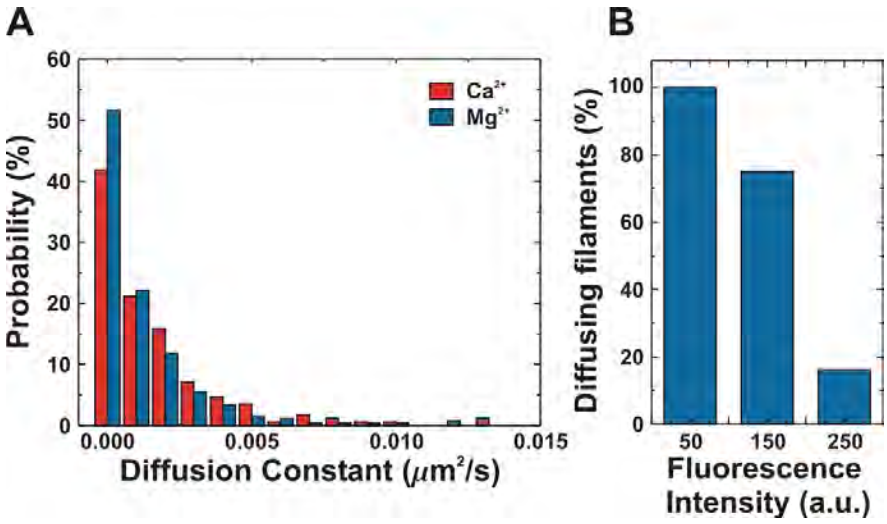

Figure 47.: Diffusion of K313-RAD51. [A] Distribution of diffusion coefficients for RAD51- K313 in Ca^{2+} (red columns, N=170) and Mg^{2+} (blue columns, N=270). [B] Histogram showing the relationship between the fluorescence intensity (size) of RAD51-K313 nucleoprotein filaments and the probability to display diffusive behaviour.

6.3.3 Disassembly of RAD51 nucleoprotein filaments shows pausing-burst behavior

Next, we studied ATP-hydrolysis-induced disassembly of individual RAD51 filaments from ssDNA. It has been shown before that RAD51 disassembly from dsDNA proceeds in bursts from filament ends, limited by ATP-hydrolysis of the terminal monomer [174]. To test whether the mechanism of disassembly from ssDNA is similar, fluorescent RAD51 (K313 and Q313) filaments were assembled on ssDNA in the presence of Mg^{2+} and the disassembly was subsequently monitored in real time in the presence of Mg^{2+}, but absence of fluorescent RAD51 in solution (Figure 49.A). Measurement conditions were optimized to minimize photo bleaching, while retaining single-fluorophore sensitivity. To determine the disassembly kinetics, kymographs were analysed (Figure 49.B) and fluorescence intensity traces were obtained (Figure 49.C).

RAD51 disassembles in burst starting from filament ends

Similarly to disassembly from dsDNA, disassembly from ssDNA occurs in bursts involving multiple RAD51 monomers, separated by pauses (Figure 49.C). We found that pause durations are exponentially distributed,

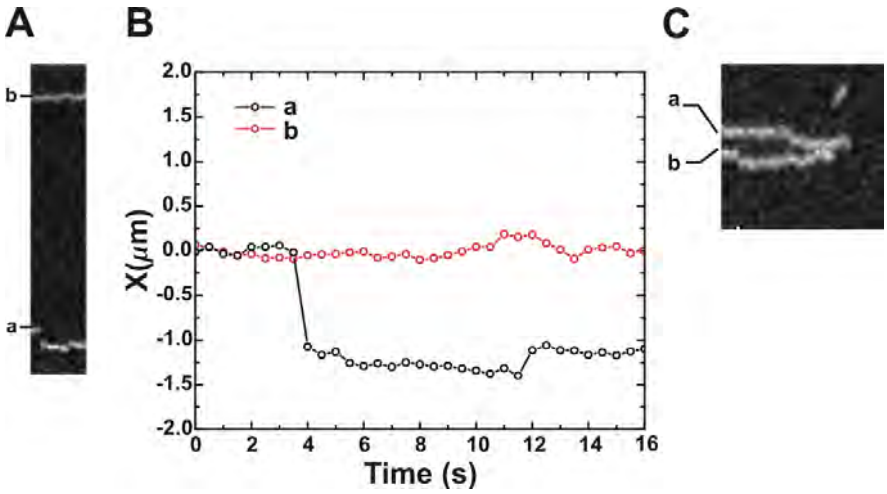

Figure 48.: Detection of hopping of K313-RAD51. [A] Example of kymograph of RAD51-K313 in the presence of ATP-Ca^{2+} showing signature of both hopping (see patch "a") and sliding (see patch "b"). [B] Single-particle tracking of the kymograph in panel A. Patch (a), changes position of approximately 1 μm within two consecutive frames (3.5s-4.0s). Patch (b) shows a purely diffusive behaviour. [C] Hopping of a RAD51 filament (patch b) allows bypassing a second filament bound to the ssDNA (patch a).

on average lasting 55±5 seconds (Figure 49.D). This value is substantially shorter than the value determined for RAD51-filament disassembly from dsDNA (150±10 seconds) [174], which is in accordance with the three-fold higher ATP-hydrolysis rate observed for RAD51 in the presence of ssDNA compared to dsDNA [166].

Our data further support the notion that RAD51 disassembles from filament ends. In addition, we observed that under conditions permitting ATP hydrolysis, Q313-RAD51 is also able to diffuse along the ssDNA (Figure 49.D). This occurs only in a small fraction of the filaments (∼6.5%) and always in the last phase of its interaction with ssDNA, just prior to release into solution.

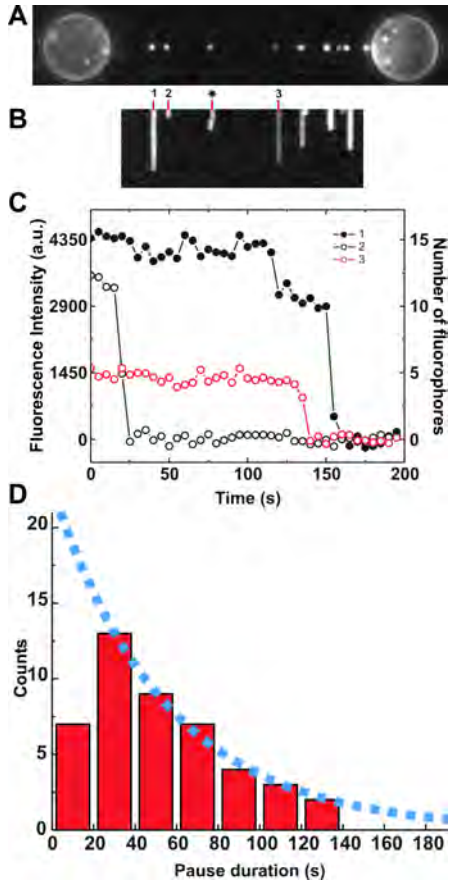

Figure 49.: RAD51-Q313 disassembly kinetic. [A] Fluorescence image showing an ssDNA construct immediately after incubation with RAD51-Q313 in solution, in the presence of ATP and Mg^{2+}, conditions that allowed ATP hydrolysis. [B] Kymograph showing ATP-hydrolysis-induced disassembly. Asterisk denotes a RAD51 nucleus that moves, prior to disassembly. We found that approximately 6.5% of RAD51-Q313 moves during disassembly. [C] Fluorescence intensity time traces of RAD51 filaments 1, 2 and 3 of kymograph B show that disassembly occurred in bursts separated by pauses. [D] Red columns represent the pause duration histogram (pauses below 20s cannot be detected experimentally). The blue dotted line is the exponential fit to the distribution indicating a mean pause duration of 55±5 seconds.

6.3.4 Nucleoprotein-filament elasticity during ATP hydrolysis

Next, we try to resolve the mechanical response of RAD51-filaments on ssDNA to tension in the presence of ATP hydrolysis and absence of free RAD51 in solution.

RAD51-ssDNA nucleoprotein filament elasticity

To this end, we densely coated ssDNA with fluorescent RAD51 (RAD51-K313) using a buffer (20 mM Tris pH 7.5, 10 mM $Mg(OAc)_2$, 2 mM $CaCl_2$, 2 mM ATP, 1 mM DTT) in which RAD51 is active for strand exchange and ATP hydrolysis and retains its interactions with recombinase mediators [27]. After incubation, the extent of RAD51 coverage of the ssDNA was checked using fluorescence visualization (see Figure 51.A). Subsequently, force-distance curves were recorded by consecutive stretching and relaxing the ssDNA molecule at a constant rate of 670 nm/s (see Figure 50).

RAD51-coated ssDNA molecule shows hysteretic force-extension behaviour

The first remarkable observation is that both stretch and relax curves of RAD51-coated ssDNA are different from the force-curves of naked ssDNA. This indicates that the stretching (relaxation) of RAD51-ssDNA filament is more complex than the entropic extension (relaxation) of a polymer chain. A second, even more striking observation, is that (in contrast to naked ssDNA) stretching and relaxation curves do not overlay in the regime of 15 to 28 μm extension. In other words, the RAD51-coated ssDNA molecule shows hysteretic force-extension behaviour. Such hysteretic behaviour has been reported before for RecA [69]. However, two interpretations were put forward to interpret that observation: (i) the recombinase filaments bound to ssDNA are able to switch between a compact and extended conformation in response to the applied tension or (ii) extension of the ssDNA can stimulate RecA binding to the interstitial sites between filaments.

Hysteretic force-extension behaviour is due to a conformational transition

To confirm that the hysteresis is caused by a force-induced conformational transition, we recorded fluorescence images before and after the extension and relaxation of the ssDNA (see Figure 51.A and Figure 51.B). The images show no appreciable difference in fluorescence intensity, indicating that the difference between the two curves is not due to force-induce detachment of RAD51. Also, our microfluidic approach permits to exclude the presence of residual recombinase proteins in solution during the force-extension cycle. Therefore we can exclude both RAD51 binding and unbinding as a possible reason of the observed hysteresis.

ADP-bound RAD51 is able to undergo a force-induced structural transition

We assume that at low force, all ADP-bound recombinase proteins are in their natural compact form. Consistently with previously published data, we assume also that ATP-bound RAD51 retains the extended conformation independently of the force applied [175]. A possible explanation of the observed lengthening is that during DNA stretching, the ADP-bound RAD51 is able to undergo a force-induced structural transition and switch to a new state, which resembles the extended conformation. In the force-

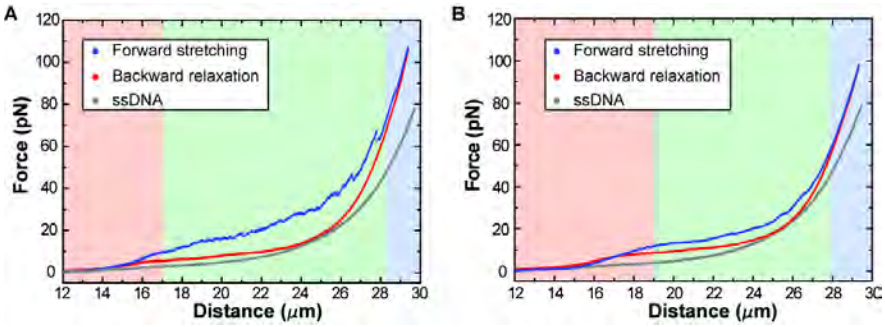

Figure 50.: Nucleoprotein-filament elasticity during ATP hydrolysis. Force-distance curves of ssDNA covered with RAD51 in ATP hydrolysis condition and absence of RAD51. [A] ssDNA-RAD51 complex is stretched (blue curve - forward extension) until 110 pN and back to low end-to-end distance (12 μm) at the loading rate of 670 nm/s. Initially (red) we observe an entropic and an enthalpic phase. In the second phase (green), a force-induced conformational transition occurs. In the third phase (blue), when high forces are reached (F>100pN) the saw-teeth behaviour cease to exist and a unique conformation is present. The reference curve for ssDNA is plotted in grey. The backward relaxation is plotted in red. [B] A second ssDNA-RAD51 complex is stretched at 100 nm/s. The reference curve for ssDNA is plotted in grey. In red, green and blue the three different elastic regimes.

extension experiments, the conformational switching of the recombinase proteins occurs in non-equilibrium, resulting in the observed hysteresis. By decreasing the extension rate, one would expect the system to stay closer to equilibrium, resulting in a lower degree of hysteresis. Indeed, upon decreasing the extension rate from 670 nm/s to 100 nm/s (see Figure 50.B), the hysteresis in the force-extension curves of RAD51-coated ssDNA is significantly lower. By independently monitoring the fluorescence intensity, we found that it decreases as a function of time (see Figure 51.C), due to ATP-hydrolysis induced detachment of RAD51 from the ssDNA.

We quantified the disassembly kinetics and found a rate constant of 0.047 ± 0.01 min^{-1}, negligible during a single stretch-relax cycle ($\sim$1 minute). This indicates that the hysteresis between subsequent stretching and relaxation curves is not due to ATP-hydrolysis induced detachment of RAD51 from ssDNA, but intrinsic to the RAD51-coated DNA, confirming the existence of a force-induced molecular transition of the ADP-bound RAD51 from a compressed to an extended structure.

Time-dependent hysteretic force-extension curves

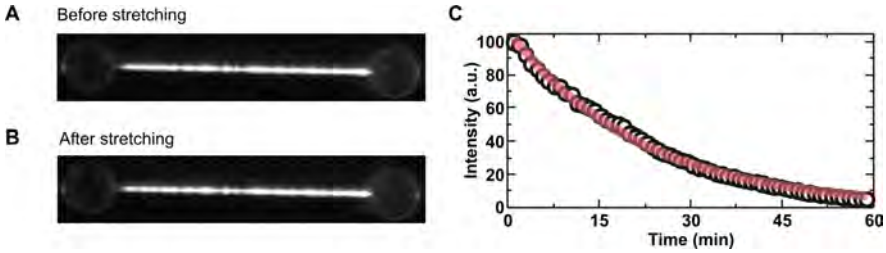

Figure 51.: RAD51 filament disassembly kinetic. Characterization of RAD51 filament disassembly kinetic using single-molecule fluorescence microscopy. [A] Image an ssDNA molecule covered with fluorescent RAD51 before the stretching cycle. [B] Image of single ssDNA molecule covered with fluorescent RAD51 after the stretching cycle. [C] Fluorescence intensity as a function of time shows that disassembly of RAD51 can be characterized by an exponential decay using 0.047 ± 0.01 min^{-1} as RAD51 disassembly rate.

To test how ATP hydrolysis and RAD51 detachment affects these hysteretic force-extension curves of RAD51-coated ssDNA, we repeatedly recorded cycles of stretch and relax force-extension curves, over a time scale of an hour. We noticed that over the course of several minutes, both stretch and relax force-extension curves dramatically changed (see Figure 52). The contour length of the DNA-protein complex, indicated approximately by the end-to-end distance at which the sudden force increase occur during the stretching (indicated by the circles in Figure 52), shifts, over time, to lower extension. We hypothesized that this shift is caused by the hydrolysis of ATP to ADP. We therefore quantified the hysteresis, calculating the area between subsequent stretches and relax curves as a function of time (see Figure 52). Note that in a force-extension curve, the area corresponds to work. The hysteresis area as a function of time shows biphasic behaviour: first the hysteresis area increases with time, until it reaches a maximum and decreases to zero.

Physical model of time-dependent hysteresis

We modelled this behaviour using the following model: (i) ATP-RAD51 bound to ssDNA can occur in only one form, the extended conformation; (ii) ADP-RAD51 bound to ssDNA, can be either in this extended or in a compact form, depending on the tension applied; (iii) only ADP-bound RAD51 is able to detach from ssDNA. Our model consists of two coupled differential equations describing the time evolution of the system, involv-

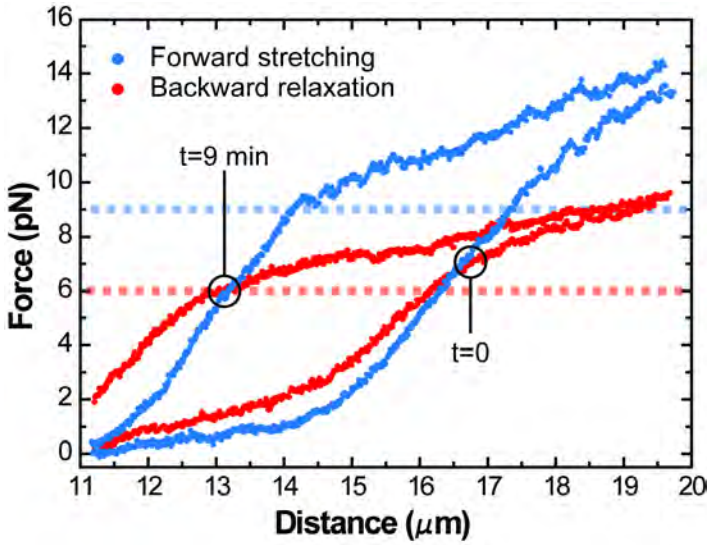

Figure 52.: Effect of ATP hydrolysis on force-distance curves of RAD51-ssDNA complexes. Inset of consecutive forward (blue) and backward stretching cycles (red). During the forward stretching we observe the presence of both an entropic and enthalpic behaviour up until the force of 9 pN. Above the force-threshold of 9 pN (blue dotted line) a saw-tooth behaviour is observed, suggesting the presence of a molecular transition. During the backward stretching cycle we observed that the reverse transition occur below the force of 6 pN (red dotted line). The cross-point between forward and backward stretching for consecutive cycles moves progressively towards shorter extensions..

ing the hydrolysis of ATP by ssDNA-bound RAD51 with rate k_{hyd} and subsequent detachment of RAD51 from the ssDNA with rate k_{off}:

$$\frac{dN_{ATP}(t)}{dt} = -N_{ATP}(t)\, k_{hyd} \tag{18}$$

$$\frac{dN_{ADP}(t)}{dt} = N_{ATP}(t)\, k_{hyd} - N_{ADP}(t)\, k_{off} \tag{19}$$

These coupled equations can be solved and compared to the time-dependence of the area of hysteresis as:

$$\Delta W(t) = \mathrm{Y} e^{-tk_{off}} \left(\chi_{ADP} + \frac{\chi_{ATP} k_{hyd} \left(-1 + e^{-t\left(k_{off} - k_{hyd}\right)} \right)}{k_{off} - k_{hyd}} \right) \tag{20}$$

where Y represents the conversion factor between the number of ADP-bound monomers and the hysteresis area, $\chi_{ADP/ATP}$ the fraction of ATP/ADP-bound RAD51 molecules in the beginning of the experiment. Our experimental results can be well fitted by this equation, resulting in an initial increase of the hysteresis due to the ATP-to-ADP conversion, a maximum value of the hysteresis and a subsequent exponential decay due to detachment of RAD51 form the ssDNA after ATP hydrolysis. Using a fixed value of k_{off} of 0.05 min^{-1} (see Figure 51.C) we obtain fitting values of Γ of $(60\pm1)\times10^3$ k_BT/molecule, and X_{ATP} of 0.68±0.03 and k_{hyd} of 0.12±0.01 min^{-1}. The quality of the fits indicates that the hysteretic force-extension behaviour is caused by force-induced switching of ADP-RAD51 from a compact to an extended form upon increasing tension on the ssDNA and vice versa (see Figure 53).

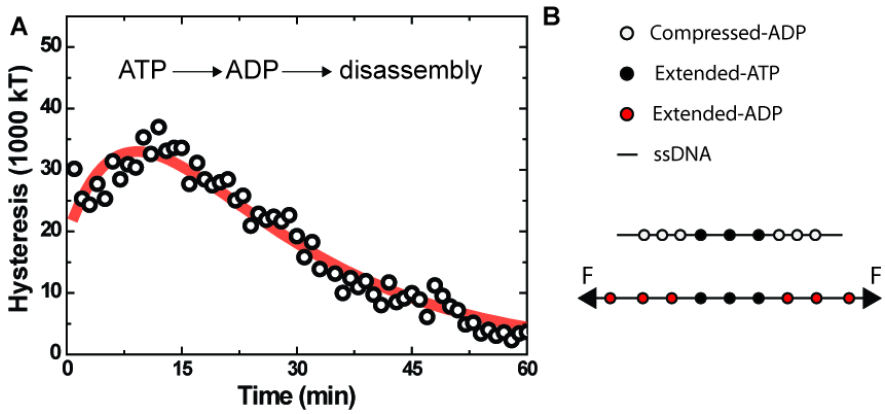

Figure 53.: **Hysteresis in successive F-D cycles computed from experimental data.** [A] The computed difference in the work performed during consecutive forward and backward stretching cycles $\Delta W = W_{forward} - W_{backward}$ is plotted as a function of time. The time dependence is due to the ATP hydrolysis and disassembly of RAD51. Under the assumption that only the ADP-bound RAD51 undergoes a non-equilibrium molecular transition we fitted the experimental curve with equation xyz. [B] Schematic representation of the force-induced conformational change. Upon application of force above 9 pN the natural compressed ADP form (white circles) undergoes a molecular transition to a new state (red circles) whose physical structure resembles the extended-ATP bound conformation (black circle).

6.4 DISCUSSION

6.4.1 RAD51 filament dynamics

The interface between RAD51 monomers within the nucleoprotein filament, of which RAD51 residue 313 is part, is crucial for homologous recombination, since it regulates both the structure and the biochemical function of the filament. It has been shown that two naturally occurring variants of RAD51, differing only with respect to the nature of residue 313 have distinct filament-formation and strand-exchange efficiencies [81].

Functional differences between K313 and Q313

Here, we report another difference between these variants using a combination of single-DNA molecule manipulation and single-protein visualization experiments. Q313-RAD51 shows a size-dependent lifetime on the DNA, as previously described (see Chapter 5). Only under conditions permitting ATP hydrolysis, Q313-RAD51 diffuses along the ssDNA, in a small fraction of the filaments (6.5%) and always in the last phase of its interaction with ssDNA, just prior to release into solution. K313-RAD51 behaves quite differently: monomers and dimers interact with ssDNA through a combination of sliding and hopping, showing considerable motility also under conditions inhibiting ATP-hydrolysis (Ca^{2+}-ATP). Filaments composed of more than three K313-RAD51 monomers are significantly more stable and form ssDNA-protein complexes that do not move along the DNA. A recent linear dichroism study has shown that DNA bases in RAD51-ssDNA filaments are less ordered when ATP hydrolysis can take place [54], indicating that the ADP-bound RAD51 interacts less strongly with ssDNA. Based on these observations, we speculate that this weakly bound-state is also able to slide along the ssDNA.

Possible role of diffusion in RAD51 filament assembly

Recombinase proteins such as RecA [172] and RAD51 (see Chapter 5) form filaments on ssDNA with high cooperativity and starting from multimeric units. Such an assembly mechanism results in incomplete coverage of the ssDNA substrate, as demonstrated using Monte-Carlo modeling and magnetic tweezers measurements [172]. A possible strategy allowing the formation of continuous filaments over μm-long segments of ssDNA would involve the redistribution of pre-bound proteins [90, 172]. Proposed possible mechanisms included that individual monomers could translocate between filament ends either via unidirectional motion, diffusion or hop-

ping [172]. Here we have shown that small nucleoprotein structures can translocate along ssDNA over significant distances (>100 nts).

Structural properties of RAD51-ssDNA filaments

Next, we investigated the structural properties of RAD51-ssDNA filaments under ATP-hydrolysis conditions. Electron micrographs studies have proposed that the RAD51-ssDNA filaments are characterized by a high degree of conformational freedom. The variety of structural forms reported for human RAD51 are likely due to a rotational movement of the N-terminal domain which can locally modify the contact between the filament and the ssDNA [190]. Multiple conformations therefore are possible, reflecting the intrinsic flexibility of the RAD51 nucleoprotein filament.

Role of force in defining the structure of RAD51-ssDNA filaments

To what extent do the ssDNA conformation and the thermal fluctuations influence the geometry of the human RAD51 nucleoprotein filament? Using force spectroscopy measurements we observed that the ssDNA conformation and the structure of the nucleoprotein filament are intimately related. Applying forces above 9 pN induces a structural transition in the RAD51-ADP-bound filament between a compressed to an extended conformation, resulting in an elongation of the filament. We used two different extension velocities (670 and 100 nm/s) and found that in both cases force-extension curves recorded in the stretching and relaxation directions are not equal: the system shows hysteresis. This indicates that the system is not in equilibrium during the force-extension experiments. Thus, the work performed on the system does not provide a good estimate of the free energy difference between the two RAD51 conformations. The equilibrium free energy difference between these conformation can, nevertheless, be recovered using the Jarzynski's equality [82]: $\left\langle e^{-W/k_BT} \right\rangle = e^{-\Delta G/k_BT}$. Since the number of ADP-bound molecules changes during our measurement due to ATP hydrolysis and RAD51 dissociation, we used a moving average obtained from 5 consecutive force-distance curves and compare the computed free energy with the expected coverage of the ssDNA molecule. We found, in the limit of initial coverage higher that 60% of the ssDNA molecule, a weak dependence of the expected value of ΔG, which is estimated in the range of 4.7 k_BT (for an estimated initial coverage of 70%) to 3.3 k_BT (for the completely saturated case). i.e. the energy required to extend ADP-bound RAD51 on ssDNA is approximately 4 k_BT of energy.

6.4.2 Implications for strand exchange

What is the structure of the RAD51 recombinase filament in vivo? RAD51 binds on ssDNA in the presence of ATP. While dissociation of ADP-bound RAD51 monomers can occur only from filament ends [84, 174], ATP hydrolysis can occur anywhere within the RAD51 filament. Therefore, when ATP-hydrolysis is permitted (when Mg^{2+} is present), the structure of the recombinase filament is likely heterogeneous, alternating segments in the ATP-bound and ADP-bound states, as confirmed by the force distance curves reported in Figure 49. In the canonical view of homologous recombination, only the ATP-bound extended conformation is active for strand exchange. Recent structural data on the bacterial homolog of RAD51 (RecA) have shown that ATP hydrolysis induces a dramatic conformational change which affects the interaction network between the recombinase protein and the ssDNA [33]. This conformational change is responsible for the inactivation of the filament for strand exchange. The question how the strand exchange reaction proceeds in the presence of a mixture of ADP and ATP nucleotides remain, therefore, unchallenged. A possibility is that such hybrid structures never occur in vivo, either because ATP molecules from solution can replace the ADP bound at the monomer-monomer interface [136], or because the conformational transition is blocked by the action of recombinase mediators, such as the tumour suppressor protein BRCA2 [49].

Filament plasticity is conserved through evolution and we argue that constitutes a key ingredient for understanding strand exchange. Our work demonstrated that a work input of approximately 3 to 4 k_BT is sufficient to induce a conformational transition from the compressed to the extended state of RAD51. This amount is considerably lower than the energy required for the chemical synthesis of an ATP molecule ($\sim$20 k_BT).

Role of filament plasticity in strand exchange

In the presence of thermal fluctuations, therefore, we expect that a small fraction (approximately 3% when ΔG=3.5 k_BT) of RAD51 proteins are in the active state for initiating the strand exchange reaction, irrespective if ATP or ADP is bound at the monomer-monomer interface. Also, if strand-exchange is initiated, the energetic penalty required to convert a RAD51 protein from the inactive to the active state may be supplied by the base-pairing energy and the interaction between the secondary binding site of the filament and the displaced ssDNA strand [103, 104]. This ADP-specific

energetic penalty therefore leads to more stringent homology requirements for stable pairing compared to the ATP-bound RAD51 case. Our results indicate a possible strategy for RAD51 to execute strand exchange even in the presence of locally ADP-bound RAD51 and explain the role of RAD51 filament's plasticity in determining the selectivity of the homology recognition process. Future single-molecule experiments will aim at elucidating how the applied tension modulates not only the physical properties but also the biochemical function of individual RAD51 filaments.

7 NON-HOMOLOGOUS END JOINING

SLIDING, PAUSING AND BRIDGING: HOW HUMAN XRCC4 AND XLF INTERACT WITH DNA

Non-Homologous End Joining (NHEJ) is an efficient mechanism to repair DNA double-strand breaks. XRCC4 and XLF are two structurally-similar core NHEJ proteins. They can directly interact at the protein-protein level and engage DNA by an unknown mechanism.

Here, we use optical tweezers and fluorescence microscopy to visualize XRCC4-XLF complexes on DNA in real time. We find that the behavior of XRCC4-XLF on DNA is multifaceted: complexes rearrange continuously and show periods of rapid diffusion along the DNA, interspersed by stationary binding. By manipulating two DNA molecules independently we study bridge formation and demonstrate that XRCC4-XLF complexes can directly bridge two independent DNA molecules.

Our approach reveals the transient and dynamic aspects of the interaction of XRCC4-XLF with DNA providing new insights on how they could function during DNA double-strand break repair by NHEJ.

7.1 INTRODUCTION

DNA damage and repair

The maintenance of chromosome integrity depends critically upon the repair of double-stranded DNA breaks (DSB). Failure to efficiently execute DNA repair may result in chromosomal aberrations such as genomic translocations, a hallmark in human cancers [73, 65]. Two major DBS repair processes exist in humans: homologous recombination (HR) and non-homologous end-joining (NHEJ). While HR requires an homologous template to copy and restore the genetic information at the damaged site [142], NHEJ operates by direct religation of the two broken DNA ends [95]. Cells presenting malfunctions in genes associated with the NHEJ repair pathway display hypersensitivity to ionizing radiations [3] and severe immunodeficiency-syndromes [73].

Non-Homologous End Joining (NHEJ)

The principal components of the NHEJ DNA repair consist of Ku70/80 [95], DNA-PKcs [152], XRCC4 [85], XLF [4, 94] and DNA Ligase IV (LigIV) [153]. Although how these proteins assemble and operate during NHEJ is still under research, two major steps have been identified: (i) Ku70/80 first recognizes the ends of the broken DNA molecules and recruits DNA-PKcs [95] and (ii) a complex of XRCC4-Lig IV ligates the broken ends together [95], stimulated by XLF [3]. XRCC4 and XLF display similar structural properties [4, 85], since both form homo-dimers characterized by N-terminal heads and alpha-helical tails. Recent X-ray crystallographic studies have indicated that XRCC4 and XLF are binding partners, forming long, helical filaments with a pitch of 72 to 84 nm and a large internal groove with a diameter of approximately 10 nm [64, 137, 182, 5]. In addition, the alpha-helical tails of XRCC4 show two intriguing features: they are involved in the formation of XRCC4 tetramers through a tail-to-tail interaction [85], and they serve as a binding platform for the C-terminal domain of LigIV (BRCT) [153].

Role of XRCC4 and XLF in NHEJ

Resolving how XRCC4 and XLF interact with DNA and what functions they execute during NHEJ are challenging research problems. Two contradicting DNA binding strategies have been proposed: in one, the XRCC4-XLF helical filament binds around the DNA [5], while in the other model is the DNA to wrap around the XRCC4-XLF protein complex [64]. Also, the exact role of XRCC4 and XLF in NHEJ is currently under debate. In the canonical view of NHEJ, XRCC4 and XLF intervene late during the repair process, stimulating the ligation step catalysed by LigIV [182]. In a recent

biochemical study it has been shown that XRCC4 and XLF are also present at the early stage of NHEJ, displaying a LigIV-independent function [141]. Also, recent bulk and AFM methods have shown hints that XRCC4 and XLF possess the capability of forming bridges between DNA molecules [5]. The possibility that XRCC4-XLF complexes are capable of holding together two DNA molecules is particularly intriguing, since it can provide a molecular explanation to the reported stimulatory role in the DNA ligation step [5] as well as their early function during NHEJ [141].

In order to provide a better understanding of the biochemical and biophysical properties of the XRCC4-XLF complex, we have generated a fluorescently labelled variant of XRCC4 with biochemical activity unaltered from wild-type. In experiments combining DNA manipulation via optical tweezers and protein visualization via single-molecule fluorescence microscopy we studied the DNA-binding properties of XRCC4 in the absence and presence of its binding partner XLF in real-time. In addition, we tested the DNA-bridging properties of XRCC4-XLF complexes in a novel assay involving the manipulation of two DNA molecules. Our results show that the DNA binding properties of XRCC4-XLF are complex, involving switching between fast diffusion along the DNA and static binding. Finally we demonstrate the ability of XRCC4-XLF to form bridges between DNA molecules.

7.2 MATERIALS & METHODS

7.2.1 Protein expression, labeling and biochemical activity

Fluorescently labelled XRCC4 was prepared by the "Cys light" method [111]. Plasmid pBMM42 [112], a pET28a derivative expressing recombinant human XRCC4 tagged with polyhistidine at the C-terminus was modified by site directed mutagenesis to remove all Cys codons but one. Constructs XRCC4-41 (C93A C128A C130A C165A) and XRCC4-43 (C128A C130A C165A C218A) were generated and verified by DNA sequencing. Recombinant XRCC4 proteins were purified after expression in bacteria as described [112]. AlexaFluor 555-maleimide (Invitrogen) was used for specific labelling at position C218 (XRCC4-41) and C93 (XRCC4-43), respectively. Proteins were first buffer exchanged into 50 mM Tris pH 7.2,

300 mM KCl, 1 mM EDTA and 10% glycerol, adjusted to 2 mg/ml and labelled with AlexaFluor 555-maleimide (Invitrogen) at 5:1 dye-to-protein molar ratio for 2 hours at 4°C. Reactions were quenched by addition of fresh DTT (10 mM) and excess dye was removed by size exclusion chromatography (Econo-Pac 10DG columns, BIO-RAD) followed by Sepharose Q chromatography. Preparations were finally dialyzed against 20 mM HEPES pH 8, 150 mM KCl, 1 mM EDTA, 1 mM DTT and 10% glycerol and stored at -80°C. Functionality of the fluorescently labelled XRCC4 preparations were tested for DNA and LigIV tandem BRCT domains interaction by electromobility shift assays as described [5] and behaved as the unlabelled wild type protein. Recombinant wild-type human XLF was produced as described [4]. The XLF expression construct was modified by inserting an eGFP-His6 cassette at the C-term. The fusion protein was purified using the same protocol as for the wild-type protein. Wild-type XLF and XLF-eGFP were stored at -80°C in 20 mM HEPES pH 8, 150 mM KCl, 1 mM EDTA, 1 mM DTT and 10% glycerol. Functionality of the fluorescently labelled XLF preparations were tested for DNA and XRCC4 binding, for DNA bridging and for LigIV/XRCC4 stimulation as described [5] In these assays XLF-eGFP behaved like the wild-type unlabelled control except that it was deficient in the DNA bridging assay.

7.2.2 Single-molecule approach

The biophysical properties of XRCC4 and XRCC4-XLF complexes on DNA were studied at the single-molecule level using a combination of DNA manipulation and fluorescence visualization. Our technique permits the manipulation of a single Λ-DNA molecule between two optically trapped microspheres (4.5 μm in diameter) and the control over the applied tension with 0.1 pN accuracy [25, 59]. The single-molecule construct was assembled in situ using a microfluidic system and a computer-controlled movable microscope stage. Fluorescent XRCC4 (XRCC4-Alexa555) and wild-type XLF were introduced in the flow-cell in a separate channel using laminar-flow, in order to minimize mixing with the other components. The DNA molecule was allowed to interact with a high concentration (in the range of 50 to 400 nM) of the fluorescent proteins for a defined amount of time (between 30 seconds to 5 minutes). Following this incubation step, the DNA-protein complex was repositioned in the imaging channel, in the ab-

sence of fluorescent protein in solution. This step permits single-molecule fluorescence resolution. To study the DNA bridging properties of XRCC4-XLF complexes, a novel instrument was developed which combines dual DNA manipulation [42] and fluorescence visualization. Using this instrument it was possible to manipulate independently two distinct DNA molecules and produce a crossed configuration where the two molecules are held in contact. DNAs kept in this configuration were incubated with XRCC4-Alexa555 and XLF. The specificity of the binding and the formation of inter-molecular bridges were tested using both direct imaging and the force response of the DNA-protein complex.

7.2.3 Buffer conditions

Protein-DNA interaction and force-stretching experiments were conducted in 20 mM Tris-HCl pH 7.5 and variable concentrations of monovalent ions, in the range of 25 to 150 mM KCl and 1 mM DTT. Beads catching and DNA tethering were performed instead in phosphate buffered saline (PBS-Sigma).

7.2.4 Fluorescence tracking and diffusion analysis

The fluorescent movies were analysed in the following way: first, the intensity in the direction longitudinal to the DNA was averaged over 5 pixels to produce a kymograph. The kymograph was further analysed using a custom written Labview routine. A one-dimensional Gaussian fitting was performed and the x-position of the fluorescent protein along the DNA was recorded. For a time trace of N point, the mean-squared-displacement at time lag n was calculated according to:

$$MSD\,(n,N) = \frac{\sum_{i=1}^{N-n}\left(x_{i+n}-x_i\right)^2}{N-n} = 2Dn\Delta t + \sigma_{loc}^2 \tag{21}$$

The statistical variance of MSD(n,N), as demonstrated by [129, 179, 88] was computed using the following expression:

$$\sigma_{n,N}^2 = \frac{(2Dn\Delta t)^2\left(2n^2+1\right)^2}{[3n\,(N-n+1)]} \tag{22}$$

Where Δt is the exposure time of the camera (typically from 50 to 100 ms). From each diffusion trajectory (with N_{frames}>50) the diffusion constant D was obtained using a weighted linear fit of MSD(n,N) in the interval from n=1 to n=5.

7.3 RESULTS

7.3.1 XLF stimulates the binding of XRCC4 to DNA

We first addressed the DNA binding properties of XRCC4 and XLF using a combination of optical tweezers and fluorescence microscopy. In order to study the interaction of XRCC4 and XLF with DNA, it is important to understand how their DNA binding affinity is affected by their relative stoichiometry.

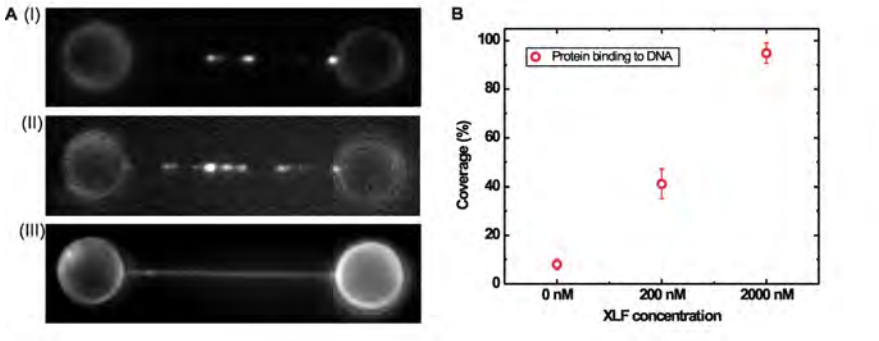

Figure 54.: XLF stimulates binding of XRCC4 on DNA. [A] Single DNA molecule observed after an incubation step of three minutes in a buffer containing: (i) 200 nM of XRCC4-Alexa555; (ii) a premixed solution with XRCC4-Alexa555 and XLF (200 nM:200 nM); (iii) 200 nM XRCC4-Alexa555 and 2 μM XLF. All measurements are performed in a buffer solution containing 20 mM Tris-HCl pH 7.5, 25 mM KCl and 1 mM DTT. [B] DNA coverage (measured as the fraction of stained and unstained DNA) as a function of XLF concentration (XRCC4-Alexa555 concentration was 200 nM).

Role of XLF in the formation of XRCC4-XLF protein complexes on DNA

To this end, we investigated how increasing concentrations of XLF modulate the formation of XRCC4-XLF complexes on DNA. For this experiment we used a single cysteine mutant of XRCC4 labelled with the fluorophore Alexa555 (XRCC4-Alexa555) and wild-type unlabelled XLF. The

DNA molecule was held at a defined tension (in the range from 1 to 30 pN) using dual optical tweezers and subsequently incubated in the channel containing the mixture of XRCC4 and XLF (for an incubation time of 3 minutes) and visualized using fluorescence in the imaging channel devoid of fluorescent proteins. After incubation with XRCC4-Alexa555 alone, many fluorescent spots of differing intensity were bound on the DNA molecule (Figure 54.A). Incubation with XRCC4 at the same concentration in the presence of an equal concentration of XLF resulted in enhanced protein binding and DNA coverage. Adding XLF in large excess (10:1, XLF:XRCC4) resulted in a complete and homogeneous coverage of the DNA, almost instantaneous on the time-scale of our experiments. Our results thus indicate that XLF stimulates the binding of XRCC4 to DNA in a concentration-dependent manner (Figure 54.B). The head-to-head interaction between XRCC4 and XLF involves both hydrophobic contacts and hydrogen bonds and is crucial for filament formation, as highlighted by mutational analysis [64]. Therefore we tested the effect of increasing salt concentration on the DNA binding properties of XRCC4 and XLF. Increasing the KCl concentration from 25 mM to 150 mM resulted in a drastic inhibition of filament formation on DNA (Figure 55). Paradoxically, at salt concentrations close to the physiological range (approximately 150 mM) the formation of filament on DNA is practically entirely suppressed. This indicates the fundamental role of electrostatic interactions in the formation of a XRCC4-XLF-DNA complex.

XRCC4 is present in solution as a homo-dimer but can from higher-order structures [112, 113]. The sparse and bright fluorescent spots observed after incubation with XRCC4-Alexa555 alone indicates that binding to DNA of XRCC4 oligomers [85] is slow and inefficient. When XLF is added to the XRCC4-Alexa555 reservoir, protein complexes containing both XRCC4 and XLF are formed in solution [182]. Because large excess of XLF strongly stimulates XRCC4-Alexa555 binding to DNA (Figure 54.C), we presume that the interaction between the DNA with a solution containing XRCC4 and XLF in equal amount will result predominantly in the formation of XRCC4-XLF complexes and not in XRCC4-alone binding to the DNA. In most of the experiments that are going to be discussed below, we used a 1:1 ratio of XRCC4-Alexa555 and XLF. We therefore refer to the fluorescent patches obtained following this protocol as XRCC4-XLF complexes. Furthermore, we verify that using equal amount of XRCC4 and XLF results

in XRCC4-XLF complex formation on DNA using multi-color fluorescence imaging (Supplementary Figure S71).

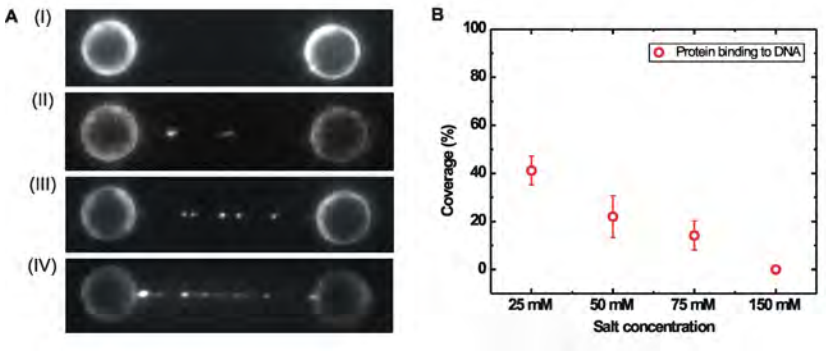

Figure 55.: **The binding affinity of XRCC4 and XLF complexes is influenced by the salt concentration.** [A] Fluorescent images obtained after three minutes of incubation in 200 nM XRCC4-Alexa555, 200 nM XLF and 20 mM Tris (pH=7.5) in (I) 150 mM KCl, (II) 75 mM KCl, (III) 50 mM KCl, (IV) 25 mM KCl. [B] The average protein coverages on the DNA (%) as a function of salt concentration, we found 41±6 % (N=16), 22±9 % (N=7), 19±6 (N=10) and 0% (N=5) for 25, 50, 75 and 150 mM, respectively. DNA-protein complex formation clearly decreases at higher ionic strengths.

7.3.2 Mechanical properties of DNA in complex with XRCC4-XLF

It is not known how XRCC4-XLF complexes interact with DNA. In general, it is well known that protein binding can affect the mechanical properties of the DNA, depending on the nature of the DNA-protein interactions [32]. For XRCC4-XLF, two contradicting views on the interaction of these proteins with DNA have been proposed: in one the DNA and proteins interact in a histone-like fashion [64], while in the second the proteins form helical filaments around the DNA [5, 182]. If the first view were correct, one would expect a substantial shortening of the DNA contour length. In addition, depending on the DNA-binding strategy employed by the XRCC4 and XLF, the assembly kinetic can be influenced by the stretching force applied on the DNA.

Mechanical properties of XRCC4-XLF filaments on DNA

In order to gain insights in the DNA binding mechanism of XRCC4-XLF binding to DNA we recorded force-extension curves. To this end,

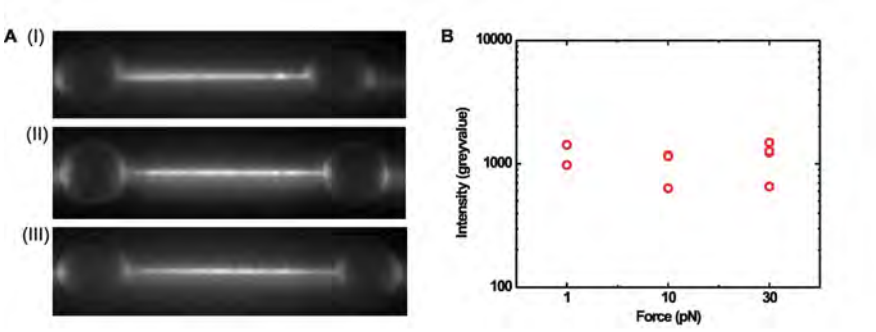

Figure 56.: XRCC4-XLF binding affinity to DNA is independent to tension. [A] Fluorescent images of DNAs that were incubated for 60s in 200 nM XRCC4-Alexa555 and 2 μM XLF. The molecules were stretched to (i) 1 pN; (ii) 10 pN and (iii) 30 pN. [B] Quantification of fluorescence intensity for individual DNA-protein complexes shows that protein binding to DNA is independent on the applied tension.

DNA subjected to tensions ranging from 1 to 30 pN was incubated with XRCC4 and XLF at high concentrations (20 mM Tris pH 7.5, 25 mM KCl, 200 nM XRCC4-Alexa555 and 2 μM XLF). Fluorescence images confirmed that DNA molecules were fully covered with XRCC4-XLF, independent of tension (see Figure 56). Next, force-distance curves were recorded and compared to curves obtained before incubation with XRCC4 and XLF. An example, in Figure 57, shows that the force-extension curve of DNA is not altered by the presence of XRCC4-XLF (as confirmed by the fluorescence image, inset), indicating that the binding of XRCC4-XLF does not influence the elastic properties of DNA in a detectable way.

Selectivity of XRCC4-XLF binding

We also studied whether the nature of the DNA, single-stranded versus double-stranded, affects binding of XRCC4-XLF. To this end, DNA was overstretched, beyond its crystallographic contour length to a length of 26 μm. In this way, at low salt concentrations (25 mM KCl), a spatially segregated ssDNA-dsDNA hybrid structure was created due to force-induced melting [60]. Next, this hybrid was incubated with XRCC4-XLF while the tension was fixed at 65 pN and fluorescence images were recorded. Figure 58.A shows that part of the hybrid-DNA molecule was not fluorescent, while the rest was fluorescent, in the same way as a completely double-stranded DNA (Figure 58.A). This result indicates that XRCC4-XLF binds specifically to dsDNA and not to ssDNA under tension.

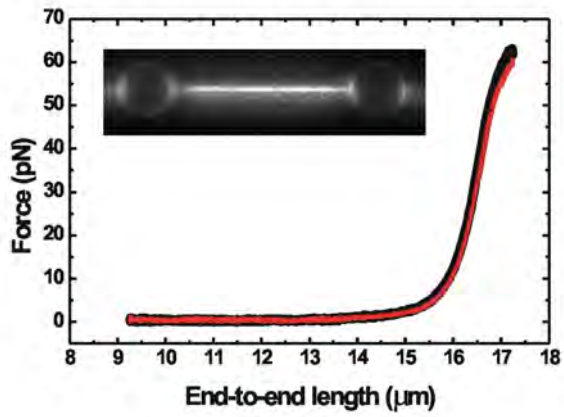

Figure 57.: XRCC4-XLF does not alter the mechanical properties of dsDNA XRCC4-XLF does not alter the mechanical properties of dsDNA. Force-distance curve of a DNA molecule before (black curve) and after (red) incubation in 200 nM of XRCC4-Alexa555 and 2 μM of XLF. In the inset, a fluorescent snapshot of the DNA-protein complex after the incubation step confirming the full fluorescent coverage.

7.3.3 Dynamic properties of XRCC4-XLF filaments on DNA

Binding modes of XRCC4-XLF on DNA

A more detailed inspection of sequences of fluorescence images of XRCC4-Alexa555 bound to dsDNA indicated that some of the XRCC4 complexes move along the DNA while remaining bound. Other complexes appear instead to be static. XRCC4, therefore, displays two distinct binding modes on the DNA: a dynamic and static one (Figure 59.A). Before further analysis of the motility parameters, we tested whether XRCC4-XLF complexes show the same behaviour. Using large excess of XLF (1:25), image sequences show that also XRCC4-XLF complexes display both DNA-binding modes (see Figure 59.B). This suggests that the dual DNA binding mode is a feature of both XRCC4 and XRCC4-XLF complexes.

Dynamic switching between static and diffusive states

In addition, we also observed individual XRCC4-XLF complexes switching from static to dynamic behaviour and vice versa (see Figure 60.A, B and C). In some cases, we observed that the motion of dynamic complexes appeared to be confined (yellow line Figure 60.D). The molecular causes of both switching and confinement are unknown. We speculate that both effects are triggered by recognition of altered DNA structures, for example nick or gaps [112] or of specific sequences on the DNA. Further

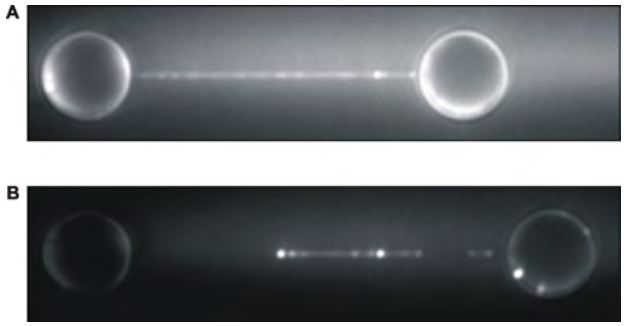

Figure 58.: XRCC4-XLF binding is specific for dsDNA. [A] A dsDNA molecule stretched at 50 pN shows full coverage after incubation with 200 nM of Alexa555-XRCC4 and 2 μM of XLF (incubation time=1min). [B] Fluorescent image showing a spatially separated fluorescent coating. The DNA molecule was first overstretched ($L_{contour}$=26 μm and F=65 pN) and after incubated with 200 nM of XRCC4-Alexa555 and 2 μM of XLF (Incubation time=1min). The proteins bind specifically to the regions corresponding to the intact segments of dsDNA.

experiments involving sequence-specific nicks and, better defined DNA-orientation might shed further light on these intriguing observations.

7.3.4 Diffusion of XRCC4-XLF on DNA

Salt effect on XRCC4-XLF diffusion on DNA

Next, we quantified the motility parameters of the dynamic XRCC4 and XRCC4-XLF complexes, by tracking the fluorescent spots with an accuracy of less than 10 nm using two-dimensional Gaussian fitting [25] (Figure 61.A). From trajectories obtained in this way, we determined the mean squared displacements (MSD) as a function of lag time (see Figure 61.B). We found that MSD increases with time in a linear way, a hallmark of free diffusion (Figure 61.C). By fitting a line to the MSD as a function of lag time we determined the one-dimensional diffusion coefficient (Figure 61.C). For XRCC4-Alexa555 (20 mM Tris; 25 mM KCl) we found a diffusion coefficient of 1.07±0.02 $\mu m^2/s$ (mean±SE, N=10). For XRCC4-XLF complexes (DNA molecules incubated in a 1:1 solution), a similar value was obtained (0.97±0.02 $\mu m^2/s$, mean±SE, N=40). Increasing the KCl concentration to 75 mM resulted in a slightly slower diffusion of the XRCC4-XLF complex (0.59±0.02 $\mu m^2/s$, mean±SE, N=30).

Specific DNA-ends bound protein complexes

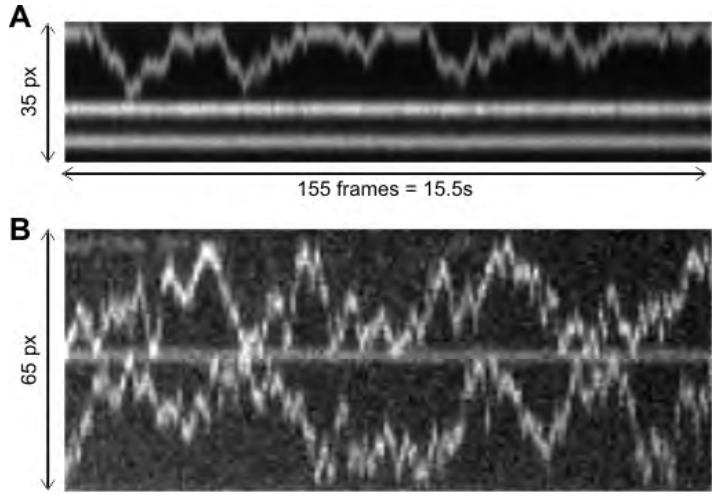

Figure 59.: XRCC4 and XRCC4-XLF show both diffusive and static behaviors. [A] Kymograph showing a DNA segments after incubation with XRCC4 (100 nM). We observe both static and diffusive fluorescent complexes. [B] Kymograph showing a DNA segments after incubation with XRCC4-XLF ([XRCC4-Alexa555]=100 nM and [XLF]=2.5 μM). Also in this case, the two binding modes are retained.

In the cell, XRCC4-XLF complexes bind and move along DNA with a free (broken) end, unlike the experiments described above, where DNA ends are both engaged with the microspheres required for optical trapping. To test whether end-specific effects occur, we attached the DNA with only one of its ends to an optically trapped microsphere and extended it in a constant buffer flow, leaving the other end free. In these experiments, the molecule was incubated in 200 nM XRCC4-Alexa555 and 200 nM XLF in presence of 20 mM Tris pH 7.5 and 50 mM KCl. We observed that in most of these flow-stretching experiments, XRCC4-XLF was found bound only at the free DNA end (Figure 62.A). We wondered whether this observation is the result of specific end-binding or an artifact due to the hydrodynamic drag pushing diffusing XRCC4-XLF complexes towards the DNA end. To answer this, we returned to the dual beads configuration and investigated the effect of buffer flow on diffusing XRCC4-XLF complexes. We found that complexes are moved in the direction of the buffer flow, as shown in Figure 62.B. We therefore conclude that buffer flow can bias the diffusion of DNA-bound XRCC4-XLF complexes, resulting in the DNA-end-bound complexes observed in the flow-stretching experiments.

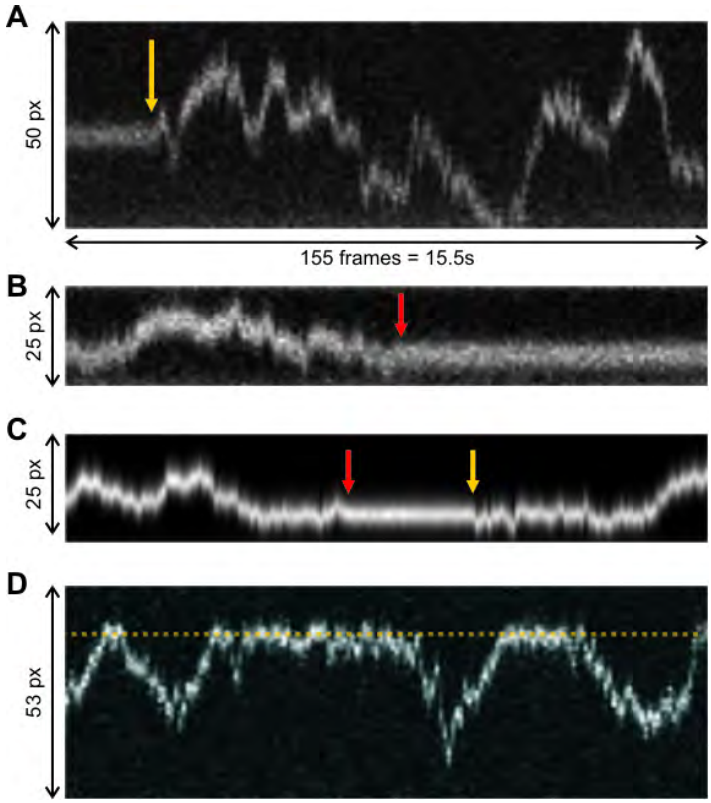

Figure 60.: XRCC4-XLF complexes switch dynamically from diffusive to static states. [A] Kymograph shows a fluorescent XRCC4-XLF complex undergoing a transition from static to a diffusive state (yellow arrow). [B] Kymograph shows the diffusive to static switching (red arrow). [C] Kymograph shows the diffusive to static switching (yellow arrow) and a consecutive static to diffusive switching (red arrow). [D] Kymograph shows a fluorescent XRCC4-XLF complexes not able to bypass the region on the DNA marked with the dotted yellow line (confined diffusion). Experiments were performed using 200 nM XRCC4-Alexa555 and 200 nM XLF in 20 mM Tris-HCl pH 7.5 and 25 mM KCl.

7.3.5 Formation of XRCC4-XLF filaments

Filament formation mechanism of XRCC4-XLF on DNA

We also investigated the mechanism of formation of XRCC4-XLF complexes on DNA. Two distinct strategies have been described for protein complexes forming on DNA. Recombinase proteins such as RAD51 and RecA bind to DNA from solution in a highly cooperative fashion, involving a rate-limiting nucleation step followed by polymerization [72, 55]. For

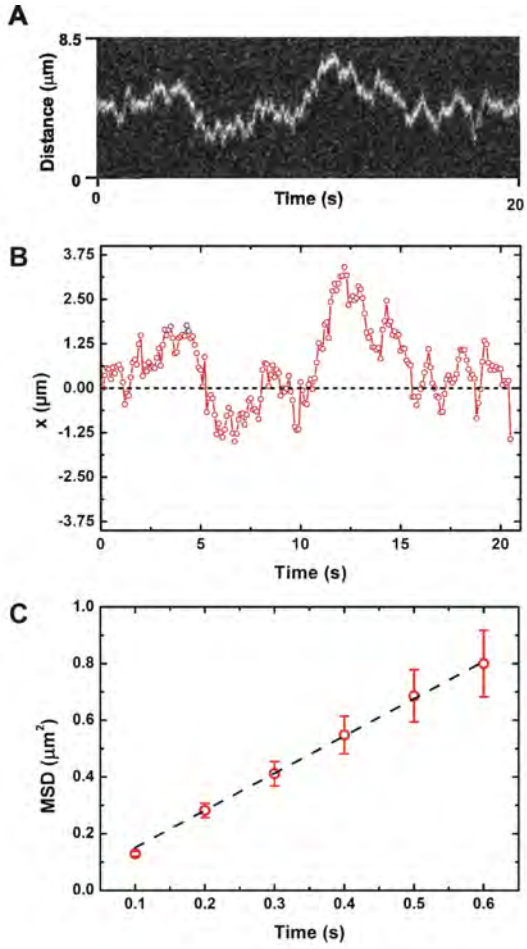

Figure 61.: Single particle tracking of XRCC4-XLF complexes diffusing along DNA. [A] Kymograph shows the diffusion of a single XRCC4-XLF complex along a single DNA molecule after incubation with 150 nM XRCC4-Alexa555 and 150 nM XLF. [B] Single-particle tracking allows determining the time-trajectory of the fluorescent spot. [C] Mean squared displacement (MSD) analysis of the diffusive particle. The diffusion coefficient is extracted from the linear fit (dashed black line) to the MSD plot, in this case D=0.66±0.01 $\mu m^2/s$.

proteins characterized by a low cooperativity in DNA binding, such as mitochondrial transcription factor A, an alternative mechanism has been proposed, with individual proteins or protein-complexes randomly moving along the DNA colliding and coalescing into larger structures [51]. To

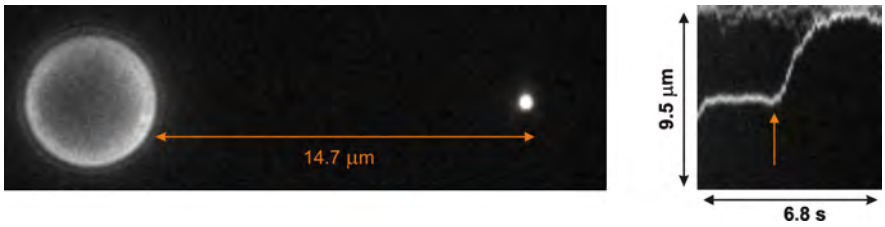

Figure 62.: **Single particle tracking of XRCC4-XLF complexes diffusing along DNA.** [A] Kymograph shows the diffusion of a single XRCC4-XLF complex along a single DNA molecule after incubation with 150 nM XRCC4-Alexa555 and 150 nM XLF. [B] Single-particle tracking allows determining the time-trajectory of the fluorescent spot. [C] Mean squared displacement (MSD) analysis of the diffusive particle. The diffusion coefficient is extracted from the linear fit (dashed black line) to the MSD plot, in this case D=0.66±0.01 $\mu m^2/s$.

test whether XRCC4-XLF follows one of these strategies, we monitored complex formation in real-time (see Figure 62). We observed that XRCC4-XLF complexes appear randomly and abruptly along the DNA and remain bound for a long time. The fluorescence intensity of the fluorescents complexes remains constant for the duration of the measurement indicating that growth of the complexes is a rare event. In several cases, we observed the collision of distinct, diffusing particles. Upon collision, particles either merged, forming larger complexes (see Figure 63.A), or "bounced" (see Figure 63.B), resulting in rapid dissociation of collision complexes. We also observed complexes bound to the DNA to break into fragments (Figure 63.C), further highlighting that XRCC4-XLF complexes on DNA are highly dynamic, undergoing continuous rearrangement.

7.3.6 DNA bridging at the single-molecule level

Finally, we tested whether XRCC4-XLF complexes possess the ability of bridging two DNA molecules. In a first attempt to study bridging, we trapped a single DNA molecule between two microspheres. While incubating for three to five minutes in 200 nM XRCC4-Alexa555 and 200 nM XLF (in 20 mM Tris (pH 7.5), 25 mM KCl), the DNA was kept in an extended configuration (tension in the range of 1-50 pN).

DNA bridging studied using single-DNA molecule manipulation

Subsequently the DNA was relaxed to an end-to-end distance of 7 μm for two minutes allowing distinct XRCC4-XLF-coated segments to come

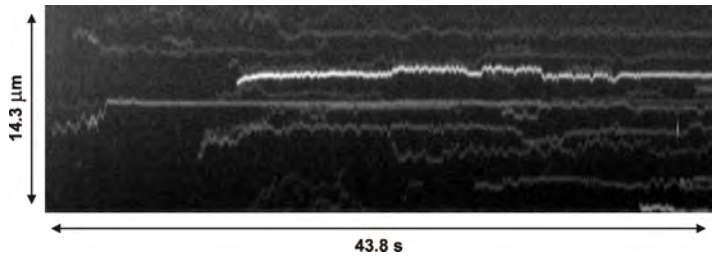

Figure 63.: XRCC4-XLF assembly on DNA is visualized in real-time. The appearance of fluorescent patches on DNA occurs randomly at different positions. Once bound, the fluorescence intensity stays constant, indicating that filament growth is not taking place during the timescale of the experiment.

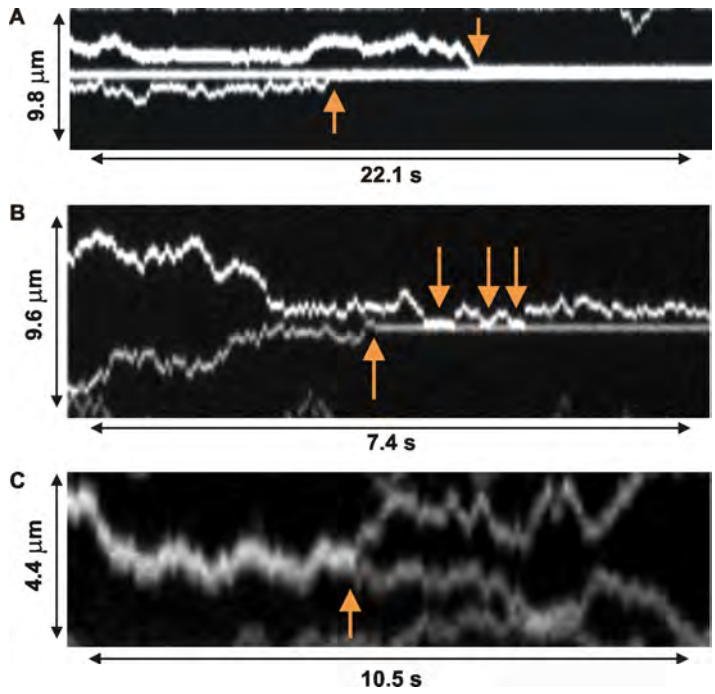

Figure 64.: Assembly and fragmentation of XRCC4-XLF complexes. [A] Kymograph showing multiple XRCC4-XLF complexes colliding (orange arrows) and forming a larger protein structure on the DNA. [B] Collision between XRCC4-XLF filaments resulting in transient complex formation (orange arrows). [C] Individual XRCC4-XLF complex fragmenting (orange arrow) into smaller filaments.

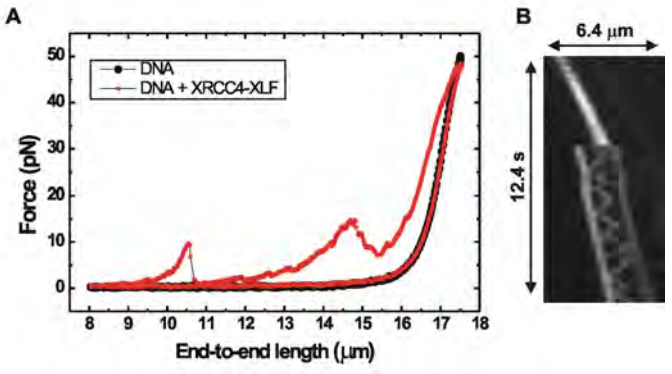

Figure 65.: XRCC4-XLF catalyzes the formation of intra-molecular bridges. [A] The force distance curve of naked DNA molecule is shown in black. The force-extension after incubation with XRCC4-XLF is shown in red. [B] Kymograph recorded during bead separation shows the rupture of an intra-molecular bridge mediated by XRCC4-XLF.

into contact due to DNA thermal motion. Afterwards, force-extension curves were measured (see Figure 65.A). These force-extension curves showed complex behavior: extension involved many force ramps and sudden force drops, most likely representing the rupture of intra-molecular bridges formed by XRCC4-XLF. At forces above 50 pN the XRCC4-XLF-coated DNA is extended comparably to naked DNA. Notably, force-extension curves recorded upon relaxing the XRCC4-XLF-coated DNA are indistinguishable from naked DNA.

A kymograph obtained from fluorescence images recorded during extension of a XRCC4-XLF coated DNA molecule, Figure 65.B, clearly shows the rupture (arrow) of a DNA bridge formed between two XRCC4-XLF complexes bound on different parts of the DNA. This observation confirms that XRCC4-XLF bound to DNA has DNA-bridging activity. Note that the use of fluorescence visualization is essential to discriminate between intra-molecular bridges formed by XRCC4 and XLF and DNA-protein adsorption to the optically trapped microspheres (Supplementary Figure S72).

In order to obtain further insight in the DNA-bridging activity of XRCC4-XLF and to avoid artefacts due to DNA binding to the optically trapped microspheres, we developed a novel assay for studying the DNA-end bridging catalysed by XRCC4 and XLF. The experiment was performed us-

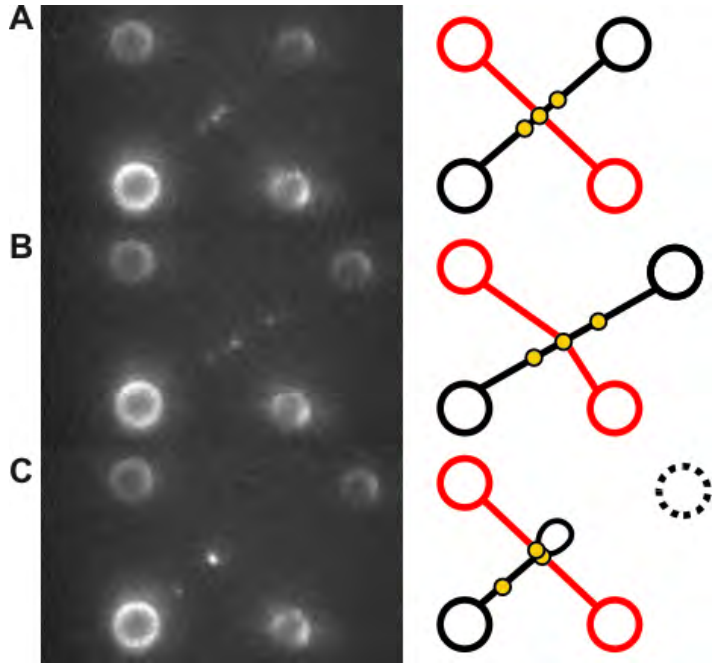

Figure 66.: Intra-molecular bridging catalyzed by XRCC4-XLF complex and creation of three-way junction. [A] Fluorescent visualization of two crossed DNA molecules with three distinct XRCC4-XLF complexes bound. [B] The top-right bead is moved towards the right, stretching the black DNA molecule into the overstretching transition. [C] After rupture of the black DNA strand due to force-induced unpeeling across a nick, a three way junction is formed. We noticed an increased fluorescence intensity at the DNA crossing position. This indicates that the segments of the black DNA molecule recoiled at the junction, probably extruding a DNA loop.

DNA bridging studied using dual-DNA molecule manipulation

ing quadruple-trap optical tweezers allowing manipulation of two DNA molecules, in combination with fluorescence visualization.

In this preliminary experiment, we trapped four individual microspheres in each of the four controllable optical traps. After a dual DNA tether system was produced, the DNA molecules were subsequently crossed. Next, the DNA molecules in the crossed configuration were incubated in 300 nM XRCC4-Alexa555 and 800 nM XLF (20 mM Tris, 25 mM KCl) for 30 seconds. Subsequently the DNA molecules were transferred to the observation channel for further inspection and manipulation. We observed a static XRCC4-XLF complex located at the location where the two DNA molecules

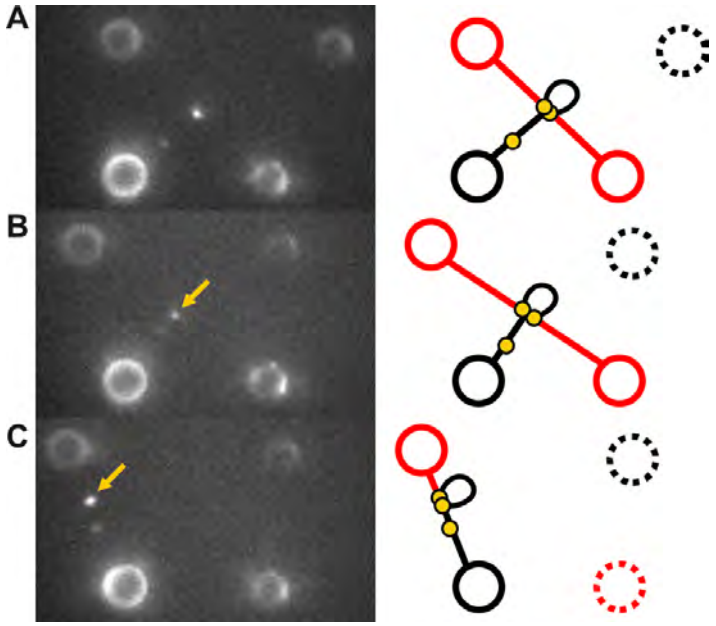

Figure 67.: Creation of a DNA tether consisting of two XRCC4-XLF-bridged DNA molecules. [A] Three-way junction DNA construct. [B] The red DNA molecule is stretched into the overstretching transition by moving the top left bead. [C] After force-induce rupture of the DNA, a single DNA tether consisting of two linked DNA molecules is created.

were expected to cross (Figure 66.A). To verify that this indeed represented an actual inter-DNA bridge, we stretched one of the two DNAs by moving the top-right bead to the right (Figure 66.B).

Upon applying tensions exceeding the overstretching force (F>65 pN), DNA starts unpeeling. In cases where the force-induced unpeeling runs across a nick, the DNA molecule breaks, as is observed in Figure 66.C. Upon DNA rupture, part of the broken strand recoiled to the initial bridge point, resulting in an increase of the fluorescence intensity. This observation suggests that part of the broken DNA strand formed a loop as depicted in Figure 66.C. In this way, a three-way junction was formed as can be confirmed by DNA manipulation and, more directly, by fluorescence visualization, since one of the fluorescent spots diffuses between the bottom-left microsphere and the crossing point. The three-way junction held with three optical traps was further manipulated by moving the top-left microsphere further to the left, resulting in tensions above 65 pN on

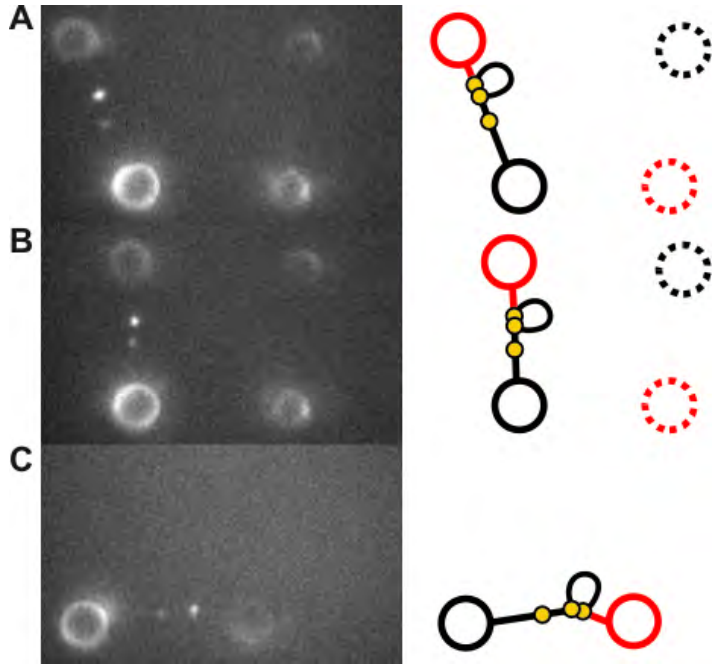

Figure 68.: Moving optically trapped microspheres confirms the stability of the bridged DNA molecules. [A] Single DNA tether consisting of two DNA molecules bridged by XRCC4-XLF (same as Figure 66.C). [B] Moving the top-left microsphere (red) confirms the existence of a stable bridge between both DNA molecules. [C] Release of the untethered microspheres and positioning of the DNA molecule in a horizontal configuration.

one of the DNAs (red in Figure 67.A). The high tension applied, again, resulted in the rupture of one of the DNA molecules.

Upon rupture, one of the fluorescent spots moves to the junction point (yellow arrow in Figure 66.B and Figure 66.C). We hypothesized that the resulting DNA tether between two beads consisted of two DNA molecules bridged by XRCC4-XLF. To test this, we kept on moving the top-left bead until the tether was horizontal (see Figure 68). Finally, we stretched the bridged DNA molecules taut, until the intra-molecular bridge formed by XRCC4-XLF is broken and both DNA molecules recoiled on the trapped microspheres (see Figure 69). Obviously, these experiments provide the first hints of the power of our experimental strategy and the first direct proof of the bridging capability of XRCC4 and XLF.

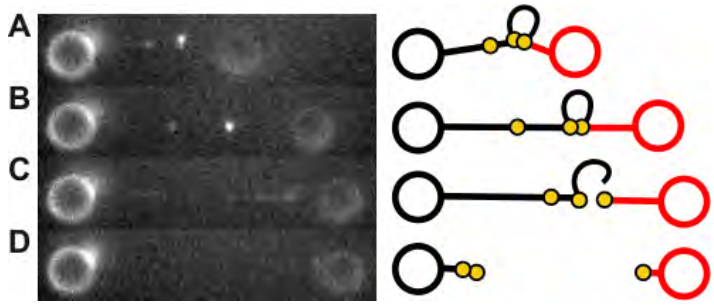

Figure 69.: **Force-induced rupture of the DNA tether consisting of two DNA molecules bridged by XRCC4-XLF.** [A] Two DNA molecules bridged by XRCC4-XLF forming a single tether between the two optically trapped microspheres (see Figure 67.C). [B] Force-induced extension of the bridged-DNA tether. [C] Forces of about 10 pN resulted in rupture of the inter-DNA bridge. The fluorescent snapshot show recoiling of the broken ends towards the tethered end. [D] Final fluorescent snapshot confirming the rupture of the DNA tether.

7.4 DISCUSSION

DNA binding strategy by XRCC4-XLF

In summary, we have studied the mechanisms of DNA binding and bridging by XRCC4 and XRCC4-XLF complexes. We have shown that both XRCC4 and XRCC4-XLF complexes are able to bind to DNA under tension, without affecting its mechanical properties. A DNA-binding mechanism by XRCC4 and XRCC4-XLF complexes resemblying histones is therefore highly unlikely, since this would result in shortening of the DNA [64]. Our observations are consistent instead with XRCC4-XLF forming a filament around the DNA.

XRCC4-XLF filament assembly on DNA as a regulatory poring during NHEJ

This hypothesis agrees very well with x-ray structural data, reporting an internal diameter of the XRCC4-XLF helix of approximately 10 nm, enough to accommodate dsDNA [5, 64, 137, 182]. The inhibitory effect on the DNA binding kinetic exerted by physiological salt concentrations suggest that in vivo, accessory factors might be required for the efficient formation of a DNA-protein complex. Cellular studies demonstrated that recruiting of XRCC4 at the site of damage depends on the presence of Ku70/80 [102]. Future experiment will clarify the role of Ku70/80 at the single-molecule level, in order to obtain a full picture of the regulation of XRCC4-XLF filament formation. Once bound, XRCC4-XLF filaments interact with the DNA for long periods, and can be observed for up to 20 minutes. This sug-

gests that the DNA binding is a near-irreversible process, and that XRCC4-XLF filaments are highly stable on the DNA. This also might imply that the disassembly of the XRCC4-XLF filaments could be a regulatory-point during NHEJ in vivo. A possible actor in the disassembly of the filaments is DNA-PKcs, which has been shown to phosphorylate XRCC4 and ablate its bridging function [141].

Binding modes of XRCC4-XLF filaments

Nevertheless, these long binding times allowed us to unravel the dynamics of XRCC4-XLF bound to DNA. While a fraction of the XRCC4-XLF complexes remained statically bound to the same spot on the DNA, many complexes moved along the DNA, showing random diffusive behaviour. We have observed transitions between both XRCC4-XLF binding modes. Interestingly, bulk biochemical approaches have shown before that two binding modes exist and that only one of them is able to bridge DNA [5], although further characterization of the two modes was not possible.

Fast diffusion of XRCC4-XLF filaments

Quantitative analysis of the diffusion of DNA-bound XRCC4-XLF revealed an unusually high diffusion coefficient, in the order of 1 $\mu m^2/s$, comparable to hOgg1, a globular protein with a hydrodynamic radius of only 3.2 nm [19], which spins around the DNA double helix [18]. XRCC4-XLF forms extended helical filaments consisting of many tens of monomers, much larger than hOgg1. Consequently, it is very surprising that the diffusion coefficients of these proteins are similar while their size is so different. Most likely, the mechanism with which XRCC4-XLF complexes diffuse along DNA is substantially different. A possible mechanism might be that the helical XRCC4-XLF complex forms a filament around the DNA that only weakly interacts with it, but can hardly detach. This is confirmed by the observation that forces as weak as the hydrodynamic drag ($\sim$10 fN) caused by the buffer flow, alter substantially the diffusion process, causing drift. Interestingly, the flow was able to accumulate fluorescent XRCC4-XLF protein on the free-end of the DNA. It is difficult to reconcile the filamentous structure of XRCC4-XLF shown by X-ray crystallography [5] with this end-accumulation without invoking a binding mechanism specific for DNA-ends.

Filament formation mechanism of XRCC4-XLF

Another interesting aspect of XRCC4-XLF interaction with DNA is that increasing the salt concentration slows down diffusion, indicating that better screened charges increase the interaction between DNA and XRCC4-XLF. By visualizing the formation of XRCC4-XLF complexes in real-time we also found that complexes do not form via a canonical nucleation-

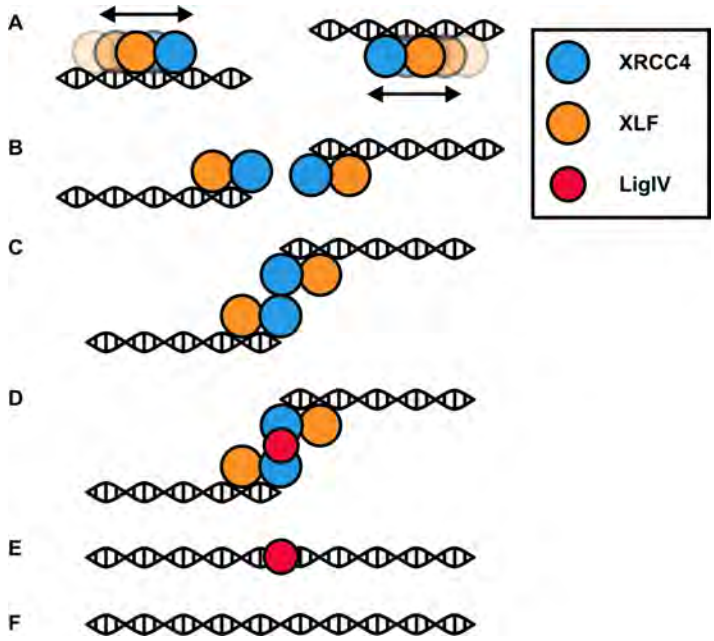

Figure 70.: Schematic representation of the role of XRCC4 and XLF role in NHEJ. [A] XRCC4-XLF forms alternating helical filaments on the broken DNA molecule. The filaments are highly mobile on the DNA through a 1-dimensional diffusion mechanism. [B] One-dimensional diffusion permits the XRCC4-XLF complex to reach the broken DNA ends through a specific recognition mechanism. [C] The tail domains of XRCC4 interact, creating an intermolecular bridge between the broken DNAs.

growth mechanism. Instead, we propose a different filament assembly scheme. XRCC4-XLF complexes bind to and diffuse along the DNA, occasionally colliding with each other. Upon collision, complexes can coalesce and form larger DNA-protein structures, similarly to the assembly of TFAM on mitochondrial DNA [51] and Ase1p on microtubules [87]. XRCC4 is able to self-assemble in solution into long homopolymers [85]. XLF can remodel these structures, forming short hetero-complexes of XRCC4 and XLF [182]. These XRCC4-XLF complexes show, in turn, fast binding kinetic to DNA and are able to form regular helical filaments on the DNA, as indicated by the homogeneous fluorescent signal noticed in our measurements. Finally we demonstrated a novel assay, allowing the direct visualization and verification of the bridging properties of XRCC4-XLF complexes.

Sliding, pausing and bridging and their relevance for DNA repair in vivo

In conclusion, based on our results we propose that diffusion (sliding), switching from dynamic to static states (pausing) and bridging are the key ingredients for in the function of XRCC4-XLF in NHEJ (see Figure 70). Fast diffusion and dynamic switching state might represent a strategy to localize DNA breaks and bind to them in an effective way. The thus formed DNA-bound XRCC4-XLF complexes are able to form stable bridges between DNA molecules, without the need for other proteins. We argue that DNA bridging by XRCC4-XLF is vital for end ligation for two reasons: (i) physically linking the two broken DNA molecules may prevent the broken DNA ends to move apart and (ii) LigIV has been shown to interact with the C-terminal tail of XRCC4, the putative bridging domain of XRCC4 [153, 5, 113]. The fact that both DNA-bridging activity and LigIV binding involves the C-terminal domain of XRCC4 could indicate that XRCC4-XLF bridging DNA localizes Lig IV to the broken DNA ends, where it can perform the final ligation step.

C | SUPPLEMENTARY FIGURES

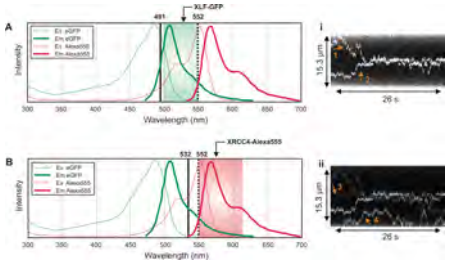

Figure S71.: Dual color excitation and emission of XLF-eGFP and XRCC4-Alexa555. [A] XLF-eGFP is excited with a 491 nm laser and the emitted light is filtered using a dichroic mirror (552 nm) and a single-band band-pass filter (550/88 nm). The EMCCD region for eGFP detection is colored in green. [i] eGFP-XLF complexes (1 and 2, orange arrows) are detected in the eGFP channel of the EMCCD. [B] Excitation with a 532 nm laser predominantly excites Alexa555 fluorophores. The emitted light that is led through the dichroic mirror (552 nm) is further filtered using a single-band band-pass filter (580/60 nm). The EMCCD region for Alexa555 detection is colored in red. [ii] Kymograph showing the Alexa555 channel when excitation is performed using a 532 nm laser. Complexes 3 and 4 consist only of XRCC4-Alexa555. Complexes 1 and 2 are present in both kymographs and represent XRCC4-XLF complexes.

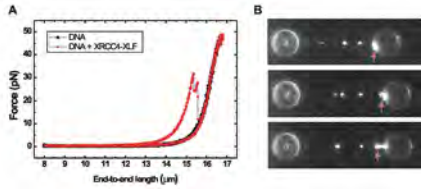

Figure S72.: Force-induced melting of dsDNA was employed to produce ssDNA templates. Force-stretching curve of a 38412 bp dsDNA(Black line). The molecule was pulled beyond the overstretching plateau (F>85 pN). The force-stretching curve (red line) confirmed the generation of a single ssDNA molecule tethered between the beads.

BIBLIOGRAPHY

[1] E. A. Abbondanzieri, W. J. Greenleaf, J. W. Shaevitz, R. Landick, and S. M. Block. Direct observation of base-pair stepping by RNA polymerase. *Nature*, 438(7067):460–5, Nov. 2005.

[2] K. Adzuma. No sliding during homology search by RecA protein. *The Journal of biological chemistry*, 273(47):31565–73, Nov. 1998.

[3] P. Ahnesorg, P. Smith, and S. P. Jackson. XLF interacts with the XRCC4-DNA ligase IV complex to promote DNA nonhomologous end-joining. *Cell*, 124(2):301–13, Jan. 2006.

[4] S. N. Andres, M. Modesti, C. J. Tsai, G. Chu, and M. S. Junop. Crystal structure of human XLF: a twist in nonhomologous DNA end-joining. *Molecular cell*, 28(6):1093–101, Dec. 2007.

[5] S. N. Andres, A. Vergnes, D. Ristic, C. Wyman, M. Modesti, and M. Junop. A human XRCC4-XLF complex bridges DNA. *Nucleic acids research*, 40(4):1868–78, Feb. 2012.

[6] H. Arata, A. Dupont, J. Miné-Hattab, L. Disseau, A. Renodon-Cornière, M. Takahashi, J.-L. Viovy, and G. Cappello. Direct observation of twisting steps during Rad51 polymerization on DNA. *Proceedings of the National Academy of Sciences of the United States of America*, 106(46):19239–44, Nov. 2009.

[7] A. Ashkin, J. M. Dziedzic, J. E. Bjorkholm, and S. Chu. Observation of a single-beam gradient force optical trap for dielectric particles. *Optics Letters*, 11(5):288, May 1986.

[8] Y. Aylon, B. Liefshitz, G. Bitan-Banin, and M. Kupiec. Molecular dissection of mitotic recombination in the yeast Saccharomyces cerevisiae. *Molecular and cellular biology*, 23(4):1403–17, Feb. 2003.

[9] A. Barzel and M. Kupiec. Finding a match: how do homologous sequences get together for recombination? *Nature reviews. Genetics*, 9(1):27–37, Jan. 2008.

[10] P. Baumann, F. E. Benson, and S. C. West. Human Rad51 protein promotes ATP-dependent homologous pairing and strand transfer reactions in vitro. *Cell*, 87(4):757–66, Nov. 1996.

[11] L. R. Bazemore, E. Folta-Stogniew, M. Takahashi, and C. M. Radding. RecA tests homology at both pairing and strand exchange. *Proceedings of the National Academy of Sciences of the United States of America*, 94(22):11863–8, Oct. 1997.

[12] J. C. Bell, J. L. Plank, C. C. Dombrowski, and S. C. Kowalczykowski. Direct imaging of RecA nucleation and growth on single molecules of SSB-coated ssDNA. *Nature*, 491(7423):274–8, Nov. 2012.

[13] M. L. Bennink, O. D. Schärer, R. Kanaar, K. Sakata-Sogawa, J. M. Schins, J. S. Kanger, B. G. de Grooth, and J. Greve. Single-molecule manipulation of double-stranded DNA using optical tweezers: interaction studies of DNA with RecA and YOYO-1. *Cytometry*, 36(3):200–8, July 1999.

[14] F. E. Benson, A. Stasiak, and S. C. West. Purification and characterization of the human Rad51 protein, an analogue of E. coli RecA. *The EMBO journal*, 13(23):5764–5771, 1994.

[15] P. R. Bianco, L. R. Brewer, M. Corzett, R. Balhorn, Y. Yeh, S. C. Kowalczykowski, and R. J. Baskin. Processive translocation and DNA unwinding by individual RecBCD enzyme molecules. *Nature*, 409(6818):374–8, Jan. 2001.

[16] P. R. Bianco, R. B. Tracy, and S. C. Kowalczykowski. DNA strand exchange proteins: a biochemical and physical comparison. *Frontiers in bioscience : a journal and virtual library*, 3:D570–603, June 1998.

[17] A. Biebricher, W. Wende, C. Escudé, A. Pingoud, and P. Desbiolles. Tracking of single quantum dot labeled EcoRV sliding along DNA manipulated by double optical tweezers. *Biophysical journal*, 96(8):L50–2, Apr. 2009.

[18] P. C. Blainey, G. Luo, S. C. Kou, W. F. Mangel, G. L. Verdine, B. Bagchi, and X. S. Xie. Nonspecifically bound proteins spin while diffusing along DNA. *Nature structural & molecular biology*, 16(12):1224–9, Dec. 2009.

[19] P. C. Blainey, A. M. van Oijent, A. Banerjee, G. L. Verdine, X. S. Xie, and A. M. van Oijen. A base-excision DNA-repair protein finds intrahelical lesion bases by fast sliding in contact with DNA. *Proceedings of the National Academy of Sciences of the United States of America*, 103(15):5752–7, Apr. 2006.

[20] I. Bonnet, A. Biebricher, P.-L. Porté, C. Loverdo, O. Bénichou, R. Voituriez, C. Escudé, W. Wende, A. Pingoud, and P. Desbiolles. Sliding and jumping of single EcoRV restriction enzymes on non-cognate DNA. *Nucleic acids research*, 36(12):4118–27, July 2008.

[21] R. R. Brau, P. B. Tarsa, J. M. Ferrer, P. Lee, and M. J. Lang. Interlaced optical force-fluorescence measurements for single molecule biophysics. *Biophysical journal*, 91(3):1069–77, Aug. 2006.

[22] L. Brewer and P. Bianco. Laminar flow cells for single-molecule studies of DNA-protein interactions. *Nature methods*, 5(6):517–525, 2008.

[23] D. V. Bugreev and A. V. Mazin. Ca2+ activates human homologous recombination protein Rad51 by modulating its ATPase activity. *Proceedings of the National Academy of Sciences of the United States of America*, 101(27):9988–93, July 2004.

[24] K. W. Caldecott. Single-strand break repair and genetic disease. *Nature reviews. Genetics*, 9(8):619–31, Aug. 2008.

[25] A. Candelli, G. J. L. Wuite, and E. J. G. Peterman. Combining optical trapping, fluorescence microscopy and micro-fluidics for single molecule studies of DNA-protein interactions. *Physical chemistry chemical physics : PCCP*, 13(16):7263–72, Apr. 2011.

[26] M. Capitanio, D. Maggi, F. Vanzi, and F. S. Pavone. FIONA in the trap: the advantages of combining optical tweezers and fluorescence. *Journal of Optics A: Pure and Applied Optics*, 9(8):S157–S163, Aug. 2007.

[27] A. Carreira, J. Hilario, I. Amitani, R. J. Baskin, M. K. K. Shivji, A. R. Venkitaraman, and S. C. Kowalczykowski. The BRC Repeats of BRCA2 Modulate the DNA-Binding Selectivity of RAD51. *Cell*, 136(6):1032–1043, 2009.

[28] A. Carreira and S. C. Kowalczykowski. Two classes of BRC repeats in BRCA2 promote RAD51 nucleoprotein filament function by distinct mechanisms. *Proceedings of the National Academy of Sciences of the United States of America*, 108(26):10448–53, June 2011.

[29] a. Cerbinskaite, a. Mukhopadhyay, E. R. Plummer, N. J. Curtin, and R. J. Edmondson. Defective homologous recombination in human cancers. *Cancer treatment reviews*, 38(2):89–100, Apr. 2012.

[30] M. Chabbert, C. Cazenave, and C. Hélène. Kinetic studies of recA protein binding to a fluorescent single-stranded polynucleotide. *Biochemistry*, 26(8):2218–25, Apr. 1987.

[31] J. R. Chapman, M. R. G. Taylor, and S. J. Boulton. Playing the end game: DNA double-strand break repair pathway choice. *Molecular cell*, 47(4):497–510, Aug. 2012.

[32] K. R. Chaurasiya, T. Paramanathan, M. J. McCauley, and M. C. Williams. Biophysical characterization of DNA binding from single molecule force measurements. *Physics of life reviews*, 7(3):299–341, Sept. 2010.

[33] Z. Chen, H. Yang, and N. P. Pavletich. Mechanism of homologous recombination from the RecA-ssDNA/dsDNA structures. *Nature*, 453(7194):489–4, May 2008.

[34] S. B. Chernikova, J. C. Game, and J. M. Brown. Inhibiting homologous recombination for cancer therapy. *Cancer biology & therapy*, 13(2):61–8, Jan. 2012.

[35] P. Cluzel, A. Lebrun, C. Heller, R. Lavery, J.-L. Viovy, D. Chatenay, and F. o. Caron. DNA: An Extensible Molecule. *Science*, 271(5250):792–794, Feb. 1996.

[36] M. J. Comstock, T. Ha, and Y. R. Chemla. Ultrahigh-resolution optical trap with single-fluorophore sensitivity. *Nature methods*, 8(4):335–40, Apr. 2011.

[37] A. J. Conover, C. Danilowicz, R. Gunaratne, V. W. Coljee, N. Kleckner, and M. Prentiss. Changes in the tension in dsDNA alter the conformation of RecA bound to dsDNA-RecA filaments. *Nucleic acids research*, 39(20):8833–43, Nov. 2011.

[38] A. B. Conway, T. W. Lynch, Y. Zhang, G. S. Fortin, C. W. Fung, L. S. Symington, and P. a. Rice. Crystal structure of a Rad51 filament. *Nature structural & molecular biology*, 11(8):791–6, Aug. 2004.

[39] M. S. Cooke, M. D. Evans, M. Dizdaroglu, and J. Lunec. Oxidative DNA damage: mechanisms, mutation, and disease. *FASEB journal : official publication of the Federation of American Societies for Experimental Biology*, 17(10):1195–214, July 2003.

[40] P. V. Cornish and T. Ha. A survey of single-molecule techniques in chemical biology. *ACS chemical biology*, 2(1):53–61, Jan. 2007.

[41] N. J. Curtin. DNA repair dysregulation from cancer driver to therapeutic target. *Nature Reviews Cancer*, 12(12):801–817, Nov. 2012.

[42] R. T. Dame, M. C. Noom, and G. J. L. Wuite. Bacterial chromatin organization by H-NS protein unravelled using dual DNA manipulation. *Nature*, 444(7117):387–90, Nov. 2006.

[43] S. S. David, V. L. O'Shea, and S. Kundu. Base-excision repair of oxidative DNA damage. *Nature*, 447(7147):941–50, June 2007.

[44] O. R. Davies and L. Pellegrini. Interaction with the BRCA2 C terminus protects RAD51-DNA filaments from disassembly by BRC repeats. *Nature structural & molecular biology*, 14(6):475–83, June 2007.

[45] I. De Vlaminck and C. Dekker. Recent advances in magnetic tweezers. *Annual review of biophysics*, 41:453–72, Jan. 2012.

[46] I. De Vlaminck, M. T. J. van Loenhout, L. Zweifel, J. den Blanken, K. Hooning, S. Hage, J. Kerssemakers, and C. Dekker. Mechanism of homology recognition in DNA recombination from dual-molecule experiments. *Molecular cell*, 46(5):616–24, June 2012.

[47] E. DiCapua, M. Schnarr, R. W. Ruigrok, P. Lindner, and P. a. Timmins. Complexes of RecA protein in solution. A study by small angle neutron scattering. *Journal of molecular biology*, 214(2):557–70, July 1990.

[48] E. H. Egelman and a. Stasiak. Structure of helical RecA-DNA complexes. Complexes formed in the presence of ATP-gamma-S or ATP. *Journal of molecular biology*, 191(4):677–97, Oct. 1986.

[49] F. Esashi, V. E. Galkin, X. Yu, E. H. Egelman, and S. C. West. Stabilization of RAD51 nucleoprotein filaments by the C-terminal region of BRCA2. *Nature structural & molecular biology*, 14(6):468–74, June 2007.

[50] C. M. Etson, S. M. Hamdan, C. C. Richardson, and A. M. van Oijen. Thioredoxin suppresses microscopic hopping of T7 DNA polymerase on duplex DNA. *Proceedings of the National Academy of Sciences of the United States of America*, 107(5):1900–5, Feb. 2010.

[51] G. Farge, N. Laurens, O. D. Broekmans, S. M. J. L. van den Wildenberg, L. C. M. Dekker, M. Gaspari, C. M. Gustafsson, E. J. G. Peterman, M. Falkenberg, and G. J. L. Wuite. Protein sliding and DNA denaturation are essential for DNA organization by human mitochondrial transcription factor A. *Nature communications*, 3:1013, Jan. 2012.

[52] I. J. Finkelstein and E. C. Greene. Single molecule studies of homologous recombination. *Molecular bioSystems*, 4(11):1094–104, Nov. 2008.

[53] A. L. Forget and S. C. Kowalczykowski. Single-molecule imaging of DNA pairing by RecA reveals a three-dimensional homology search. *Nature*, 482(7385):423–7, Mar. 2012.

[54] L. H. Fornander, K. Frykholm, A. Reymer, A. Renodon-Cornière, M. Takahashi, and B. Nordén. Ca2+ improves organization of single-stranded DNA bases in human Rad51 filament, explaining stimulatory effect on gene recombination. *Nucleic acids research*, pages 1–10, Feb. 2012.

[55] R. Galletto, I. Amitani, R. J. Baskin, and S. C. Kowalczykowski. Direct observation of individual RecA filaments assembling on single DNA molecules. *Nature*, 443(7113):875–878, 2006.

[56] B. Gibb, T. D. Silverstein, I. J. Finkelstein, and E. C. Greene. Single-stranded DNA curtains for real-time single-molecule visualization of protein-nucleic acid interactions. *Analytical chemistry*, 84(18):7607–12, Sept. 2012.

[57] J. Gorman, T. Fazio, F. Wang, S. Wind, and E. C. Greene. Nanofabricated racks of aligned and anchored DNA substrates for single-molecule imaging. *Langmuir : the ACS journal of surfaces and colloids*, 26(2):1372–9, Jan. 2010.

[58] J. Gorman and E. C. Greene. Visualizing one-dimensional diffusion of proteins along DNA. *Nature structural & molecular biology*, 15(8):768–74, Aug. 2008.

[59] P. Gross, G. Farge, E. J. G. Peterman, and G. J. L. Wuite. Combining optical tweezers, single-molecule fluorescence microscopy, and microfluidics for studies of DNA-protein interactions. *Methods in enzymology*, 475:427–53, Jan. 2010.

[60] P. Gross, N. Laurens, L. B. Oddershede, U. Bockelmann, E. J. G. Peterman, and G. J. L. Wuite. Quantifying how DNA stretches, melts and changes twist under tension. *Nature Physics*, 7(9):731–736, May 2011.

[61] R. C. Gupta, E. Folta-Stogniew, S. O'Malley, M. Takahashi, and C. M. Radding. Rapid exchange of A:T base pairs is essential for recognition of DNA homology by human Rad51 recombination protein. *Molecular cell*, 4(5):705–14, Nov. 1999.

[62] T. Ha, T. Enderle, D. F. Ogletree, D. S. Chemla, P. R. Selvin, and S. Weiss. Probing the interaction between two single molecules: fluorescence resonance energy transfer between a single donor and a single acceptor. *Proceedings of the National Academy of Sciences of the United States of America*, 93(13):6264–8, June 1996.

[63] T. Ha, A. G. Kozlov, and T. M. Lohman. Single-molecule views of protein movement on single-stranded DNA. *Annual review of biophysics*, 41:295–319, Jan. 2012.

[64] M. Hammel, M. Rey, Y. Yu, R. S. Mani, S. Classen, M. Liu, M. E. Pique, S. Fang, B. L. Mahaney, M. Weinfeld, D. C. Schriemer, S. P. Lees-Miller, and J. a. Tainer. XRCC4 protein interactions with XRCC4-like factor (XLF) create an extended grooved scaffold for DNA ligation and double strand break repair. *The Journal of biological chemistry*, 286(37):32638–50, Sept. 2011.

[65] D. Hanahan and R. a. Weinberg. Hallmarks of cancer: the next generation. *Cell*, 144(5):646–74, Mar. 2011.

[66] N. Handa, P. R. Bianco, R. J. Baskin, and S. C. Kowalczykowski. Direct visualization of RecBCD movement reveals cotranslocation of

the RecD motor after chi recognition. *Molecular cell*, 17(5):745–50, Mar. 2005.

[67] Y. Harada, T. Funatsu, K. Murakami, Y. Nonoyama, a. Ishihama, and T. Yanagida. Single-molecule imaging of RNA polymerase-DNA interactions in real time. *Biophysical journal*, 76(2):709–15, Feb. 1999.

[68] Y. Hashimoto, A. Ray Chaudhuri, M. Lopes, and V. Costanzo. Rad51 protects nascent DNA from Mre11-dependent degradation and promotes continuous DNA synthesis. *Nature structural & molecular biology*, 17(11):1305–11, Nov. 2010.

[69] M. Hegner, S. B. Smith, and C. Bustamante. Polymerization and mechanical properties of single RecA-DNA filaments. *Proceedings of the National Academy of Sciences*, 96(18):10109–10114, Aug. 1999.

[70] K. M. Herbert, A. La Porta, B. J. Wong, R. A. Mooney, K. C. Neuman, R. Landick, and S. M. Block. Sequence-resolved detection of pausing by single RNA polymerase molecules. *Cell*, 125(6):1083–94, June 2006.

[71] W.-D. Heyer, K. T. Ehmsen, and J. Liu. Regulation of homologous recombination in eukaryotes. *Annual review of genetics*, 44:113–39, Jan. 2010.

[72] J. Hilario, I. Amitani, R. J. Baskin, and S. C. Kowalczykowski. Direct imaging of human Rad51 nucleoprotein dynamics on individual DNA molecules. *Proceedings of the National Academy of Sciences of the United States of America*, 106(2):361–368, Jan. 2009.

[73] J. H. Hoeijmakers. Genome maintenance mechanisms for preventing cancer. *Nature*, 411(6835):366–74, May 2001.

[74] S. J. Holden, S. Uphoff, J. Hohlbein, D. Yadin, L. Le Reste, O. J. Britton, and A. N. Kapanidis. Defining the limits of single-molecule FRET resolution in TIRF microscopy. *Biophysical journal*, 99(9):3102–11, Nov. 2010.

[75] W. K. Holloman. Unraveling the mechanism of BRCA2 in homologous recombination. *Nature structural & molecular biology*, 18(7):748–54, July 2011.

[76] J. T. Holthausen, C. Wyman, and R. Kanaar. Regulation of DNA strand exchange in homologous recombination. *DNA repair*, 9(12):1264–72, Dec. 2010.

[77] P. Howard-Flanders, S. C. West, and A. Stasiak. Role of RecA protein spiral filaments in genetic recombination. *Nature*, 309(5965):215–220, May 1984.

[78] B. Ibarra, Y. R. Chemla, S. Plyasunov, S. B. Smith, J. M. Lázaro, M. Salas, and C. Bustamante. Proofreading dynamics of a processive DNA polymerase. *The EMBO journal*, 28(18):2794–802, Sept. 2009.

[79] G. Iliakis, H. Wang, A. R. Perrault, W. Boecker, B. Rosidi, F. Windhofer, W. Wu, J. Guan, G. Terzoudi, and G. Pantelias. Mechanisms of DNA double strand break repair and chromosome aberration formation. *Cytogenetic and genome research*, 104(1-4):14–20, Jan. 2004.

[80] K. Inoue and J. R. Lupski. Molecular mechanisms for genomic disorders. *Annual review of genomics and human genetics*, 3(121):199–242, Jan. 2002.

[81] T. Ishida, Y. Takizawa, I. Sakane, and H. Kurumizaka. The Lys313 residue of the human Rad51 protein negatively regulates the strand-exchange activity. *Genes to cells : devoted to molecular & cellular mechanisms*, 13(1):91–103, Jan. 2008.

[82] C. Jarzynski. Nonequilibrium Equality for Free Energy Differences. *Physical Review Letters*, 78(14):2690–2693, Apr. 1997.

[83] R. B. Jensen, A. Carreira, and S. C. Kowalczykowski. Purified human BRCA2 stimulates RAD51-mediated recombination. *Nature*, 467(7316):678–83, Oct. 2010.

[84] C. Joo, S. A. McKinney, M. Nakamura, I. Rasnik, S. Myong, and T. Ha. Real-time observation of RecA filament dynamics with single monomer resolution. *Cell*, 126(3):515–27, Aug. 2006.

[85] M. S. Junop, M. Modesti, A. Guarné, R. Ghirlando, M. Gellert, and W. Yang. Crystal structure of the Xrcc4 DNA repair protein and implications for end joining. *The EMBO journal*, 19(22):5962–70, Nov. 2000.

[86] I. Kamileri, I. Karakasilioti, and G. A. Garinis. Nucleotide excision repair: new tricks with old bricks. *Trends in genetics : TIG*, 28(11):566–73, Nov. 2012.

[87] L. C. Kapitein, M. E. Janson, S. M. J. L. van den Wildenberg, C. C. Hoogenraad, C. F. Schmidt, and E. J. G. Peterman. Microtubule-driven multimerization recruits ase1p onto overlapping microtubules. *Current biology : CB*, 18(21):1713–7, Nov. 2008.

[88] J. H. Kim and R. G. Larson. Single-molecule analysis of 1D diffusion and transcription elongation of T7 RNA polymerase along individual stretched DNA molecules. *Nucleic acids research*, 35(11):3848–58, Jan. 2007.

[89] K. Kim and O. A. Saleh. A high-resolution magnetic tweezer for single-molecule measurements. *Nucleic acids research*, 37(20):e136, Nov. 2009.

[90] S. C. Kowalczykowski, N. Lonberg, J. W. Newport, L. S. Paul, and P. H. von Hippel. On the thermodynamics and kinetics of the cooperative binding of bacteriophage T4-coded gene 32 (helix destabilizing) protein to nucleic acid lattices. *Biophysical journal*, 32(1):403–18, Oct. 1980.

[91] M. P. Landry, P. M. McCall, Z. Qi, and Y. R. Chemla. Characterization of photoactivated singlet oxygen damage in single-molecule optical trap experiments. *Biophysical journal*, 97(8):2128–36, Oct. 2009.

[92] M. J. Lang, P. M. Fordyce, A. M. Engh, K. C. Neuman, and S. M. Block. Simultaneous, coincident optical trapping and single-molecule fluorescence. *Nature methods*, 1(2):133–9, Nov. 2004.

[93] R. G. Larson, T. T. Perkins, D. E. Smith, S. Chu, B. Laboratories, L. Technologies, M. Avenue, and M. Hill. Hydrodynamics of a DNA molecule in a flow field. *Physical Review E*, 55(2):1794–1797, Feb. 1997.

[94] Y. Li, D. Y. Chirgadze, V. M. Bolanos-Garcia, B. L. Sibanda, O. R. Davies, P. Ahnesorg, S. P. Jackson, and T. L. Blundell. Crystal structure of human XLF/Cernunnos reveals unexpected differences from XRCC4 with implications for NHEJ. *The EMBO journal*, 27(1):290–300, Jan. 2008.

[95] M. R. Lieber. The mechanism of double-strand DNA break repair by the nonhomologous DNA end-joining pathway. *Annual review of biochemistry*, 79(D):181–211, Jan. 2010.

[96] J. Lipfert, J. W. J. Kerssemakers, T. Jager, and N. H. Dekker. Magnetic torque tweezers: measuring torsional stiffness in DNA and RecA-DNA filaments. *Nature methods*, 7(12):977–80, Dec. 2010.

[97] J. Lipfert, M. Wiggin, J. W. J. Kerssemakers, F. Pedaci, and N. H. Dekker. Freely orbiting magnetic tweezers to directly monitor changes in the twist of nucleic acids. *Nature communications*, 2:439, Jan. 2011.

[98] J. Liu, T. Doty, B. Gibson, and W.-D. Heyer. Human BRCA2 protein promotes RAD51 filament formation on RPA-covered single-stranded DNA. *Nature structural & molecular biology*, 17(10):1260–2, Oct. 2010.

[99] B. Maier, D. Bensimon, and V. Croquette. Replication by a single DNA polymerase of a stretched single-stranded DNA. *Proceedings of the National Academy of Sciences of the United States of America*, 97(22):12002–7, Oct. 2000.

[100] P. Mangeol and U. Bockelmann. Interference and crosstalk in double optical tweezers using a single laser source. *The Review of scientific instruments*, 79(8):083103, Aug. 2008.

[101] A. Mani, I. Braslavsky, R. Arbel-Goren, and J. Stavans. Caught in the act: the lifetime of synaptic intermediates during the search for homology on DNA. *Nucleic acids research*, 38(6):2036–43, Apr. 2010.

[102] P.-O. Mari, B. I. Florea, S. P. Persengiev, N. S. Verkaik, H. T. Brüggenwirth, M. Modesti, G. Giglia-Mari, K. Bezstarosti, J. a. a. Demmers, T. M. Luider, A. B. Houtsmuller, and D. C. van Gent. Dynamic assembly of end-joining complexes requires interaction between Ku70/80 and XRCC4. *Proceedings of the National Academy of Sciences of the United States of America*, 103(49):18597–602, Dec. 2006.

[103] A. V. Mazin and S. C. Kowalczykowski. The specificity of the secondary DNA binding site of RecA protein defines its role in DNA strand exchange. *Proceedings of the National Academy of Sciences of the United States of America*, 93(20):10673–8, Oct. 1996.

[104] A. V. Mazin and S. C. Kowalczykowski. The function of the secondary DNA-binding site of RecA protein during DNA strand exchange. *The EMBO journal*, 17(4):1161–8, Feb. 1998.

[105] a. V. Mazin, E. Zaitseva, P. Sung, and S. C. Kowalczykowski. Tailed duplex DNA is the preferred substrate for Rad51 protein-mediated homologous pairing. *The EMBO journal*, 19(5):1148–56, Mar. 2000.

[106] M. J. McCauley and M. C. Williams. Mechanisms of DNA binding determined in optical tweezers experiments. *Biopolymers*, 85(2):154–68, Feb. 2007.

[107] S. a. McKinney, C. Joo, and T. Ha. Analysis of single-molecule FRET trajectories using hidden Markov modeling. *Biophysical journal*, 91(5):1941–51, Sept. 2006.

[108] P. J. McKinnon and K. W. Caldecott. DNA strand break repair and human genetic disease. *Annual review of genomics and human genetics*, 8:37–55, Jan. 2007.

[109] J. Miné, L. Disseau, M. Takahashi, G. Cappello, M. Dutreix, and J.-L. Viovy. Real-time measurements of the nucleation, growth and dissociation of single Rad51-DNA nucleoprotein filaments. *Nucleic acids research*, 35(21):7171–87, Jan. 2007.

[110] K. Miyagawa. Clinical relevance of the homologous recombination machinery in cancer therapy. *Cancer science*, 99(2):187–94, Feb. 2008.

[111] M. Modesti. Fluorescent labeling of proteins. *Methods in molecular biology (Clifton, N.J.)*, 783:101–20, Jan. 2011.

[112] M. Modesti, J. E. Hesse, and M. Gellert. DNA binding of Xrcc4 protein is associated with V(D)J recombination but not with stimulation of DNA ligase IV activity. *The EMBO journal*, 18(7):2008–18, Apr. 1999.

[113] M. Modesti, M. S. Junop, R. Ghirlando, M. van de Rakt, M. Gellert, W. Yang, and R. Kanaar. Tetramerization and DNA Ligase IV Interaction of the DNA Double-strand Break Repair Protein XRCC4 are Mutually Exclusive. *Journal of Molecular Biology*, 334(2):215–228, Nov. 2003.

[114] M. Modesti, D. Ristic, T. van der Heijden, C. Dekker, J. van Mameren, E. J. G. Peterman, G. J. L. Wuite, R. Kanaar, and C. Wyman. Fluorescent human RAD51 reveals multiple nucleation sites and filament segments tightly associated along a single DNA molecule. *Structure (London, England : 1993)*, 15(5):599–609, May 2007.

[115] W. E. Moerner and D. P. Fromm. Methods of single-molecule fluorescence spectroscopy and microscopy. *Review of Scientific Instruments*, 74(8):3597, 2003.

[116] J. R. Moffitt, Y. R. Chemla, D. Izhaky, and C. Bustamante. Differential detection of dual traps improves the spatial resolution of optical tweezers. *Proceedings of the National Academy of Sciences of the United States of America*, 103(24):9006–11, June 2006.

[117] J. R. Moffitt, Y. R. Chemla, S. B. Smith, and C. Bustamante. Recent advances in optical tweezers. *Annual review of biochemistry*, 77:205–28, Jan. 2008.

[118] S. Myong, M. M. Bruno, A. M. Pyle, and T. Ha. Spring-loaded mechanism of DNA unwinding by hepatitis C virus NS3 helicase. *Science (New York, N.Y.)*, 317(5837):513–6, July 2007.

[119] S. Negrini, V. G. Gorgoulis, and T. D. Halazonetis. Genomic instability–an evolving hallmark of cancer. *Nature reviews. Molecular cell biology*, 11(3):220–8, Mar. 2010.

[120] K. C. Neuman and S. M. Block. Optical trapping. *The Review of scientific instruments*, 75(9):2787–809, Sept. 2004.

[121] K. C. Neuman and A. Nagy. Single-molecule force spectroscopy: optical tweezers, magnetic tweezers and atomic force microscopy. *Nature methods*, 5(6):491–505, June 2008.

[122] J. Nomme, Y. Takizawa, S. F. Martinez, A. Renodon-Cornière, F. Fleury, P. Weigel, K.-i. Yamamoto, H. Kurumizaka, and M. Takahashi. Inhibition of filament formation of human Rad51 protein by a small peptide derived from the BRC-motif of the BRCA2 protein. *Genes to cells : devoted to molecular & cellular mechanisms*, 13(5):471–81, May 2008.

[123] M. C. Noom, B. van den Broek, J. van Mameren, and G. J. L. Wuite. Visualizing single DNA-bound proteins using DNA as a scanning probe. *Nature methods*, 4(12):1031–6, Dec. 2007.

[124] L. Pellegrini, D. S. Yu, T. Lo, S. Anand, M. Lee, T. L. Blundell, and A. R. Venkitaraman. Insights into DNA recombination from the structure of a RAD51-BRCA2 complex. *Nature*, 420(6913):287–93, Nov. 2002.

[125] T. Perkins, D. Smith, and S. Chu. Direct observation of tube-like motion of a single polymer chain. *Science*, 264(5160):819–822, May 1994.

[126] T. Perkins, D. Smith, and S. Chu. Relaxation of a single DNA molecule observed by optical microscopy. *Science*, 264(5160):822–826, May 1994.

[127] P. Pierobon, J. Miné-Hattab, G. Cappello, J.-L. Viovy, and M. Lagomarsino. Separation of time scales in one-dimensional directed nucleation-growth processes. *Physical Review E*, 82(6):061904, Dec. 2010.

[128] C. Prvost and M. Takahashi. Geometry of the DNA strands within the RecA nucleofilament: role in homologous recombination. *Quarterly Reviews of Biophysics*, 36(4):429–453, Nov. 2003.

[129] H. Qian, M. P. Sheetz, and E. L. Elson. Single particle tracking. Analysis of diffusion and flow in two-dimensional systems. *Biophysical journal*, 60(4):910–21, Oct. 1991.

[130] S. R. Quake, H. Babcock, and S. Chu. The dynamics of partially extended single molecules of DNA. *Nature*, 388(6638):151–4, July 1997.

[131] S. Quiros, W. P. Roos, and B. Kaina. Rad51 and BRCA2–New molecular targets for sensitizing glioma cells to alkylating anticancer drugs. *PloS one*, 6(11):e27183, Jan. 2011.

[132] K. Ragunathan, C. Joo, and T. Ha. Real-time observation of strand exchange reaction with high spatiotemporal resolution. *Structure (London, England : 1993)*, 19(8):1064–73, Aug. 2011.

[133] U. Resch-Genger, M. Grabolle, S. Cavaliere-Jaricot, R. Nitschke, and T. Nann. Quantum dots versus organic dyes as fluorescent labels. *Nature methods*, 5(9):763–75, Oct. 2008.

[134] A. Reymer, K. Frykholm, K. Morimatsu, M. Takahashi, and B. Nordén. Structure of human Rad51 protein filament from molecular modeling and site-specific linear dichroism spectroscopy. *Proceedings of the National Academy of Sciences of the United States of America*, 106(32):13248–53, Aug. 2009.

[135] D. Ristic, M. Modesti, T. van der Heijden, J. van Noort, C. Dekker, R. Kanaar, and C. Wyman. Human Rad51 filaments on double- and single-stranded DNA: correlating regular and irregular forms with recombination function. *Nucleic acids research*, 33(10):3292–302, Jan. 2005.

[136] R. B. Robertson, D. N. Moses, Y. Kwon, P. Chan, P. Chi, H. Klein, P. Sung, and E. C. Greene. Structural transitions within human Rad51 nucleoprotein filaments. *Proceedings of the National Academy of Sciences of the United States of America*, 106(31):12688–93, Aug. 2009.

[137] V. Ropars, P. Drevet, P. Legrand, S. Baconnais, J. Amram, G. Faure, J. a. Márquez, O. Piétrement, R. Guerois, I. Callebaut, E. Le Cam, P. Revy, J.-P. de Villartay, and J.-B. Charbonnier. Structural characterization of filaments formed by human Xrcc4-Cernunnos/XLF complex involved in nonhomologous DNA end-joining. *Proceedings of the National Academy of Sciences of the United States of America*, 108(31):12663–8, Aug. 2011.

[138] I. Rouzina and V. A. Bloomfield. Force-induced melting of the DNA double helix 1. Thermodynamic analysis. *Biophysical journal*, 80(2):882–93, Feb. 2001.

[139] I. Rouzina and V. A. Bloomfield. Force-induced melting of the DNA double helix. 2. Effect of solution conditions. *Biophysical journal*, 80(2):894–900, Feb. 2001.

[140] R. Roy, S. Hohng, and T. Ha. A practical guide to single-molecule FRET. *Nature methods*, 5(6):507–16, June 2008.

[141] S. Roy, S. N. Andres, A. Vergnes, J. a. Neal, Y. Xu, Y. Yu, S. P. Lees-Miller, M. Junop, M. Modesti, and K. Meek. XRCC4's interaction with XLF is required for coding (but not signal) end joining. *Nucleic acids research*, pages 1–11, Jan. 2012.

[142] J. San Filippo, P. Sung, and H. Klein. Mechanism of eukaryotic homologous recombination. *Annual review of biochemistry*, 77(February):229–57, Jan. 2008.

[143] W. L. Santivasi and F. Xia. The role and clinical significance of DNA damage response and repair pathways in primary brain tumors. *Cell & bioscience*, 3(1):10, Jan. 2013.

[144] Y. Santoso, C. M. Joyce, O. Potapova, L. Le Reste, J. Hohlbein, J. P. Torella, N. D. F. Grindley, and A. N. Kapanidis. Conformational transitions in DNA polymerase I revealed by single-molecule FRET. *Proceedings of the National Academy of Sciences of the United States of America*, 107(2):715–20, Jan. 2010.

[145] B. D. Sattin and M. C. Goh. Direct observation of the assembly of RecA/DNA complexes by atomic force microscopy. *Biophysical journal*, 87(5):3430–6, Nov. 2004.

[146] K. Schlacher, N. Christ, N. Siaud, A. Egashira, H. Wu, and M. Jasin. Double-strand break repair-independent role for BRCA2 in blocking stalled replication fork degradation by MRE11. *Cell*, 145(4):529–42, May 2011.

[147] T. Schmidt, U. Kubitscheck, D. Rohler, and U. Nienhaus. Photostability Data for Fluorescent Dyes: An Update. *Single Molecules*, 3(5-6):327–327, Nov. 2002.

[148] J. W. Shaevitz, E. A. Abbondanzieri, R. Landick, and S. M. Block. Backtracking by single RNA polymerase molecules observed at near-base-pair resolution. *Nature*, 426(6967):684–687, 2003.

[149] K.-S. Shim, C. Schmutte, K. Yoder, and R. Fishel. Defining the salt effect on human RAD51 activities. *DNA repair*, 5(6):718–30, June 2006.

[150] G. V. Shivashankar, M. Feingold, O. Krichevsky, and A. Libchaber. RecA polymerization on double-stranded DNA by using single-molecule manipulation: The role of ATP hydrolysis. *Proceedings of the National Academy of Sciences*, 96(14):7916–7921, July 1999.

[151] M. K. K. Shivji, S. R. Mukund, E. Rajendra, S. Chen, J. M. Short, J. Savill, D. Klenerman, and A. R. Venkitaraman. The BRC repeats of human BRCA2 differentially regulate RAD51 binding on single- versus double-stranded DNA to stimulate strand exchange. *Proceedings of the National Academy of Sciences of the United States of America*, 106(32):13254–9, Aug. 2009.

[152] B. L. Sibanda, D. Y. Chirgadze, and T. L. Blundell. Crystal structure of DNA-PKcs reveals a large open-ring cradle comprised of HEAT repeats. *Nature*, 463(7277):118–21, Jan. 2010.

[153] B. L. Sibanda, S. E. Critchlow, J. Begun, X. Y. Pei, S. P. Jackson, T. L. Blundell, and L. Pellegrini. Crystal structure of an Xrcc4-DNA ligase IV complex. *Nature structural biology*, 8(12):1015–9, Dec. 2001.

[154] S. Smith, L. Finzi, and C. Bustamante. Direct mechanical measurements of the elasticity of single DNA molecules by using magnetic beads. *Science*, 258(5085):1122–1126, Nov. 1992.

[155] S. B. S. B. Smith, Y. Cui, and C. Bustamante. Overstretching B-DNA: The Elastic Response of Individual Double-Stranded and Single-Stranded DNA Molecules. *Science*, 271(5250):795–799, Feb. 1996.

[156] M. Spies, I. Amitani, R. J. Baskin, and S. C. Kowalczykowski. RecBCD enzyme switches lead motor subunits in response to chi recognition. *Cell*, 131(4):694–705, Nov. 2007.

[157] M. Spies, P. R. Bianco, M. S. Dillingham, N. Handa, R. J. Baskin, and S. C. Kowalczykowski. A molecular throttle: the recombination hotspot chi controls DNA translocation by the RecBCD helicase. *Cell*, 114(5):647–54, Sept. 2003.

[158] T. R. Strick, J.-F. F. Allemand, D. Bensimon, A. Bensimon, and V. Croquette. The Elasticity of a Single Supercoiled DNA Molecule. *Science*, 271(5257):1835–1837, Mar. 1996.

[159] P. Sung and H. Klein. Mechanism of homologous recombination: mediators and helicases take on regulatory functions. *Nature Reviews Molecular Cell Biology*, 7(10):739–750, 2006.

[160] P. Sung, L. Krejci, S. Van Komen, and M. G. Sehorn. Rad51 recombinase and recombination mediators. *The Journal of biological chemistry*, 278(44):42729–32, Oct. 2003.

[161] M. Takahashi. Analysis of DNA-RecA protein interactions involving the protein self-association reaction. *The Journal of biological chemistry*, 264(1):288–95, Jan. 1989.

[162] A. Tal, R. Arbel-Goren, and J. Stavans. Cancer-associated mutations in BRC domains of BRCA2 affect homologous recombination induced by Rad51. *Journal of molecular biology*, 393(5):1007–12, Nov. 2009.

[163] P. B. Tarsa, R. R. Brau, M. Barch, J. M. Ferrer, Y. Freyzon, P. Matsudaira, and M. J. Lang. Detecting force-induced molecular transitions with fluorescence resonant energy transfer. *Angewandte Chemie (International ed. in English)*, 46(12):1999–2001, Jan. 2007.

[164] R. E. Thompson, D. R. Larson, and W. W. Webb. Precise nanometer localization analysis for individual fluorescent probes. *Biophysical journal*, 82(5):2775–83, May 2002.

[165] T. Thorslund, M. J. McIlwraith, S. a. Compton, S. Lekomtsev, M. Petronczki, J. D. Griffith, and S. C. West. The breast cancer tumor suppressor BRCA2 promotes the specific targeting of RAD51 to single-stranded DNA. *Nature structural & molecular biology*, 17(10):1263–5, Oct. 2010.

[166] G. Tombline and R. Fishel. Biochemical characterization of the human RAD51 protein. I. ATP hydrolysis. *The Journal of biological chemistry*, 277(17):14417–25, Apr. 2002.

[167] T. van der Heijden and C. Dekker. Monte carlo simulations of protein assembly, disassembly, and linear motion on DNA. *Biophysical journal*, 95(10):4560–9, Nov. 2008.

[168] T. van der Heijden, M. Modesti, S. Hage, R. Kanaar, C. Wyman, and C. Dekker. Homologous recombination in real time: DNA strand exchange by RecA. *Molecular cell*, 30(4):530–8, May 2008.

[169] T. van der Heijden, R. Seidel, M. Modesti, R. Kanaar, C. Wyman, and C. Dekker. Real-time assembly and disassembly of human RAD51 filaments on individual DNA molecules. *Nucleic acids research*, 35(17):5646–57, Jan. 2007.

[170] T. van der Heijden, J. van Noort, H. van Leest, R. Kanaar, C. Wyman, N. H. Dekker, N. Dekker, and C. Dekker. Torque-limited RecA polymerization on dsDNA. *Nucleic acids research*, 33(7):2099–105, Jan. 2005.

[171] M. A. van Dijk, L. C. Kapitein, J. van Mameren, C. F. Schmidt, and E. J. G. Peterman. Combining optical trapping and single-molecule fluorescence spectroscopy: enhanced photobleaching of fluorophores. *The journal of physical chemistry. B*, 108(20):6479–84, May 2004.

[172] M. T. J. van Loenhout, T. van der Heijden, R. Kanaar, C. Wyman, and C. Dekker. Dynamics of RecA filaments on single-stranded DNA. *Nucleic Acids Research*, 37(12):4089–4099, 2009.

[173] J. van Mameren, P. Gross, G. Farge, P. Hooijman, M. Modesti, M. Falkenberg, G. J. L. Wuite, and E. J. G. Peterman. Unraveling the structure of DNA during overstretching by using multicolor, single-molecule fluorescence imaging. *Proceedings of the National Academy of Sciences of the United States of America*, 106(43):18231–6, Oct. 2009.

[174] J. van Mameren, M. Modesti, R. Kanaar, C. Wyman, E. J. G. Peterman, and G. J. L. Wuite. Counting RAD51 proteins disassembling from nucleoprotein filaments under tension. *Nature*, 457(7230):745–8, Feb. 2009.

[175] J. van Mameren, M. Modesti, R. Kanaar, C. Wyman, G. J. L. Wuite, E. J. G. Peterman, and J. van Mameren. Dissecting elastic heterogeneity along DNA molecules coated partly with Rad51 using concurrent fluorescence microscopy and optical tweezers. *Biophysical journal*, 91(8):L78–80, Oct. 2006.

[176] J. van Mameren, E. J. G. Peterman, and G. J. L. Wuite. See me, feel me: methods to concurrently visualize and manipulate single DNA molecules and associated proteins. *Nucleic acids research*, 36(13):4381–9, Aug. 2008.

[177] A. M. van Oijen, P. C. Blainey, D. J. Crampton, C. C. Richardson, T. Ellenberger, and X. S. Xie. Single-molecule kinetics of lambda exonuclease reveal base dependence and dynamic disorder. *Science (New York, N.Y.)*, 301(5637):1235–8, Aug. 2003.

[178] M. Wang, H. Yin, R. Landick, J. Gelles, and S. Block. Stretching DNA with Optical Tweezers. *Biophysical Journal*, 72(March), 1997.

[179] Y. Wang, R. Austin, and E. Cox. Single Molecule Measurements of Repressor Protein 1D Diffusion on DNA. *Physical Review Letters*, 97(4):048302, July 2006.

[180] M. S. Wold. Replication protein A: a heterotrimeric, single-stranded DNA-binding protein required for eukaryotic DNA metabolism. *Annual review of biochemistry*, 66:61–92, Jan. 1997.

[181] D. Woods and J. J. Turchi. Chemotherapy induced DNA damage response: Convergence of drugs and pathways. *Cancer biology & therapy*, 14(5), Feb. 2013.

[182] Q. Wu, T. Ochi, D. Matak-Vinkovic, C. V. Robinson, D. Y. Chirgadze, and T. L. Blundell. Non-homologous end-joining partners in a helical dance: structural studies of XLF-XRCC4 interactions. *Biochemical Society transactions*, 39(5):1387–92, suppl 2 p following 1392, Oct. 2011.

[183] G. J. Wuite, S. B. Smith, M. Young, D. Keller, and C. Bustamante. Single-molecule studies of the effect of template tension on T7 DNA polymerase activity. *Nature*, 404(6773):103–6, Mar. 2000.

[184] C. Wyman and R. Kanaar. DNA double-strand break repair: all's well that ends well. *Annual review of genetics*, 40:363–83, Jan. 2006.

[185] J. Xiao, A. M. Lee, and S. F. Singleton. Direct evaluation of a kinetic model for RecA-mediated DNA-strand exchange: the importance of nucleic acid dynamics and entropy during homologous genetic recombination. *Chembiochem : a European journal of chemical biology*, 7(8):1265–78, Aug. 2006.

[186] A. Yildiz, J. N. Forkey, S. a. McKinney, T. Ha, Y. E. Goldman, and P. R. Selvin. Myosin V walks hand-over-hand: single fluorophore imaging with 1.5-nm localization. *Science (New York, N.Y.)*, 300(5628):2061–5, June 2003.

[187] J. G. Yodh, M. Schlierf, and T. Ha. *Insight into helicase mechanism and function revealed through single-molecule approaches.*, volume 43. May 2010.

[188] J. G. Yodh, B. C. Stevens, R. Kanagaraj, P. Janscak, and T. Ha. BLM helicase measures DNA unwound before switching strands and hRPA promotes unwinding reinitiation. *The EMBO journal*, 28(4):405–16, Feb. 2009.

[189] K.-i. Yoshioka, Y. Yumoto-Yoshioka, F. Fleury, and M. Takahashi. pH- and salt-dependent self-assembly of human Rad51 protein analyzed as fluorescence resonance energy transfer between labeled proteins. *Journal of biochemistry*, 133(5):593–7, May 2003.

[190] X. Yu, S. a. Jacobs, S. C. West, T. Ogawa, and E. H. Egelman. Domain structure and dynamics in the helical filaments formed by RecA and Rad51 on DNA. *Proceedings of the National Academy of Sciences of the United States of America*, 98(15):8419–24, July 2001.

SAMENVATTING

Dit proefschrift is als volgt opgezet:

Hoofdstuk 2 bevat een uitgebreide uiteenzetting van bestaande literatuur over single-molecule experimenten met RecA and RAD51, het belangrijkste element van HR in prokaryotische en eukaryotische organismen. In HR assembleren RecA en RAD51 op enkelstrengs DNA, binden met de homologe sequentie op het zusterchromosoom, wisselen een streng uit en vallen uiteindelijk van het heteroduplex DNA af.Het binden van ATP coördineert al deze biochemische reacties, transformaties in de conformatie van het eiwit en ATP hydrolyse. "singe-molecule" aanpakken, zoals optische en magnetische tweezers (nanoschaal pincetten), FRET spectroscopie en fluorescentie microscopie maken het mogelijk om deze moleculaire mechanismen te isoleren en te bestuderen. Ondanks jaren van intensief onderzoek blijven vele inconsistenties en open vragen bestaan met betrekking tot dit onderwerp.

Hoofdstuk 3 beschrijft de techniek die in dit onderzoek gebruikt is: een combinatie van DNA-manipulatie (optische pincetten), directe visualisat van de eiwitten (single-molecule fluorescentie microscopie) en microfluïdische technologieën. Ik beschrijf de voordelen en het gebied van toepassing van deze specifieke aanpak voor het bestuderen van DNA-eiwit interacties. Daarnaast beschrijf ik enkele experimenten waarin ik de limieten van het lokaliseren van eiwit op een enkel DNA molecuul bestudeer als functie van de toegepaste spanning.

Hoofdstuk 4 beschrijft de biochemische methoden en procedures om enkelstrengs DNA te genereren uit single-molecule experimenten met behulp van optische pincetten. Er zijn veel biochemische methoden beschikbaar om dsDNA moleculen te modificeren, maar het aantal protocollen is veel beperkter. Ik beschrijf ook enkele praktische uitdagingen bij het intact houden van ssDNA moleculen tijdens de experimenten met de optische pincet en de procedures voor single-molecule studies.

Hoofdstuk 5 is een uitgebreide single-molecule studie naar het mechanisme achter het binden van RAD51-'nucleoprotein' filamenten aan zowel ssDNA als dsDNA. Aangetoond wordt dat filament binding zeer selectief

plaatsvindt met een voorkeur voor ssDNA boven dsDNA. Doordat we individuele RAD51 eiwitten kunnen tellen, hebben we de nucleation en groei van RAD51 filamenten afzonderlijk kunnen visualiseren en kwantificeren. Ik heb aan het licht gebracht dat het verschil in grootte tussen RAD51 kernen afhangt van de grootte van de filamenten in de oplossing.. We hebben een fysisch model ontwikkeld dat onze experimentele waarnemingen kwantitatief beschrijft. Bovendien hebben we het effect van BRC4, de RAD51-bindingseenheid van de borstkanker tumor onderdrukker BRCA2, op RAD51 filamentvormingbestudeerd.

Hoofdstuk 6 bediscussieert verschillende dynamische aspecten van het RAD51 nucleoprotein filament. Ik start met het beschrijven van een opvallend verschil in het gedrag tussen twee natuurlijk bestaande varianten van RAD51 (K313 and Q313). Ik neem daarbij waar dat deze biochemische verandering RAD51 activeert om langs het ssDNA te bewegen volgens een mechanisme van diffussie en sprongen. Met het gebruik van "dynamische kracht-spectroscopie", hebben we bekeken hoe de kracht de structuur van het RAD51 nucleoprotein filament beïnvloedt. Met metingen ver buiten de evenwichtstoestand was het mogelijk om het verschil in vrije energie verschil te meten tussen de RAD51 conformaties.

Hoofdstuk 7 presenteert het DNA-binding en 'bridging' mechanisme van XRCC4 en XLF – twee cruciale onderdelen van de non-homologous end joining pathway (NHEJ). Ik nam waar dat de vorming van XRCC4-XLF filamenten de mechanische eigenschappen van DNA niet beinvloedt. Dit gaf ons inzicht in het mechanisme van XRCC4 en XLF in het binden aan DNA. De DNA-binding modus van het XRCC4-XLF filament is zeer complex en wordt gekarakteriseerd door schuiven, pauzeren en filament herschikking. Tot slot hebben we een innovatieve analyse ontwikkeld om de DNA 'end-bridging' activiteit van XRCC4-XLF te bestuderen.

ACKNOWLEDGMENTS

I visited the VU for the first time in 2007. I was in The Netherlands for not very long and I was busy with my master project in the single-molecule biophysics group at the TU Delft when I accidentally encountered Gijs. He was giving a presentation about the latest instruments that he and his colleague, Erwin Peterman, developed in Amsterdam. After the presentation ended I directly asked if he had some PhD positions starting anytime soon. Unfortunately the answer was negative. But we could apply for a grant together and maybe I could start the following year on DNA repair. That worked out well at the end. And this PhD too, finally. Overall it has been a great choice and I would certainly do it again.

The first two people I want to thank are my two promotors, Gijs Wuite and Erwin Peterman. I felt your trust all along in this PhD and that helped me a lot in the most difficult moments. It took some time before we got really started but finally some good results came out. The daily life in the group has a great atmosphere and more and more exciting projects are starting every month. It's great to see a new generation of young scientist joining the lab and bringing a lot of fresh thoughts in the group.

I spent several years together with a lot of friends in a small room and in the underground basement. Working for longer than half-an-hour in a row was real challenge in certain days where everybody was in a good mood. But good friendships started and I am very happy about it. I had great times with Gerrit, Tjalle, Felix and Bram, and I they'll continue. In our office I witnessed rare but great moments of discovery and daily research frustrations with the other PhD students of "the barrack", Peter, Niels, Onno, Geraldine and Daan. Just next door, Jona, Aravinan and Marion are experiencing the same problems. Good luck with your science. Ineke, it's great you have chosen to work on DNA repair, looking back at this thesis I see so many great chances for future research. Cannot wait to hear what will come up. I want to mention Stephanie and Mariella, a lot of this thesis is thanks to you both. I am very glad you decided to continue your career in research. You will do a great job.

I want to wish good luck for their academic career to our post-docs: Iddo, Matthijs, Wouter, Andreas, Greame, Seyda, Pierre and Jules. Most of the time are all early coffee-timers and I am sure this will help a lot in their future career!

Now I want to thank some really special people with whom I shared a lot in these years and made up the small Little Italy community: Andrea, Valentina, Vasco, Matteo, Matteo, Valerio e Pierluigi.

Voglio ringraziare i miei genitori, la mia famiglia e miei amici Andrea, Stefano, Tommaso, Gianluca, Emanuele e Francesco per il supporto in tutti questi anni passati lontano da casa.

And finally thank you Anne, this thesis is mainly for you. You supported me all along this journey. I hope I did the same with your.